

Reduction of underwater piling noise

An optimization of the impact force to reduce underwater noise
during the installation of a large sized monopile

by

Jorrit van Rhijn

In partial fulfillment of the requirements for the degree of

Master of Science

in Offshore and Dredging Engineering
at the Delft University of Technology

Student number: 1516639
Date: January 19, 2017
Committee: Prof.dr. A.Metrikine TU Delft - Chairman
Dr.ir. A.Tsouvalas TU Delft
Dr.ir. K.N. van Dalen TU Delft
Ir. O. Sainz Avila Boskalis

Abstract

Offshore wind is a fast growing industry that has the potential to play an increasing role in the near future of power generation. As the industry evolves, wind farms are constructed further offshore where the wind is less turbulent and more space is available to increase the size of the wind farms. Furthermore, the capacity and size of wind turbine generators is growing due to technical developments. As a result, the foundation structure increases in size to assure stability and sufficient support of the generator. In general a monopile (large diameter steel cylinder) is the preferred foundation due to its economic benefits and relatively simple installation. In 2015, approximately 80% of all the offshore foundations installed in Europe were monopiles. This amount is expected to rise taking into account offshore wind farms that are currently being developed. For the installation of a monopile, a large amount of energy is applied by the impact of a hammer on top of the pile. This impact generates waves that propagate through the surrounding air, water and soil over large distances and disturb the marine life. Consequently, pile driving has become a strictly regulated construction process. Therefore, the offshore wind industry developed a variety of noise mitigation methods to reduce the underwater noise. However, these are expensive methods, driving the costs of noise mitigation till approximately 15% of the total installation costs of an offshore wind farm foundation.

Noise which directly radiates into the water is referred to as the primary noise path. Noise which re-radiates from the soil back into the water is referred as the secondary noise path. With increasing size of the monopiles, the ring frequency of the shell (the frequency at which the monopile moves radially outwards and inwards together) shifts towards lower frequencies. In addition, the amount of energy required to drive the monopile into the soil increases, resulting at a longer duration of the impact force and hence lower frequencies to be excited. Low frequency waves are less attenuated in soil compared to high frequencies, increasing the influence of the secondary noise path. However, most of the noise mitigation systems nowadays do not consider the secondary noise path and hence become less effective in reducing underwater noise generated by large monopiles.

The aim of this research is to investigate ways to reduce noise levels directly at the source of the noise, instead of mitigating the radiated noise. This is achieved by optimizing the impact force with respect to noise, while keeping the drivability unimpaired. First of all, insight in the noise propagation during installation of a large sized monopile is obtained. This is done by modeling acoustics with a basic spring dashpot model and a more advanced elastic medium model derived by Tsouvalas and Metrikine [2013 2014]. The analysis shows a large amount of energy at low frequencies carried by waves traveling along the soil-water interface, so called "Scholte waves". Both models are validated with measurements. The impact force, which serves as input for both models, is obtained from the drivability program GRLWEAP.

For the optimization process, multiple steps are taken. Firstly, the dominant acoustic frequencies of the pile-water-soil system are derived that result in a high response after excitation. Secondly, a method is developed to evade the dominant acoustic frequencies in the amplitude excitation spectrum of the hammer. In order to keep the drivability with the adjusted impact force unimpaired, a basic non-linear drivability model is developed based on mass, springs and dashpots. The non-linearity is limited to the description of the sliding of the monopile into the soil with locally reacting non-linear springs. A concept which still needs to be verified for the case of large piles and relatively low frequencies. Finally, an additional analysis on the effect of the adjusted impact force on the noise levels is performed. The results show an increased amount of energy at low frequencies carried by waves traveling along the soil-water interface. Due to the high geometrical and material damping in the soil, the high frequency compressional waves attenuate rather quickly with increasing distance from the pile, resulting at shear and Scholte waves being dominant at larger distances. The energy carried by the latter is increased compared to the previous analysis with the non-adjusted impact diagram. However, the Scholte wave produces only pressure fluctuations in the water close to the soil-water interface and not further up into the water column. With the current derived analysis method, the noise levels at 100 m from the piling source are reduced while drivability is kept largely unimpaired.

Preface

With the enormous extension of offshore wind farms recently, the installation of the foundations must happen as fast as possible and remain economical beneficial. This looks relatively easy; you bring a pile, put it on the ground and hit it with a hammer to penetrate it into the soil till the required depth. Large installation vessels and noisy equipment are required who produce a large amount of disturbance to the surrounding environment. But who cares? Besides of the construction team, there are no other people who suffer from the noise that is released during the installation. Consequently, all day long and 7 days a week monopiles were installed without any downtime. Ideal conditions you would say.

But then all of a sudden, people started worrying about the marine life. The noise levels could damage the marine life, which in my opinion is completely true. As a result, countries introduces regulations with regard to underwater noise. This was the start of a large change in the offshore wind farm installation process causing more downtime and high costs. On the other hand, this development gained new opportunities. New methods to reduce the underwater noise levels had to be engineered, develop and finally construct. This raised a lot of new questions for engineers to be solved. With my graduation thesis, I can now proudly say I was one of them. As this is a relative new topic, I was inspired and very motivated to gain new insights in order to find a way to reduce the underwater noise. It has been a challenging research project given the limited knowledge and data beforehand, but highly rewarding due to the better understanding of the phenomena afterwards. The thesis has been written to fulfill the graduation requirements of the master program in Offshore and Dredging Engineering at the Delft University of Technology.

I would like to take the opportunity to thank all those who contributed to this work. First, I would like to thank my daily supervisor Oscar from Boskalis. With the limited knowledge you and I had on this topic, your profound interest in my research which inspired me even further. Thank you for always being available for me to help, even though you were offshore or even on holidays. Second, from the university I would like to thank Apostolos, my daily supervisor. I was the first student to work with your models which sometimes required some knowledge I did not have at the beginning. Thank you for always being available for questions and explanation with regard to the topic and the models. And remaining so patient when I once again did not understand something the first time. Third, I would like to thank Prof. Metrikine for your guidance in bringing this project to completion. Each meeting gave me a lot of new information and input for my research. Fourth, I would like to thank all the students at Boskalis, for making the time enjoyable as well. For those still busy at the moment, I wish you all the luck.

Finally, thanks to my parents for supporting me during my studies and many thanks to my friends and girlfriend for supporting me and accepting the fact that I was living under a stone for the past few months. I had a great time doing this project and writing this thesis, I hope you enjoy reading.

Jorrit van Rhijn, Papendrecht, January, 2017

Nomenclature

α_p	Compressional wave attenuation
α_s	Shear wave attenuation
δ	Constant volume friction angle
η	Damping steel
λ	Wavelength
ν	Poisson ratio
ϕ	Friction angle
ρ	Density
<i>ADD</i>	Acoustic Deterrent Devices
<i>BSH</i>	Federal Maritime and Hydrographic Agency
c_b	Wave speed in soil
c_p	Compressional wave speed
c_s	Shear wave speed
c_w	Wave speed in water
<i>CPT</i>	Cone Penetration Test
<i>D</i>	Diameter
<i>d</i>	Depth to layer
<i>dB</i>	Decibel
<i>DBBC</i>	Double Big Bubble Curtains
<i>DFT</i>	Discrete Fourier Transform
<i>E</i>	Elasticity Modulus
<i>EEZ</i>	Exclusive Economic Zones
f_{shaft}	Shaft friction
f_{si}	Initial shaft friction
f_{sres}	Residual shaft friction
f_{tip}	Unit Tip Resistance
<i>GPS</i>	Global Positioning System
<i>GRLWEAP</i>	Goble-Rausche-Liking Wave Equation Analysis Program
<i>HSD</i>	Hydro Sound Damper
<i>I</i>	Intensity

<i>ITAP</i>	Institut für Technische und Angewandte Physik
<i>K</i>	Horizontal stress ratio after driving
<i>k</i>	Shape factor for degradation
<i>k_r</i>	Spring stiffness radial direction
<i>k_z</i>	Spring stiffness vertical direction
<i>k_θ</i>	Spring stiffness circumferential direction
<i>L</i>	Length
<i>LNG</i>	Liquid Nitrogen Gas
<i>MMO</i>	Marine Mammal Observer
<i>OWF</i>	Offshore Windforce VM
<i>p</i>	Pile Tip penetration
<i>p'₀</i>	Effective pressure
<i>p_r</i>	Reference pressure
<i>PTS</i>	Permanent Threshold Shift
<i>Q</i>	Quake
<i>Q_f</i>	Quality factor
<i>q_t</i>	Total cone tip resistance
<i>r</i>	Radial distance
<i>R_m</i>	Resistance force
<i>SEL</i>	Sound Exposure Level
<i>SPL</i>	Sound Pressure Level
<i>SRD</i>	Static Resistance to Driving
<i>t</i>	Thickness
<i>TTS</i>	Temporary Threshold Shift
<i>WEAP</i>	Wave Equation Analysis Program

Contents

1	Introduction	1
1.1	Background Information	1
1.2	Problem definition	2
2	Literature study	3
2.1	Energy demand	3
2.1.1	Status of Offshore Wind Power	4
2.1.2	Foundation	4
2.2	Pile Driving Proces	5
2.2.1	Pile Driving using Impact Hammers	6
2.2.2	Pile driving using Vibratory Hammers	7
2.2.3	Pile driving using BLUE Piling	8
2.3	Sound.	9
2.3.1	Sound attenuation	11
2.3.2	Sound notation	12
2.3.3	Underwater Noise	13
2.3.4	Underwater noise mitigation.	15
3	System Parameters	17
3.1	Soil Data	17
3.1.1	Impact Diagram	18
3.2	Additional Impact Diagram	20
3.3	Model Specific Parameters	21
3.3.1	Spring Dashpot Model	21
3.3.2	Elastic Medium Model	22
3.4	Conclusions.	23
4	Spring Dashpot Model	25
4.1	A 3-D spring dashpot model	25
4.2	Model Interface	27
4.3	Validation.	30
4.3.1	Response during pile driving at different stages	32
4.4	Parametric Study	35
4.4.1	Response in frequency domain	35
4.4.2	Response in time domain	36
4.5	Conclusions.	37
5	Elastic Medium Model	39
5.1	A 3-D vibroacoustic model	39
5.2	Model Interface	40
5.3	Validation.	42
5.3.1	Response during pile driving at different stages in frequency domain	43
5.3.2	Response during pile driving at different stages in time domain	44
5.3.3	Conclusions	46
5.4	Energy propagation	47
5.4.1	Energy input into the pile	47
5.4.2	Energy launched into the soil and fluid layer.	48
5.5	Parametric study	51
5.5.1	Influence of soil elasticity	52
5.5.2	Influence of soil attenuation	53
5.5.3	Influence of two soil layers.	54

5.6	Conclusions.	56
6	Pile Driving Analysis	57
6.1	Mechanism of soil reaction	57
6.2	Theory of Pile Driving Models.	58
6.3	Drivability Model	59
6.3.1	Basic theory of drivability model.	59
6.3.2	Validation of drivability model	61
6.4	Conclusions.	62
7	Model Comparison	65
7.1	Velocity Comparison	65
7.1.1	Influence of Soil Elasticity	67
7.1.2	Corrected Velocity Comparison	69
7.2	Energy Comparison.	71
7.3	Conclusions.	72
8	Force Optimization	73
8.1	Function Analysis.	73
8.1.1	Fourier Analysis	73
8.1.2	Fourier transformation properties	74
8.2	Method description	76
8.2.1	Simple Scaling Approach.	77
8.2.2	Acoustic Optimization Approach	78
8.3	Adjusted Absolute Excitation Spectrum	79
8.3.1	Dominant acoustic frequencies	81
8.3.2	Remove energy from excitation spectrum	82
8.3.3	Obtain Time Trace	83
8.4	Drivability Analysis	83
8.5	Noise predictions with Spring Dashpot Model	84
8.5.1	Response during pile driving in frequency domain.	84
8.5.2	Response during pile driving in time domain	85
8.6	Noise predictions with Elastic Medium Model	86
8.6.1	Response during pile driving in frequency domain.	87
8.6.2	Response during pile driving in time domain	88
8.7	Conclusions.	91
9	Conclusions and Recommendations	93
9.1	Conclusions.	93
9.2	Recommendations	95
	Bibliography	97



Introduction

This master thesis with the title "Reduction of underwater piling noise: An optimization of the impact force to reduce underwater noise during the installation of a large sized monopile" serves as the graduation project of MSc. Student Offshore Engineering Jorrit van Rhijn, specialized in Arctic, Wind, Bottom Founded & Floating Structures.

1.1. Background Information

Offshore wind is a fast growing industry that has the potential to play an increasing role in the near future of power generation. As the industry evolves, wind farms are constructed further offshore where the wind is less turbulent and more space is available to increase the size of the wind farms. Furthermore, the capacity and size of wind turbine generators is growing due to technical developments. As a result, the foundation structure increases in size to assure stability and sufficient support of the generator. In general a monopile (large diameter steel cylinders) is the preferred foundation due to its economic benefits and relatively simple installation. In 2015, approximately 80% of all the offshore foundations installed in Europe were monopiles [EWEA; 2016]. This amount is expected to rise taking into account offshore wind farms that are currently being developed.

For the installation of a monopile, a large amount of energy is applied by the impact of a hammer on top of the pile. This impact generates high sound levels that propagate through the surrounding air, water and soil over large distances and disturbs the marine life. Consequently, pile driving has become a strictly regulated construction process in which the German government has implemented a strict regulation regarding allowable noise levels. These are set to 160 dB re $1\mu Pa^2 s$ for the Sound Exposure Level and 190 dB re $1\mu Pa s$ for the peak level at a distance of 750 m from the piling source. Therefore, the offshore wind industry developed a variety of noise mitigation methods to reduce the underwater noise. Numerical modeling of the underwater acoustics before and after applying noise mitigation measures can provide useful insight into more specific measures to be taken. The industry features a variety of different models to do so, but not all are complete or sufficiently validated. Hence predicting noise levels which can be trusted, is still a significant issue in the offshore wind industry. Eventually, extra redundancy is added to fulfill the requirements of the local government or client and prevent downtime during installation. However, these are expensive methods, driving the costs of noise mitigation till approximately 15% of the total installing costs of an offshore wind farm foundation. As a result, the offshore wind industry is exploring new methods to decrease these costs.

This can roughly be done by permitting higher noise levels, preventing noise or mitigating noise to reduce noise levels. Permitting higher noise levels is unlikely to happen and should not be the starting point here. Mitigation of the propagating noise is most common, since the proven installation method is unaffected. However, the source of the high underwater noise level is the installation process which is often done by impact piling. Here a large steel rod hits an anvil and directs the energy into the monopile, which on its turn penetrates into the soil layer. The noise mitigation systems mainly focus on blocking the primary noise path, this is the path where noise directly radiates into the fluid layer. The secondary noise path, the path where noise re-radiates from the soil back into the fluid, is hereby left unimpaired. It is known that the noise miti-

gation systems depend partly on the local environmental conditions such as soil properties, pile dimensions and installation depth. The influence of the latter two are nowadays well understood. However, the significance of the former is often overlooked. Most of the noise mitigation systems nowadays do not consider the secondary noise path which mainly consists of low frequencies. With small (<5 m diameter) monopiles, the ring frequency is far above these low frequencies resulting in a less effective secondary noise path. However, according to the trend of moving towards larger (>5 m diameter) monopiles the low frequencies become of interest. This is due to the shift of the ring frequency of the shell towards lower frequencies.

Comparing impact piling with alternative piling methods like BLUE piling and vibratory piling results in a difference in the impact diagram. The impact diagram represents the duration over which the impact force is divided and corresponds directly to the output characteristic of the systems. A different piling method might result in a lower noise level. As a result, less or even non noise mitigation method is needed, which can be economically beneficial. However, this could also result in a shift of the frequency spectrum towards the lower frequencies whereby the current noise mitigation systems are less effective. This would make switching to an alternative piling method less attractive. The aim of this research is therefore to investigate ways to reduce noise levels directly at the source of the noise, instead of mitigating the radiated noise. This is done by optimizing the impact force with respect to noise, while keeping the drivability unimpaired. First of all, insight in the noise propagation during installation of a large sized monopile is obtained with the help of two acoustic models.

The first is the Spring Dashpot model by Tsouvalas and Metrikine [2013]. By means of the normal mode method, the modes of vibration of the shell structure are calculated. The frequencies of these vibrations give the horizontal wavenumbers that are associated with the modal propagation. The complete acoustic field is then constructed by summing up contributions by each mode. Due to the soil modeling, no influence of wave propagating through the soil is taken into account but only wave propagation in the fluid layer.

The second model is the Elastic Medium mode, also developed by Tsouvalas and Metrikine [2014]. In this model, the soil is modelled as an elastic medium and therefore takes into account shear waves and Scholte waves. These Scholte waves are known to contain a high amount of energy and can therefore have a significant influence on the final noise level as stated by Bruns et al. [2014]. Both models are validated with measurements. The impact force, which serves as input for both models, is obtained from the drivability program GRLWEAP.

For the optimization process, multiple steps are taken. Firstly, the dominant acoustic frequencies of the pile-water-soil system are derived that result in a high response after excitation. Secondly, a method is developed to evade the dominant acoustic frequencies in the amplitude excitation spectrum of the hammer. In order to keep the drivability with the adjusted impact force unimpaired, a basic non-linear drivability model is developed. The effect of the optimized impact force is extensively analyzed with the two earlier introduced acoustic models.

1.2. Problem definition

To provide a clear research structure in this thesis report the question is split in different smaller subquestions. By answering and combining the subquestions a solution is presented for the main objective:

"Can the time trace of an impact hammer be optimized in order to reduce structural vibrations and hence reduce underwater noise, while keeping the drivability unimpaired "

The objective can be obtained by answering the following subquestions:

1. How does the noise travel that is generated during the installation of a large sized monopile?
2. What are the dominant frequencies which generate large amplitude vibrations?
3. How can these dominant frequencies be avoided, keeping a realistic time trace?
4. How does changing the impact diagram affects the drivability?
5. What are the results with regard to the noise levels?

This study aims to contribute to the understanding of underwater noise and finally mitigation and to the process of developing reliable prediction models.

2

Literature study

This literature study aims at presenting a selection of topics related to wind energy. It mainly serves to introduce the research framework and the position of this study within that framework. In the first section, a brief description of the energy demand world wide and the position of offshore energy within is given. Also the selection of foundation is discussed here together with the trend for future foundations. In section 2.2, the affects that occur during pile driving with different hammers are discussed. Subsequently, in section 2.3 an introduction in acoustics and notations are presented and together with the concepts of underwater noise propagation and noise mitigation in relation to pile driving.

2.1. Energy demand

The U.S. Energy Information Administration recently released their International Energy Outlook for 2016 [EIA; 2016]. The report projects that world energy consumption will grow by 48% between 2012 and 2040. Renewable and nuclear power are the world's fastest-growing energy sources over that period. Renewable energy increases by an average 2.6% per year through 2040 and nuclear power increases by 2.3% per year as illustrated in Figure 2.1.

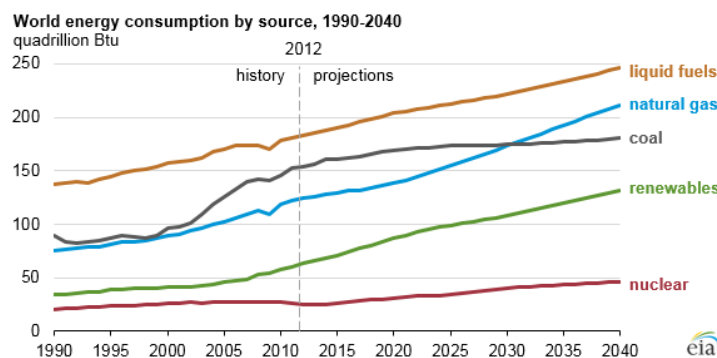


Figure 2.1: World energy consumption by source between 1990 and 2040 [EIA; 2016]

Even though non fossil fuels are expected to grow faster than fossil fuels, fossil fuels still account for more than three-quarters of world energy consumption through 2040. Natural gas, which has a lower carbon intensity than coal and petroleum, is the fastest-growing fossil fuel, with global natural gas consumption increasing by 1.9% per year. Rising supplies of tight gas, shale gas, and coalbed methane contribute to the increasing consumption of natural gas. Although liquid fuels remain the largest energy source, the liquids share of world marketed energy consumption is projected to fall from 33% in 2012 to 30% in 2040. As oil prices rise in the long term, many energy users adopt more energy-efficient technologies as wind power and switch away from liquid fuels when feasible.

In 2015 total investments in the renewable energy sector reached a record of EUR 296.6 billion. This is an increase of 4% compared to 2014 and beating the previous record set in 2011 by 3% [Bloomberg; 2016]. The new global total for wind power at the end of 2015 was 432.9 GW, representing cumulative market growth of more than 17%. In total an astonishing 63,467 MW were installed in 2015, from which almost half in China. This assures China's leadership position with 33.6% (145 GW) of total installed capacity by the end of 2015. Followed by USA with 17.2 %. Germany accounts for 10.4% closely followed by others like India, Spain and UK.

From the 432.9 GW total installed capacity worldwide, only 2.8% (12,107 MW) is placed offshore. Even though this is a small part, the amount of turbines needed to produced the same capacity onshore are many more. With an average turbine size of 3 MW onshore, this would require 4039 turbines. Compared to the 3230 turbines which are now located offshore, makes the offshore industry highly interesting. The size of an onshore wind turbine is limited by the maximum crane capacity and available space, where for the offshore wind turbine these limitations are less important [GWEC; 2015].

2.1.1. Status of Offshore Wind Power

In 1991, the first offshore wind farm, Vindeby, became operational near the coast of Denmark. This marked the start of a rapid expansion that led to a total installation of 12,107 MW worldwide in 2015. From that 91 % (11,027 MW) are installed in Europe, making Europe world leader in the offshore wind industry with 3,230 turbines. The remaining 9% of installed capacity is located mainly in China, followed by Japan and South Korea [EWEA; 2016] [GWEC; 2015].

As can be seen in Figure 2.2 within Europe the UK has the largest installed wind capacity offshore with 45.9% (5,061 MW). Followed by Germany in the second spot with 29.9%. Denmark accounts for 11.5%, Belgium 6.5%, Netherlands 3.9% and Sweden 1.8%. Other European markets including Finland, Ireland, Norway, Spain and Portugal make up about 0.5 % of the market in Europe.

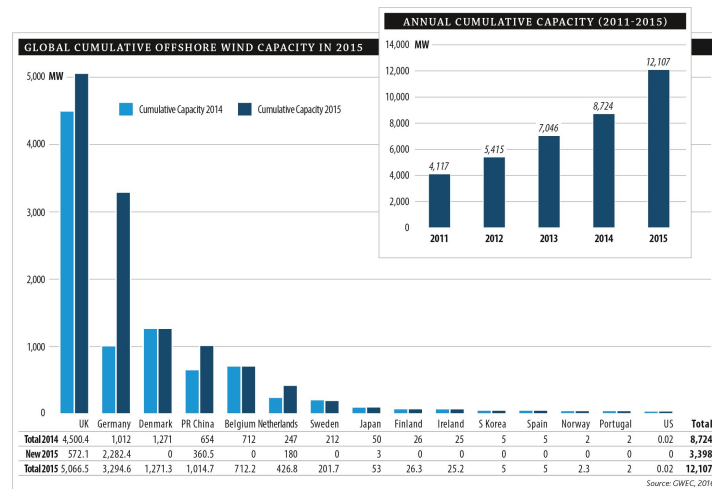


Figure 2.2: Installed wind capacity offshore in Europe in 2014 and 2015 [GWEC; 2015]

2.1.2. Foundation

Offshore wind is a fast growing industry that will play an increasing role in the near future power generation. As the industry evolves, offshore wind farms are constructed further offshore where the wind is less turbulent and more space is available to increase the size of the wind farms.

As described above, the offshore wind industry is growing rapidly. As the industry evolves, more offshore wind farms are expected to be constructed further offshore. Consequently the turbine sizes increase resulting in higher capacities. To support larger wind turbines, monopiles are preferred as they are relative easy to install and economically beneficial. An amount of approximately 80% of all the support support structures that are placed in offshore Europe during 2015 where monopiles as can be seen in Figure 2.3a. Over the last five years,

the average wind farm size has more than doubled from in 2010 of 155.3 MW to 337.9 MW in 2015.

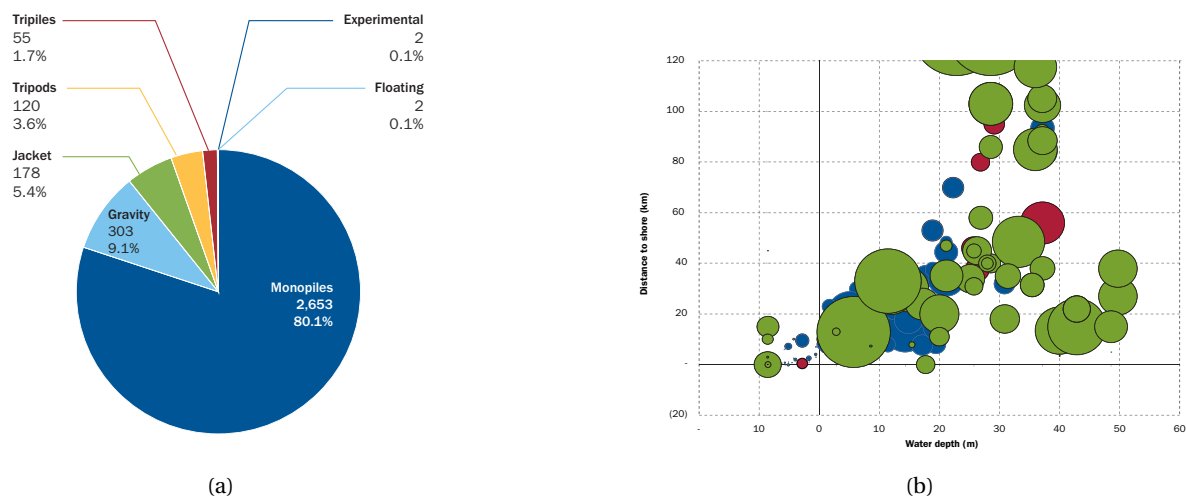


Figure 2.3: (a) Share of substructure type installed for wind turbines offshore and (b) Trend in average water depth and distance to shore of operating (blue), under construction (red) and scheduled (green) wind farms [EWEA; 2016]

A significant amount of new wind farm are planned to be installed as illustrated in Figure 2.3b. This shows the amount of wind farms operating, under construction or scheduled by 2015 for Europe against water depth and distance from shore. From here it can be concluded that almost all of them are within monopile applicable limits, which is approximately till 40 m water depth, and as a result implies that monopiles will still be governing for the near future. The monopile foundation used at offshore wind farms is basically a cylindrical tube compiled of steel. The tube is directly installed into the seabed using impact piling. This technique has been used in the onshore construction industry and offshore oil production before. Now it makes its way to wind energy where it has proven to be very effective. Its working principle is described in section 2.2.1. An advantage of using an impact hammer over vibratory hammer (section 2.2.2) is that instant compacting occurs. This creates a tight layer between pile and soil and increases the solidity. However, this does not necessarily mean that other methods are not suitable here. In general the behavior of soil and its bearing capacity after installation is still a matter of ongoing debate.

As a result of the increasing size of the monopiles, the natural frequency tends to shift towards lower frequencies. Generally speaking, the greater mass at the top of the structure and the more slender the structure itself, the lower its natural frequency. Consequently it gets closer to the forcing frequencies of the wind and waves and the risk of occurrence of resonance is higher [Sparrevik; 2014]. These are effects during operations that are taken into account already for years. But what is not taken into is the overlap between the natural frequencies of the monopile with the excitation spectrum of the installation force. The excitation spectrum of the installation force consists of relative low frequencies that can interfere with the shifted lower natural frequency of the vibration spectrum of the monopile during installation. Causing radial and vertical motions in the fluid and soil layer that can propagate very far as pressure waves. For the marine life this can be highly harassing and even lead to death. Reducing the underwater noise during piling should therefore be taken into account.

2.2. Pile Driving Proces

Pile driving refers to the proces of a pile being safely (i.e., without damage) and economically (i.e., with reasonably sized construction equipment, and without excessive blow counts) driven to support the required bearing capacity and possibly to a minimum required penetration depth as stated by Hussein et al. [2006]. A number of different methods are available, all with different static and dynamic effects. The two main hammers, Impact hammer and vibratory hammer are here discussed together with the new BLUE Piling method.

2.2.1. Pile Driving using Impact Hammers

An impact to a monopile induces a force and a particle velocity v at the top of the foundation. This causes a compressional wave propagating along the pile in axial direction, as can be seen in Figure 2.4.

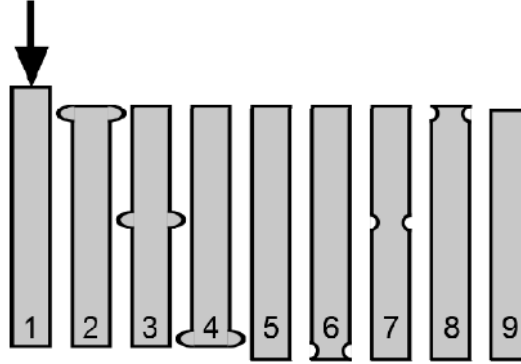


Figure 2.4: Simplified model of wave propagation in a monopile

The waves in a simplified one-dimensional system travel along the vertical axis of the monopile with a wave speed c_p , which is defined as:

$$c_p = \sqrt{\frac{E}{\rho}} \quad (2.1)$$

In which E is the modulus of elasticity and ρ is the mass density of the material. This estimation is based on a one-dimensional longitudinal model for the pile with no surrounding medium. The actual speed is slightly different depending on whether the pile is surrounded by fluid or soil and on the dispersion characteristics of the shell.

When reaching the tip of the monopile, the compression wave causes an associated radial expansion of the pile due to the Poisson's ratio effect [Achenbach; 1973]. This means that the compression wave propagates downwards to the tip and pushes the pile into the ground. Thereafter a tension or compression wave is reflected from the tip upwards. Whether it is a tension, or a compression wave depends on the soil resistance. High soil resistance results in a reflection of a compression wave where a low soil resistance, mainly only at the beginning of the piling process, result in a reflection of a tension wave as illustrated in Figure 2.4 [Kuhn et al.; 2014].

This process can easily be simplified by the reflection of the end of a free or fixed rod and by applying the method of the images that enables the rod motion to be presented in the form of propagating waves. Introducing an incident pulse of $u_i(t - x/c)$, propagating in the rod in the positive x -direction to a free end, the reflection process and stresses are described by:

$$\begin{aligned} u(x, t) &= u_i(t - x/c) + u_i(t + x/c) \\ \sigma(x, t) &= \sigma_i(t - x/c) - \sigma_i(t + x/c) \end{aligned} \quad (2.2)$$

From here it is clear that the direction of the displacement in the reflected pulse is identical to that in the incidental pulse, while the stress in the reflected pulse is opposite to the stress in the incidental pulse. This means that for the reflection from a free end, i.e. low soil resistance, the magnitude of the displacement doubles while it remains the same for the stress as can be seen in Figure 2.5a [Metrikine and Vrouwenvelder].

The same method as for the free end, can also be applied in case of a fixed end. In this case, i.e. stiff soil resistance an incident pulse propagates in the positive x -direction of $u_i(t - x/c)$. The reflection process and stress field is thereby describe by:

$$\begin{aligned} u(x, t) &= u_i(t - x/c) - u_i(t + x/c) \\ \sigma(x, t) &= \sigma_i(t - x/c) + \sigma_i(t + x/c) \end{aligned} \quad (2.3)$$

Hence, while the displacement in the reflected pulse is opposite to that of the incidental pulse, the stresses in the reflected wave are of the same sign. This causes a stress doubling and displacement wave of same direction during reflection as seen in Figure 2.5b [Metrikine and Vrouwenvelder].

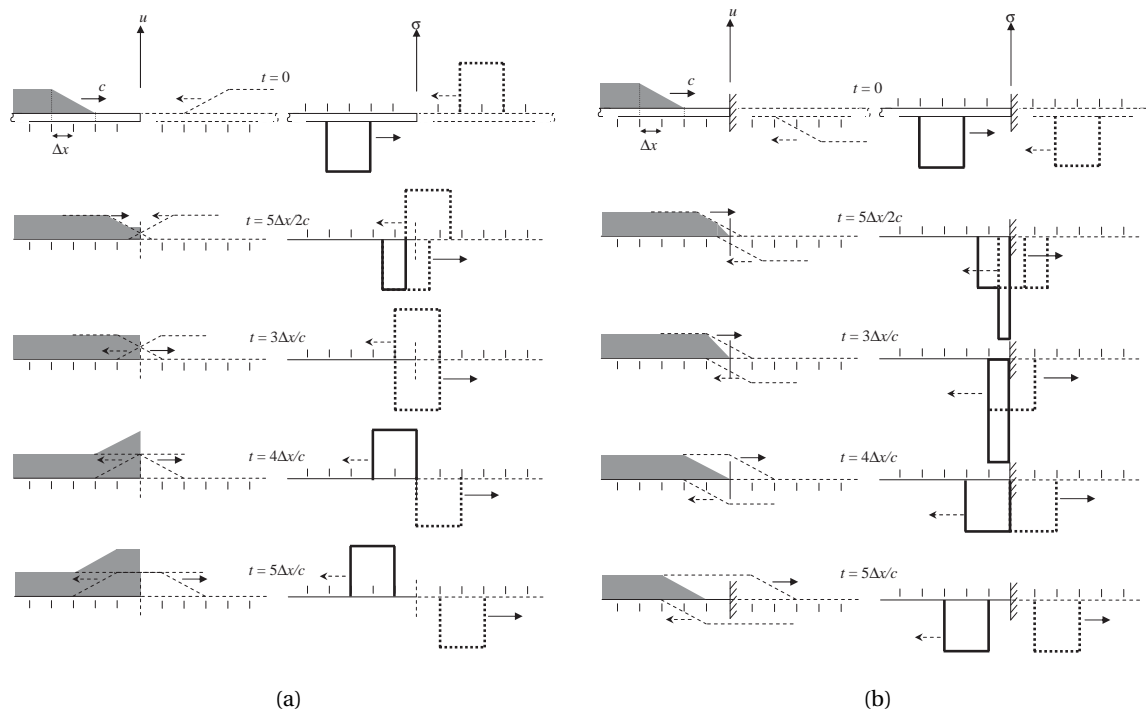


Figure 2.5: Reflection of the displacement and stress pulse from (a) free end (b) fixed end.

The radial displacement motion due to the effect of the Poisson's ratio of steel, caused by the compressional wave that is induced by the hammer impact, is according to Reinhall and Dahl [2011] the primary source of underwater sound. Since the wave speed of steel $c_p = 5120$ m/s is higher than that of water $c_w = 1490$ m/s, the compression wave produces an underwater pressure field in the shape of an axisymmetric cone, or Mach cone like the one shown in Figure 2.6 for a perfect vertical applied force. As soon as this wave enters the fluid layer, part of the energy is irradiated in the form of pressure waves into the fluid layer. Another part of the energy enters the soil and radiates outwards in the form of compression and shear waves. Some of these waves tend to "leak" into the fluid layer where they contribute to the sound at the receiver.

From Figure 2.6 it is clear that the wave front travels under an angle with the vertically oriented pile that can be calculated by $\phi_w = \sin^{-1}(c_w/c_p) = 17.2$ deg. Also it can be seen that due to the oscillation of the shell of the pile, multiple weaker pressure variations arise. After 6 ms the wave front in the pile reaches the bottom and is reflected with an angle of $\phi_s = \sin^{-1}(c_s/c_p) = 18.6$. Consequently a large part of the noise follows a zigzag path reflecting on the seabed and the ocean surface.

2.2.2. Pile driving using Vibratory Hammers

Vibratory pile driving is a complete different technique compared to impact hammering. Whereby the goal with impact hammering is to overcome the soil resistance, the goal with vibratory hammering is to eliminate the resistance of penetrating the pile in the soil. At the final end of installation no static pile capacity test can be executed since no resistance has been overcome. The result is an uncertainty in the industry whether the bearing capacity of the pile is achieved.

Vibratory pile hammers contain a system of rotating eccentric weights, powered by hydraulic motors. The eccentric weights rotate in direction counter to one another to cancel out the horizontal vibrations, while only the vertical vibrations are transmitted into the pile. This results of a periodic, low frequency force input character. The vibratory hammers are directly clamped to the pile, as can be seen in Figure 2.7, and therefore

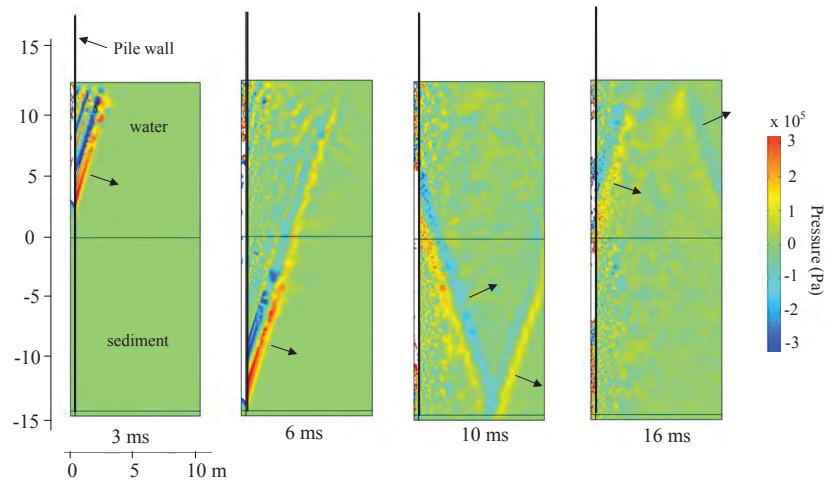


Figure 2.6: Underwater pressure field showing radiation from the pile after 3, 6, 10 and 16 ms after impact [Reinhall and Dahl; 2011].

make the pile handling much more efficient, while saving time and costs [Saleem; 2011].



Figure 2.7: PVE 300M Vibratory hammer clamped directly to a monopile.

The transmission paths for vibratory hammering are similar to that of impact piling. However the number of strikes differs significantly. With vibratory hammering the pile is struck with between 5 and 50 strikes per second. The impact energy of each strike is therefore less than for a impact hammer.

2.2.3. Pile driving using BLUE Piling

A new technique in pile driving is the one of BLUE Piling. Instead of using a steel ram as used in impact hammering, BLUE Piling uses the combustion of a gas mixture under a water column to create a pressure increase. This increase in pressure forces the water to accelerate upwards that already creates a relative smaller downward force acting on the pile. Thereafter the water column falls back under the force of gravity, creating a second downward force acting on the pile. Below the full working principle is described and illustrated in Figure 2.8.

1. Gas is fed into the combustion chamber
2. The gas is ignited and pushes the water out of the combustion chamber, a pressure increase pushes on the pile delivering the first blow.
3. The water then jumps in the air while the gasses expand further. The gasses remain in the combustion chamber.
4. The water jumps further until it reaches its highest point.
5. During the descent of the water column a percentage (roughly 50%) of the exhaust gasses is allowed to escape which makes the gas buffer stiffer. The water then falls on this stiff buffer and delivers the second blow.
6. The remaining exhaust gas is now allowed to escape and the cycle can be repeated.

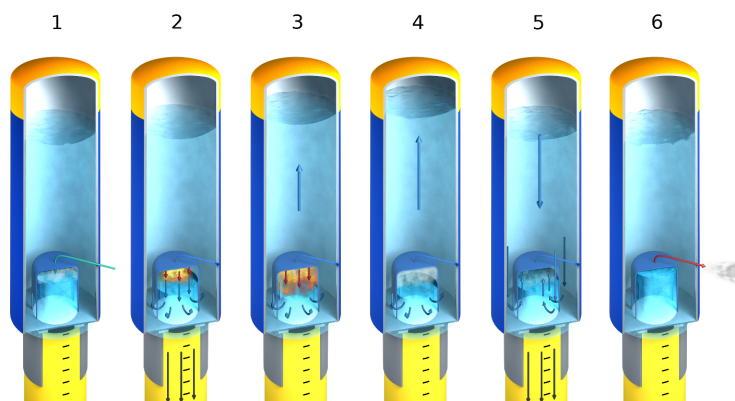


Figure 2.8: Operation cycle of a BLUE Piling hammer. [Fistuca; 2016]

Figure 3.4 shows the full impact diagram of the hammer. The first force increase is caused by the combustion of the gas in the hammer, and the second larger force build up results from when the water falls back. The last force build up is direct related to the previously falling water. This pushed the hammer a bit up and now falling down again. Therefore in total three blows are delivered to the system. An advantage of this system is that due to the large period of time in which the force excited by the falling weight of the water is transferred to the pile, approximately 0.2 sec, much lower tensile stresses occurs in the pile material. This results into less fatigue and less vibrations in the pile.

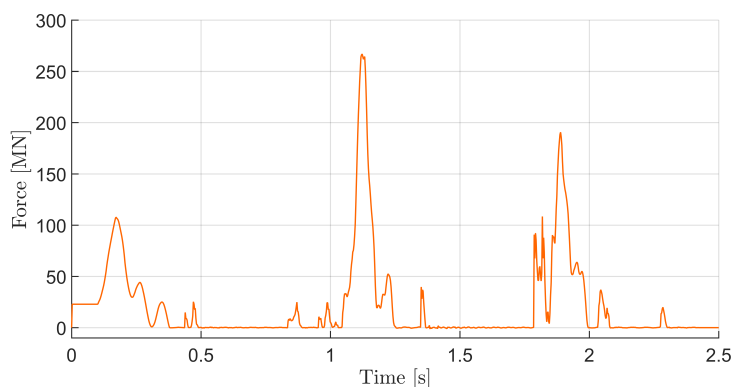


Figure 2.9: Entire Impact Diagram of the BLUE Piling hammer

2.3. Sound

Before going into the underwater acoustics during pile driving, it is of importance to understand what sound is. Sound is a disturbance in pressure that propagates through a compressible medium via the action of elastic stresses involving local compression and expansion of the medium. So by means of particle motions,

pressure differences occur. If there is an elastic medium which is capable of being compressed and extended between the vibrating particles sound will be detected. Depending on the strength of the vibrations, which defines their amplitude, a different loudness of the sound is experienced.

Sound can propagate in three principle modes, as illustrated in 2.10, through different media and based on the way the particles oscillate:

1. Longitudinal waves in air, fluid and solids
2. Transverse or shear waves in solids
3. Scholte waves at soil-water interface

In a longitudinal wave the displacement of the medium is parallel to the direction of energy transfer. Because of the longitudinal motion of the particles, there are regions in the medium where the particles are compressed together and other regions where the particles are spread apart. These regions are known as the compression and expansion respectively. In the compression regions high pressures occur, while in the rarefaction region a low pressure occurs and can propagate through air, fluid and solids because the energy travels through the atomic structure.

Transverse or shear waves oscillate perpendicular to the direction of energy transfer. During their propagation, every element of the medium experiences shear stress. Shear waves require a solid material that can encounter shear stress, and as a result cannot propagate in fluid or air.

The third wave of influence, the Scholte wave is a combination of a longitudinal and shear wave as it moves both vertically and horizontally in a perpendicular to the direction of energy transfer plane. This wave propagates at the soil water interface and decaying exponentially in both directions along the normal to the interface. Scholte waves propagate with a slightly lower speed than shear wave.

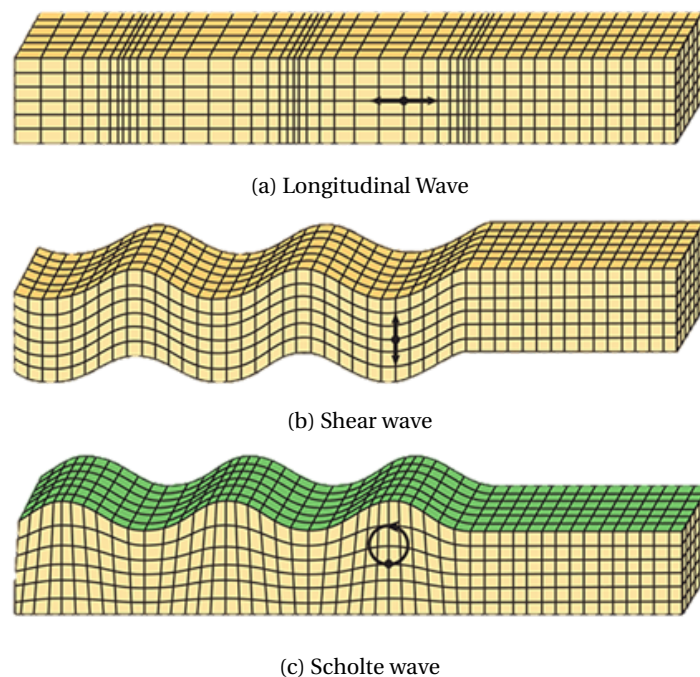


Figure 2.10: Propagating waves [Peterie et al.; 2014]

The sound wave is described by the scalar quantity sound pressure. Sound pressure is often simply defined as the difference between instantaneous total pressure and the equilibrium pressure. The latter being that pressure that would exist in the absence of sound waves. Sound pressure is in general the most useful acoustical quantity since it is relatively straightforward to measure, it is the quantity to which a hydrophone responds and the hearing organs of many species and marine life detect.

2.3.1. Sound attenuation

The further a wave travels from its source, the weaker it becomes. The decrease of amplitude with increasing distance from the source is referred to as attenuation. This is partly due to the geometry of the propagating wave, and partly due to the an-elastic properties of the material through which it travels.

The most important reduction is due to the geometric attenuation. If no material friction is considered, the energy loss in radial distance from the source is distributed over the surface of a hemisphere with area $2\pi r^2$. The intensity of the wave is the energy per unit area of the wavefront, and in radial distance this is expressed as:

$$I = \frac{E}{2\pi r^2} \quad (2.4)$$

This is the case for the compressional wave into the fluid layer and the compressional and shear waves propagating into the soil layer. For the Scholte wave, which travels at the soil water interface, the energy is spread out laterally. As a result, the initial energy is distributed over a circular cylindrical surface with a depth d . In radial distance, the intensity of a Scholte wave is given by:

$$I_s = \frac{E_s}{2\pi r d} \quad (2.5)$$

It can now be noticed that equation 2.4 shows the decrease in intensity in radial direction is proportional to $1/r^2$, while the decrease of the Scholte wave in equation 2.5 is proportional with $1/r$. The energy in a wavefront is proportional to the square of its amplitude. As a consequence, the amplitude of attenuation of normal waves and Scholte waves are proportional to $1/r$ and $1/\sqrt{r}$, respectively.

Another reason for attenuation is the absorption of energy due to not completely elastic properties. The particles in a medium do not react perfectly elastically when a waves travels through. As a result, part of the energy in the wave is converted to frictional heat and hence a decrease of amplitude result. This type of attenuation is referred to as damping. The damping of waves is described by the quality factor. It is defined as the fractional loss of energy per cycle of the wave:

$$Q_f = -\frac{2\pi E}{\Delta E} \quad (2.6)$$

In which ΔE is the energy lost in one cycle and E is the total elastic energy stored in the wave. It is conventional to measure damping by its effect on the amplitude of a wave, because that is what is observed during real time measurements. Accordingly, the quality loss is first rewritten as a function of the distance it travels. Thereafter, with the fact that the energy in a wave is proportional to the square of the amplitude, the energy difference is rewritten dependently by the amplitude difference. Solving the final equation, results in the damped amplitude of a wave at distance r from the pile:

$$\begin{aligned} \frac{2\pi}{Q_f} &= -\frac{1}{E} \lambda \frac{dE}{dr} \\ \frac{1}{E} dE &= -\frac{2\pi}{Q_f \lambda} dr \\ \frac{2}{A} dA &= -\frac{2\pi}{Q_f \lambda} dr \\ A &= A_0 \exp\left(-\frac{\pi r}{Q_f \lambda}\right) \\ A &= A_0 \exp\left(-\frac{r}{D}\right) \end{aligned} \quad (2.7)$$

As can be noticed from the equation, the amplitude decays more rapidly for low quality factor or short wavelength. This means that a material with a low wave velocity and hence high elasticity modulus, transmits a wave with relatively high energy loss by absorption. As a results, high frequency waves with a short wavelength make more cycles per second and hence lose more energy. High frequencies are attenuated more rapidly than lower frequencies [Lowrie; 2007].

2.3.2. Sound notation

Sound levels and other acoustic parameters vary over a wide range, therefore the values relating to sound are measured in a logarithmic unit named decibels [dB]. A decibel is a ratio of intensities. Two intensities I_1 and I_2 have a ratio I_1/I_2 in decibels of $10\log(I_1/I_2)$ dB. Ratios can only be calculated in relation to a reference pressure. This reference pressure is usually different in water and in air. The presently accepted and chosen by US Navy in 1970, reference intensity is the intensity of a plane wave having a root-mean-square pressure equal to 10^{-6} pascals or $1 \mu\text{Pa}$. In air the reference pressure p_r is $20 \mu\text{Pa}$. Pressure ratios are expressed in dB re $1 \mu\text{Pa}$ by taking the $20\log(p_1/p_r)$. The conversion from one scale to another can be expressed by:

$$\begin{aligned}\Delta dB &= 20\log_{10}\left(\frac{p_{r,air}}{p_{r,water}}\right) \\ \Delta dB &= 20\log_{10}\left(\frac{20}{1}\right) = 26dB\end{aligned}\quad (2.8)$$

Sound caused by pile driving activities are non-continuous sounds that are characterized by short bursts of acoustic energy of finite duration. The most appropriated definitions for use with non-continuous sounds are [Robinson et al.; 2014]:

1. Sound Pressure Level (SPL)
2. Single pulse Sound Exposure Level (SEL)
3. Peak Sound Pressure Level
4. Peak-to-Peak Sound Pressure Level

Sound Pressure Level

Sound Pressure Level is used in both continuous and non-continuous sounds. Acoustic pressure readings vary above and below a mean value with time. To allow for this variation, the Sound Pressure Level is averaged over a specified period of time.

$$SPL = 20\log_{10}\left(\frac{p_{rms}}{10^{-6}}\right), \text{ in dB re } \mu\text{Pa} \quad (2.9)$$

Sound Exposure Level

The Sound Exposure Level is a logarithmic measure of the sound exposure of a sound relative to a reference value over a finite time period by:

$$SEL = 10\log_{10}\left(\frac{1}{t_0} \int_{t_1}^{t_2} \frac{p^2}{10^{-12}}\right), \text{ in dB re } \mu\text{Pa}^2\text{s} \quad (2.10)$$

That eventually results in the energy content of a pulse. The time duration of the pulse is commonly defined as the time occupied by the central portion of the pulse, where 90% of the pulse energy resides. This makes it easy to state the start and end of a pulse. Figure 2.11 shows the determination of the time duration of a pulse.

Peak Sound Pressure Level

The peak sound pressure level is the maximum sound pressure during a stated time interval. A peak sound pressure arises from a positive or negative sound pressure and is calculated by:

$$L_{peak} = 20\log_{10}\left(\frac{p_{peak}}{10^{-6}}\right), \text{ in dB re } \mu\text{Pa} \quad (2.11)$$

Peak-to-Peak Sound Pressure Level

The sum of the peak compressional pressure and the peak expansional pressure during a stated time interval and calculated by:

$$L_{peak-to-peak} = 20\log_{10}\left(\frac{p_{peak-to-peak}}{10^{-6}}\right), \text{ in dB re } \mu\text{Pa} \quad (2.12)$$

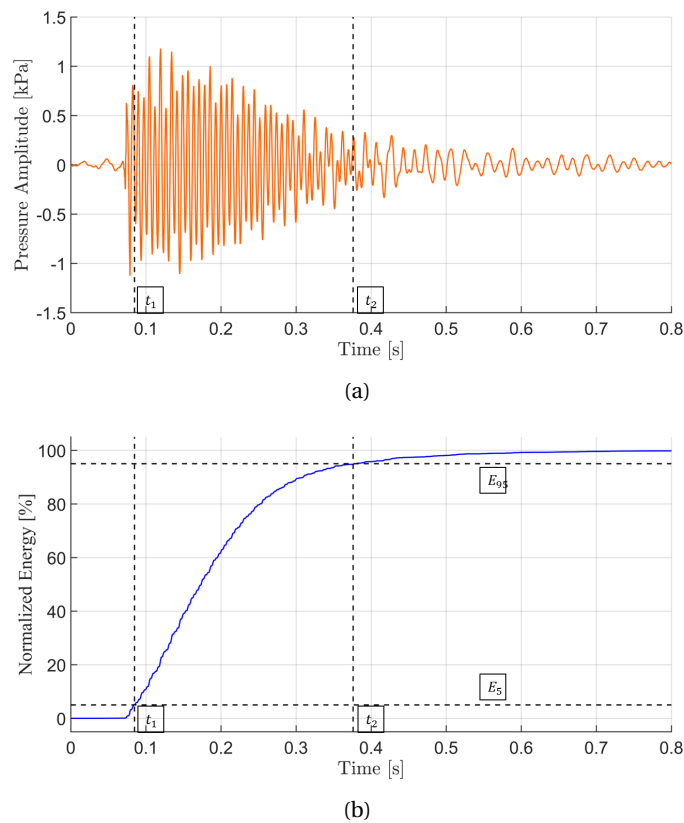


Figure 2.11: Calculation of pulse duration over pulse for SEL

Strictly, the use of decibels for peak levels of pulsed sound waves is somewhat controversial because decibels were originally used only for quantities that may be related to the time-averaged power. However, the usage has now become common practice.

2.3.3. Underwater Noise

In the previous section, the most common sound notations are given that can also be referred to as noise notations. The only difference between sound and noise is that noise is unwanted or unpleasant sound. The classification of sound as noise is therefore highly subjective. People are able to indicate whether sound is wanted or not, but for the marine life this is much more difficult. At least for people to understand. This makes underwater noise a highly important and interesting topic.

One important characteristic of underwater sound compared to noise above water is the speed. The speed of sound underwater varies significantly from speed of sound in air as the two medias have different properties. Sound travels faster through a medium with low compressibility and/or lower density as indicated by equation 2.1. Water has a higher density and is harder to compress, so higher elasticity modulus than air. This results in an increase of about 4.3 times the speed of sound of air in water. Finally resulting in sound traveling around 4.3 times faster, and thus also further, through water than air. Making piling noise audible from background noise up to 80 km from the piling source. Exposure of marine life to increased sound levels can have severe effects and where therefore categorized, in order of decreasing severity [Bailey et al.; 2010]:

1. Auditory injury or permanent threshold shift in hearing (PTS)
2. Temporary threshold shift in hearing (TTS)
3. Behavior disturbance
4. Audibility

To protect the marine life of TTS happening, regulations were set by nations involved in offshore pile driving. As of January 2014, the FF Act (species protection) and the NP Law (habitat protection) became applicable on

the Exclusive Economic Zones (EEZ) . Stating that for any human activity that possibly has a negative impact on the marine environment or marine protected species, a permit through the NP law and exemption of the FF Act is required [Haskoning; 2015]. Regulations on underwater noise mitigation differ greatly between the countries bordering the North Sea and Baltic Sea. They border on nine countries that have their EEZ in this area; Germany, the United Kingdom, the Netherlands, Belgium, Denmark, France, Sweden, Poland and Norway. Standard regulations in each country include the use of Acoustic Deterrent Devices (ADD) and a soft start. In some countries additional regulations have been implemented. Some of these are elaborated in the oncoming section and summarized in Table 2.1.

In the Netherlands a seasonal restriction is implemented between January and July, in addition to the standard regulation by the NP law and FF Act. The regulation focus mainly on the harbour porpoise as they see this species as most sensitive. Other conditions can be implemented in the permit depending on location and period.

The German underwater noise procedures based on regulations are assigned by the Federal Maritime and Hydrographic Agency (BSH). The regulations in the German EEZ state that the involved parties must do everything within their power to generate as less noise as possible. The legislation is set to a maximum SEL of 160 dB re 1 μPa^2 s and a peak level of 190 dB re 1 μPa s at 750 m from the piling source. The noise levels must be measured within the lower one-third of the water column and the parties must use one or more noise mitigation systems to decrease the sound levels when necessary. There are no seasonal restrictions [UBA; 2011] [Faijer; 2014].

The largest part of the North sea is regulated by the United Kingdom. Where German legislation is mostly based on setting sound limits, United Kingdom legislation focuses on the present marine life. They are known for their obligatory use of Marine Mammal Observers (MMO). Noise reduction measures are not mandatory, but marine mammal deterrence and soft start of piling is. The United Kingdom also implements seasonal restrictions based on fish breeding season.

Belgium and Denmark, like in Germany, implemented a noise threshold. Belgium has set a peak level of 185 dB re 1 μPa s at 750 m from the source. This is comparable with the 190 dB re 1 μPa s of the Germans. In Denmark harbour porpoises should not be exposed to a SEL of 183 dB re 1 μPa^2 s or more. This noise threshold is based on a model which takes into consideration that the marine mammals have been scared up to 2 km away from the source. In France, no piling of offshore wind farms is allowed. As a results their are no noise regulations.

Table 2.1: Comparison of regulations for noise mitigation per country [Haskoning; 2015]

Country	Noise threshold	Noise mitigation	Seasonal restriction	Marine Mammal Detection	Marine Mammal Deterrence
Netherlands	No	No	Yes <i>January-July</i>	No	Yes <i>ADD and soft start</i>
Germany	Yes <i>SEL at 750 m: 160 dB</i> <i>SPL at 750 m: 190 dB</i>	Yes	No	No <i>C-PODs</i>	Yes <i>ADD and soft start</i>
United Kingdom	No	No	Yes <i>fish breeding season</i>	No <i>MMO</i>	Yes <i>ADD and soft start</i>
Belgium	Yes <i>SPL at 750 m: 185 dB</i>	Yes	Yes <i>May-August</i>	No	Yes <i>ADD and soft start</i>
Denmark	Yes <i>SEL at 750 m: 183 dB</i>	No	No	No	Yes <i>ADD and soft start</i>
France	No piling allowed for offshore wind farms				
Norway	No	No	No	No	No
Poland	No	No	No	No	No
Sweden	No	No	No	No	No

2.3.4. Underwater noise mitigation

In order to mitigate the noise to meet the legal requirements, it is of importance to understand how the noise propagates. This differs a lot with soil conditions, pile size and hammer type. Figure 2.12 shows the noise propagation after the hammer strikes the pile. Sound is generated in the air surrounding the hammer and pile. This sound may enter the water via the airborne path, where airborne noise is incident upon the air-water interface and a portion of the sound enters the water layer. However, of more significance in underwater noise is the radiation of noise from the pile surface as a consequence of the compressing and expanding waves that travel down the pile. Due to the direct contact of pile and water, waves in the submerged section of the pile may efficiently couple into waves traveling in the water and therefore highly contribute to the noise level. This path may be referred to as the primary noise path.

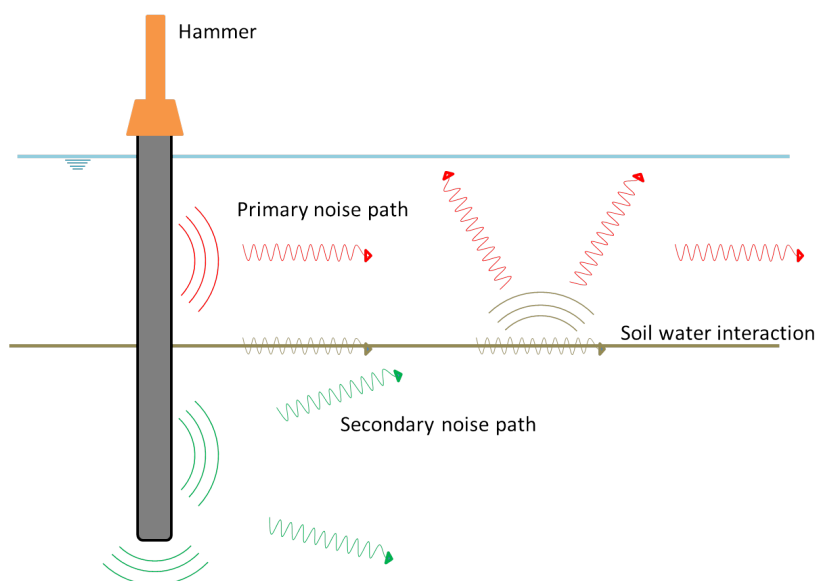


Figure 2.12: Wave propagation during piling in monopile, soil and water

Last is the secondary noise path caused by the elastic waves traveling down the pile and inducing lateral waves in the seabed. These travel as discussed in section 2.3 as compressional and shear waves through the soil. Thereby also Scholte waves occur that travel outwards through the seabed and leak vibrations into the water layer, contributing to the sound level in the water. Soil has a much higher damping factor than water, causing the high frequencies to be damped out in the soil. Therefore the secondary noise path mainly contains of relative low frequency waves. As discussed in section 2.1.2, the monopiles now being installed or in the near future, are increasing in size and therefore the natural frequency shifts towards the lower frequencies. Causing more noise to travel through the soil and from there radiate into the water following the secondary noise path. However, no noise mitigation system is able to mitigate this path yet making the need for a different method of reducing underwater noise levels of extra of interest.

3

System Parameters

This section describes the input parameters that are selected for the acoustic models discussed in chapters 4 and 5. For this research, extra attention is given on investigating the effect of the force distribution over time of the hammer on the noise levels for very large monopiles. Subsequently, section 3.2 introduces the large duration impact diagram of the BLUE Piling hammer which is used later to examine the noise propagation. Finally, section 3.3 describes both the separate and overlapping parameters as inserted in both acoustic models.

3.1. Soil Data

The soil input data is obtained by means of a Cone Penetration Test (CPT), for the cone resistance of shaft and tip. From more comprehensive data, Table 3.1 is obtained for more specific data as the saturated density and friction angle. The table also shows the inserted unit tip resistance obtained from CPT.

Table 3.1: CPT data

Layer	Depth	Material	Saturated density	Constant volume friction angle	Average measured total cone resistance	Measured friction value
	<i>m</i>	–	<i>kN/m³</i>	°	<i>MN/m²</i>	<i>kN/m²</i>
S1	2.0	Sand	19	20	8	-
S2	10.2	Sand	19	30	20	-
S3	16.9	Sand	19.5	35	45	-
C1	19.7	Clay	20	-	5	200
S4	23.2	Sand	20.5	37.5	55	-
S5	24.7	Sand	21	30	22.5	-
C2	26.2	Clay	20	-	10	200
C3	28.1	Clay	20	-	5	200
S6	29.9	Sand	21	37.5	70	-
S7	32.4	Sand	20.5	38	100	-
S8	37.0	Sand	21	37.5	80	-

For later purpose, the data provided by the CPT analysis must first be converted in terms of SRD . This is the static resistance to driving of the pile. The major contribution to SRD is due to the side friction, and a realistic model for friction during driving is therefore of importance. This is done according to the method described by Alm and Hamre [2001] where drivability predictions are based on the fact that ultimate shaft friction, that can develop in a given layer, decreases as the pile tip penetrates deeper. This phenomenon is referred to as the friction fatigue concept.

The general formulation for the unit shaft friction along a pile during driving is:

$$f_{shaft} = f_{sres} + (f_{si} - f_{sres})e^{k(d-p)} \quad (3.1)$$

In order to obtain the final shaft friction, a distinction is made between clay and sand since these react different. For clays, the initial friction is taken as the recorded CPT sleeve friction, while the residual friction is a function of the normalized cone tip resistance by:

$$f_{sres} = 0.004q_t \left(1 - 0.0025 \frac{q_t}{p'_0}\right) \quad (3.2)$$

For sands this is slightly different. Instead of obtaining the initial friction from CPT, the basic static friction formulation is taken:

$$f_{si} = K \cdot p'_0 \cdot \tan(\delta) \quad (3.3)$$

In which the stress Kp'_0 and constant volume friction angle δ is calculated by:

$$Kp'_0 = 0.0132q_t \frac{p'_0}{p_a}^{0.13} \quad (3.4)$$

$$\delta = (\phi - 5)$$

For the residual friction, a best fit was found by Alm and Hamre [2001] of 20% of the initial friction for sand. The shape factor k that encounters for a fast degradation in dense sand and the opposite for soft clay is constructed by:

$$k = \frac{\frac{q_t}{p'_0}^{0.5}}{80} \quad (3.5)$$

The unit tip resistance and unit shaft resistance that serve as input for the GRLWEAP program in the next section can be obtained. For the unit shaft resistance this equals f_{shaft} from equation 3.1. For the unit tip resistance take for clay 60% of the total cone resistance, and for sand:

$$f_{tip} = 0.15q_t \left(\frac{q_t}{p'_0}\right)^{0.2} \quad (3.6)$$

The total static resistance to driving is thereafter calculated by its contribution of the pile tip resistance and shaft resistance along the pile. This approach does not take plugging into account. Therefore also internal resistance must be taken into account by reducing the unit friction to 50% and applying on both inside and outside of the shaft. Finally this results in the SRD by the summation of the SRD for the shaft and the SRD for the tip by equation 3.7. This is often used to predict the amount of blowcounts for the hammer. For the Upper Bound Resistance the effect of soil variability is taken into account. Therefore a factor of 1.25 is applied to cater for this effect as stated by Alm and Hamre [2001]. Finally the calculation results in a best estimate SRD value at final penetration of 235 MN and upper bound of 294 MN.

$$\begin{aligned} SRD_{shaft}^{out} &= SRD_{shaft-1} + \Delta d \cdot f_{shaft} \cdot A_{out} \\ SRD_{shaft}^{in} &= SRD_{shaft-1} + \Delta d \cdot f_{shaft} \cdot A_{in} \\ SRD_{tip} &= f_{tip} \cdot A_{tip} \\ SRD &= SRD_{shaft}^{out} + SRD_{shaft}^{in} + SRD_{tip} \end{aligned} \quad (3.7)$$

3.1.1. Impact Diagram

The impact force is the force that develops between hammer and pile during the blow and the diagram diagram shows how the impact force varies with time [Voitus van Hamme et al.; 1974]. The impact diagram serves as input for the acoustic models on which will be elaborated more in chapters 4 and 5. For the validation of both models, a similar impact diagram as used in reality must be obtained as input. Unfortunately,

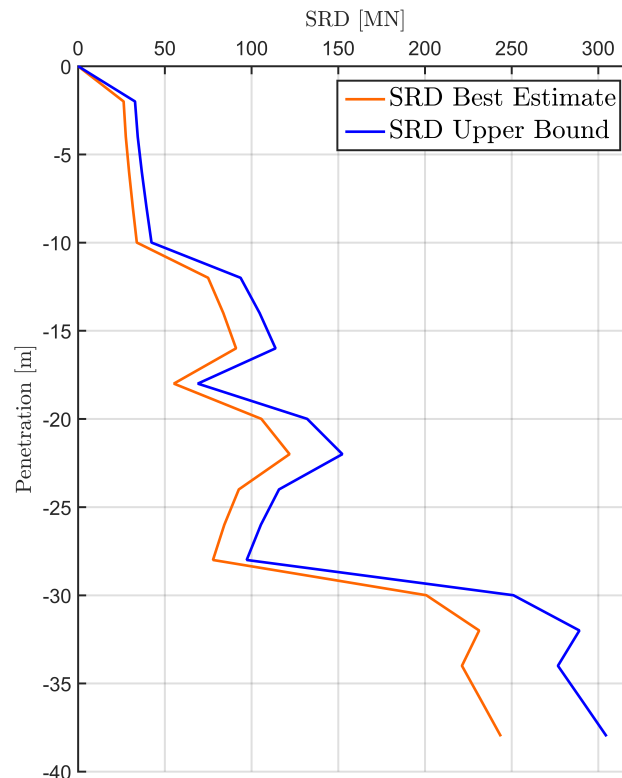


Figure 3.1: Static resistance to driving as function of penetration

this is not measured data from the project itself and as a results it is obtained by computer models. Use is therefore made of the program GRLWEAP. This is a pre-driving computational analysis tool for simulating pile response based on the solution of one-dimensional wave equation which is a broadly used program to predict drivability and select a suitable hammer for a project. A more detailed description of the working principle of the program is given in chapter 6.

The main inputs in GRLWEAP are hammer, cushion, pile specifications and soil parameters. For the hammer, a large data file is provided within almost all commercially available hammers are available. This data contains information as fall heights of masses, velocity and weight of the mass and system. Soil data is inserted as unit shaft f_{shaft} and unit tip f_{tip} resistance per depth as obtained from section 3.1 and presented in Table 3.2. Pile data consists of total length, cross section area, elastic modulus of material and material density.

From the drivability predictions a maximum amount of energy of 2100 kJ was predicted for the piling process. However, from the piling data log a maximum value of only 1800 kJ was needed to drive the pile at its final penetration depth. To obtain an identical impact diagram, the energy amount has been adjusted in GRLWEAP to 1800 kJ by changing the fall height of the mass. The amount of energy needed to pile during stage 1,2 and 3 is similar resulting in the three impact diagrams as shown in Figure 3.2.

Interesting is the difference in the reflected wave for stage 1,2 and 3 which is visible in the second bump in the impact diagram. This is caused by the difference in resistance at the tip of the pile as discussed in section 2.2.1, where the process has been simplified for a reflecting wave at a free and fixed end rod. Inserting these impact diagrams would result in an overestimation of the noise predictions due to the presence of the reflected wave. In both acoustic models adding the reflected wave would result in an extra energy input even though this is not the case in reality. Therefore, as shown in Figure 3.3, it is here adopted that omission of the reflected wave results in a more realistic outcome and the impact diagrams for the different stages are adjusted to only the main impact pulse.

Table 3.2: Unit shaft f_{shaft} and unit tip f_{tip} resistance per depth as obtained from section 3.1

Layer	Depth m	Material	Unit Shaft Resistance kN/m^2	Unit Tip Resistance kN/m^2
S1	2.0	Sand	0	0
S2	10.2	Sand	122	12147
S3	16.9	Sand	412	23202
C1	19.7	Clay	200	3000
S4	23.2	Sand	604	25704
S5	24.7	Sand	191	8479
C2	26.2	Clay	200	60000
C3	28.1	Clay	200	3000
S6	29.9	Sand	779	33644
S7	32.4	Sand	1148	50670
S8	37.0	Sand	915	37913

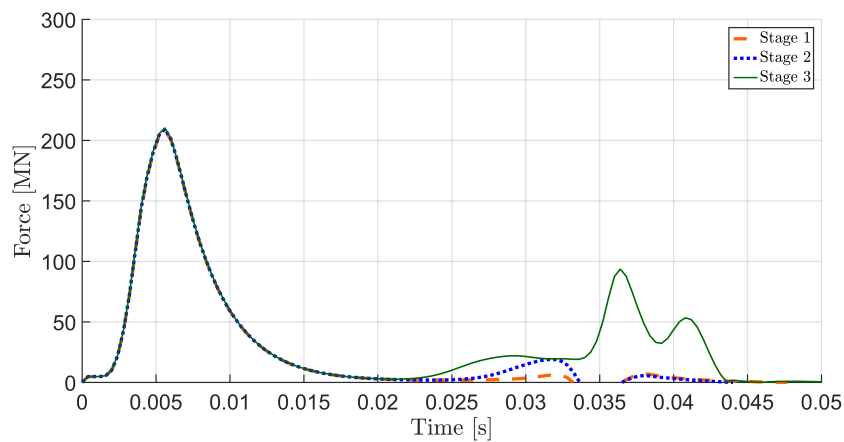


Figure 3.2: Impact diagram of impact hammer at stage 1, stage 2 and stage 3

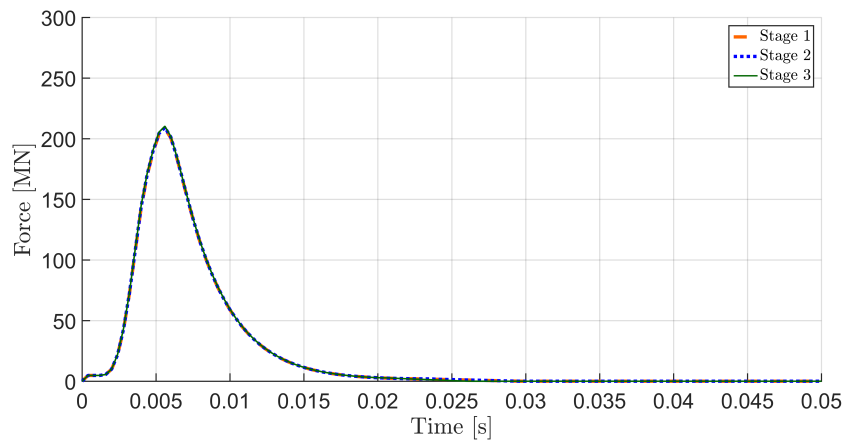


Figure 3.3: Impact diagram of impact hammer at stage 1, stage 2 and stage 3 for impact only

3.2. Additional Impact Diagram

In previous section, the derivation from GRLWEAP of the impact diagram of an impact hammer has been described. The impact diagram of an impact hammer gives a short pulse which induces high dynamic response in the pile. Consequently, high vertical and radial velocities in the pile occur during impact. Reducing these

velocities, might result in less dynamic motions and thus less fatigue in the monopile. A method to do so, is by increasing the force distribution over time. When the duration is sufficient long, there is no possibility of reflecting waves in the pile and therefore only compressional waves occur. possible. A hammer that is capable of doing this is the BLUE Piling Hammer as introduced in section 2.2.3

Since the BLUE Piling technique is relatively new, GRLWEAP has only very recently inserted this option in their program. The working principle however is the same as for an impact hammer whereby the soil resistance force has to be overcome. Followed by sliding of the pile as long as the force exceeds this resistance force determines the amount of penetration into the soil.

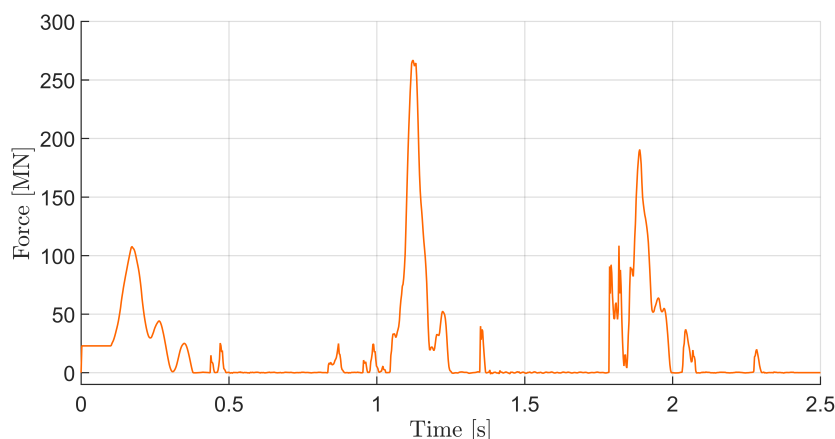


Figure 3.4: Impact diagram of BLUE Piling hammer at stage 3

3.3. Model Specific Parameters

This section describes the data needed for the acoustic models. For both models, the monopile is assumed to have a constant diameter over length. This differs from reality where the monopile has a conical shape for the first approximate 30 m from top. The constant geometry and material characteristics that are identical for both models are summarized in Table 3.3. The oncoming two subsections will discuss for each individual model the standard input parameters. In section 4.2 and section 5.2 a brief introduction to the interface of the model is given in more detail.

Table 3.3: Material constants and geometrical parameters of the pile

Parameter	Value	Unit
E	$2.1 \cdot 10^{11}$	N/m^2
ν	0.28	-
ρ	7850	kg/m^3
η	0.001	-

3.3.1. Spring Dashpot Model

The extent to which the pile is driven has a potentially large impact on the overall noise transmitted in the fluid and soil. This is due to the different penetration depth and therefore different damping characteristics. Therefore, the model input has been simplified to three different stages that are defined in Table 3.4. Stage 1 has a penetration of 16.5 m, Stage 2 a depth of 26.5 m and Stage 3 a penetration depth of 36.5 m when the installation is practically finished. Stage 1 has been chosen so that the impact piling system is at its maximum energy input and therefore these different stages can better be compared.

Table 3.5 shows the parameters for the fluid and the soil layer. The Spring Dashpot model has, in contrast to the Elastic medium model, the ability to include the inner fluid in the pile.

Table 3.4: Different stages during installation

Parameter	Value			Unit
	Stage 1	Stage 2	Stage 3	
z_0	24.5	14.5	4.5	m
z_1	24.5	14.5	4.5	m
z_2	63.5	53.5	43.5	m

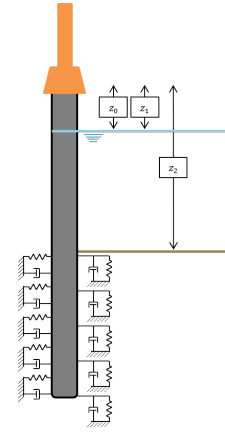


Figure 3.5: Basic geometry of the model in 2D together with parameters for different stages during installation

Table 3.5: Fluid and Soil properties that serve as input for the Spring Dashpot model

Layer	Depth m	ρ kg/m^3	c_p m/s	E MN/m^2	ν
Inner Fluid	75.5	1025	1490	-	-
Outer Fluid	39	1025	1490	-	-
Soil	36.5	2000	-	50	0.40

3.3.2. Elastic Medium Model

When sound waves interact with the seabed, the structure of the seabed surface becomes important. Bottom sediments are often modeled as fluids which means that they support only compressional waves. This is often a good approximation since the rigidity (and hence the shear speed) of the sediment is usually considerably less than that of a solid layer. When willing to take into account the complete bottom interaction till a reasonable depth, another method must be applied to account for all propagating waves. Meaning the medium must be modeled as elastic and hence supporting both compressional and shear waves. For the Elastic Medium model, the soil is therefore modeled as a viscoelastic medium that extends beyond the tip of the pile. Table 3.6 gives a summary of all included layers during the three stages. The first layer z_1 is defined as the distance from pile head to water surface. The next layer z_2 represents the seabed distance from pile head and z_3 the extra medium below the pile tip to account for propagating waves through the soil.

Table 3.6: Different stages during installation, including soil layer

Parameter	Value			Unit
	Stage 1	Stage 2	Stage 3	
z_1	24.5	14.5	4.5	m
z_2	63.5	53.5	43.5	m
z_3	20	20	20	m

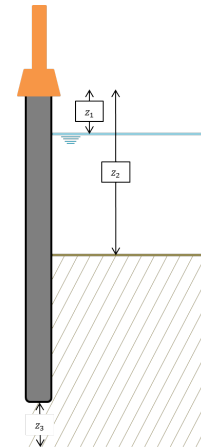


Figure 3.6: Basic geometry of the model in 2D

The major advantage of the Elastic Medium model is the ability to account for shear and Scholte waves prop-

agating through the soil. Attenuation of energy during their propagation in the soil reduced the amplitude of the vibrations with increasing distance from the source. The decay of amplitude of vibration with distance can be attributed to two components; geometric (radiation) damping and material damping. The geometric damping occurs due to the decrease of the energy density with distance from source. The material damping coefficient can be analytically determined by assessing the type of the propagating wave and material conditions.

The geoacoustic information required for the viscoelastic bottom model includes the following material properties: The compressional wave speed c_p , the shear wave speed c_s , the compressional wave attenuation α_p , the shear wave attenuation α_s , and the density ρ . From CPT data it is clear that the main soil material is sand. By previous work from Hegazy and Mayne [1995], an empirical correlation between cone tip resistance and shear wave speed is known by:

$$c_s = (10.1 \log(\bar{q}_c) - 11.4)^{1.67} \cdot (rf100)^{0.3} \quad (3.8)$$

In which \bar{q}_c is the average cone tip resistance and rf the friction ratio in percentage. The shear and Scholte wave propagation, later shown in the results, are mainly vertical polarized and hence most influenced by the upper soil layer. As a consequence, the medium dense sand layer is inserted and used as reference case for the complete soil layer. Later in section 5.5 the sensitivity of selecting the soil parameters is discussed during a parametric study.

An average tip resistance for the first soil layer till 10 m of 10 MPa and a friction factor of 1% results in a shear wave speed of 270 m/s. According to the same work by Hegazy and Mayne [1995], the soil unit weight is derived from the shear wave speed using the empirical formula:

$$\gamma = (8.32 \log(c_s) - 1.61 \log(z)) \quad (3.9)$$

where z is the depth in the soil. Finally, the density of the soil is calculated by $\rho = \gamma/g$. Table 3.7 lists the results that serve as input for the Elastic medium model.

Table 3.7: Fluid and Soil properties that serve as input for the Elastic Medium model.

Layer	Depth m	E MN/m^2	ν -	ρ kg/m^3	c_p m/s	c_s m/s	α_p dB/λ	α_s dB/λ
Fluid	39	-	-	1025	1490	-	-	-
Medium dense sand	36.5	420	0.487	1936	1697	270	1.2	3.8

The obtained value of the compressional wave attenuation in the soil are similar to those adopted in table 4.18 of [Ainslie; 2010], representative for the soil conditions in the German North Sea. The obtained value of the shear wave attenuation is by $0.01 c_s$ from [Fricke and Rolfes; 2015]. In order to account for the rigid seabed below the pile tip and due to the large amount of low frequency waves traveling as shear waves due to the large size monopile, the attenuation factors found in literature are increased with 25%.

3.4. Conclusions

In this chapter, the system parameters as adopted are introduced. First, an introduction of the project is given. This project serves as reference case due to the large size monopiles installed. One of the monopile was installed without any noise mitigation measures, and is thus applicable as reference pile for the acoustic models. From the obtained soil data at the location, the impact diagram used to drive the pile is obtained the drivability program GRLWEAP. Additionally, the impact diagram from the new pile driving method, BLUE Piling, is obtained. Subsequently, the model specific parameters are discussed. For both the Spring dashpot model and the Elastic Medium model different input parameters are derived. The selection of parameters in this chapter forms the basis of model analysis in chapter 4 and 5.

4

Spring Dashpot Model

This chapter will discuss the first of the two Acoustic models used during this thesis, namely the Spring Dashpot model. The propagation of mechanical disturbances in layered acousto-elastic media is addressed using the normal mode method. This approach is common when taking into account wave propagation in acoustics. Another method is by using the wavenumber integration approach which is not dependent on the pole contributions being dominant. However, the modal methods are mainly preferred because of their robustness and computational efficiency [Jensen et al.; 2011]. The normal mode method involves solving a depth-dependent equation that has a set of modes of vibration of the shell structure. The frequencies of these vibrations give the horizontal wavenumbers which are finally associated with the modal propagation. The complete acoustic field is then constructed by summing up contributions of each of the modes weighted in accordance to the source depth.

After the Spring Dashpot model working principle is discussed in section 4.1, a brief description of the input interface and available settings is given in section 4.2. In order to make sure the model predictions are in line with reality, a validation has been conducted in section 4.3. In section 4.4, a parametric study is presented where the influence of enlarging the time period of an impact diagram is discussed for the frequency spectrum in the exterior fluid layer, pressure levels and final sound exposure levels. Finally, section 4.5 concludes on the efficiency and accuracy of the model.

4.1. A 3-D spring dashpot model

The geometry of the model is shown in Figure 4.1. In this model, the pile is modeled as a thin elastic circular cylindrical shell of constant thickness and finite length. The shell is surrounded by fluid at $z_1 < z < z_2$. For this layer it is assumed to have the same properties as an ideal fluid and therefore has no viscosity. Thereby the fluid is compressible, since otherwise shock and sound waves cannot exist. At $z_2 < z < L$ the shell is surrounded by distributed springs and dashpots in all directions to model the soil layer. The interior of the shell is filled with fluid from $z_0 < z < L$ and the hammer is modelled as an external force applied at the top of the pile.

Compared to other studies in which the fluid problem is treated by boundary integral conditions, this model is based on the separation of variables. In here the coupling of the shell vibrations with the surrounding fluid is accomplished by the fluid pressure acting on the surface of the shell which is expressed in terms of the in vacuo shell modes. This is known as the modal domain decomposition, which is common to use when interested in analyzing the behavior of mechanical structures. A major advantage of using the modal domain for the coupling is that the vibrations of a finite length shell together with the surrounding fluid and the soil domains are integrated into a single model. By using a system of coupled algebraic equations, the system can be solved with high accuracy.

The model is based on 4 different calculation stages that have to be encountered. The first stage considers the vibrations of the shell, the second stage treats the exterior fluid region, the third deals with the interior fluid and the last one considers the forced vibrations of the complete system. The overall structure of the model is based on a single equation where the vibrations of the shell structure, together with those of the surrounding

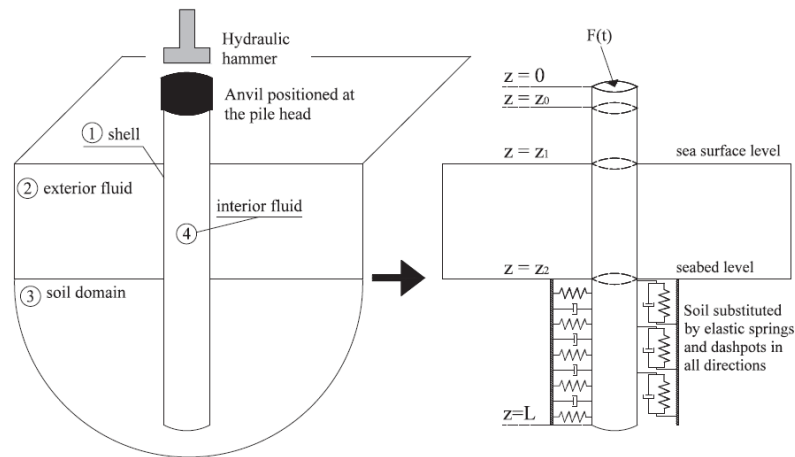


Figure 4.1: Geometry of the model Tsouvalas and Metrikine [2013]

fluid are described by a set of coupled partial differential equation.

As stated by Jensen et al. [2011] the wave equation in an ideal fluid can be derived from hydrodynamics and the adiabatic relation between pressure and density. By assuming Newton's second law in an adiabatic process and linear approximations, the acoustic wave equation, which only involves first-order terms are derived. Thereafter considering that the time scale of oceanographic changes is much longer than the time scale of acoustic propagation, it can be assumed that the material properties like density and speed of sound are independent of time. This finally results into a wave equation for pressure:

$$\rho \nabla \left(\frac{1}{\rho} \nabla p \right) - \frac{1}{c^2} \frac{\partial^2 p}{\partial t^2} = 0 \quad (4.1)$$

If the density is constant in space equation 4.1 can be replaced by the standard form of the wave equation:

$$\nabla^2 p - \frac{1}{c^2} \frac{\partial^2 p}{\partial t^2} = 0 \quad (4.2)$$

For the exterior fluid domain, Tsouvalas and Metrikine [2015] uses the velocity potential to describe the fluid motions. This potential is dependent on the radial, circumferential and axial coordinate in time. By transforming to the frequency domain, a reduction in the dimensions of this partial differential equation is possible which is simpler to solve than the full wave equation [Agilent Technologies; 2000].

To do so, a few boundary conditions need to be satisfied in the exterior fluid domain:

- Fluid particles must stay connected to the outer shell layer of pile
- Water surface is defined as a pressure release boundary
- Soil water interface is either defined as a rigid boundary or impedance boundary

The fluid layer and shell are treated as separate systems. However, for a reliable case these involve interaction between both boundaries. In order to find the response of the system, use is made of the modal expansion with respect to the in vacuo modes of the shell. This is based on a few steps as described below:

1. Solution of the eigenvalue problem for the shell without the presence of the fluids and the soil
2. Solution of the governing equations for the inner and external fluid domain by expressing the interface conditions at the shell-fluid contact surface in modal domain.
3. Solution of the coupled system of equations resulting from the substitution of the obtained solutions for the shell and the fluid domains into the interface conditions. And the use of proper orthogonality conditions of shell and fluid modes.

The hammer is modelled as an impact force exerted at the pile head. In contrast to other studies the force here is allowed to have an inclination to the vertical in order to excite axially asymmetric modes as well. During operations, a maximum tolerance of $\pm 0.25^\circ$ is allowed. With an average peak force of 210 MN applied, this results in a maximum horizontal force of a bit less than 1 MN. Consequently this will have an influence on the circumferential modes to be excited and hence the shell vibrations. However, for the sake of simplicity the inclination has been set here to zero to only examine the lowest two circumferential modes. Thereby a perfect uniform alignment of the hammer and anvil on top of the monopile is assumed, resulting in perfect uniform force distribution over the pile in the circumferential axis. In reality, this is unlikely to happen due to imperfections of the anvil and pile. Both circumferential modes are illustrated in Figure 4.2

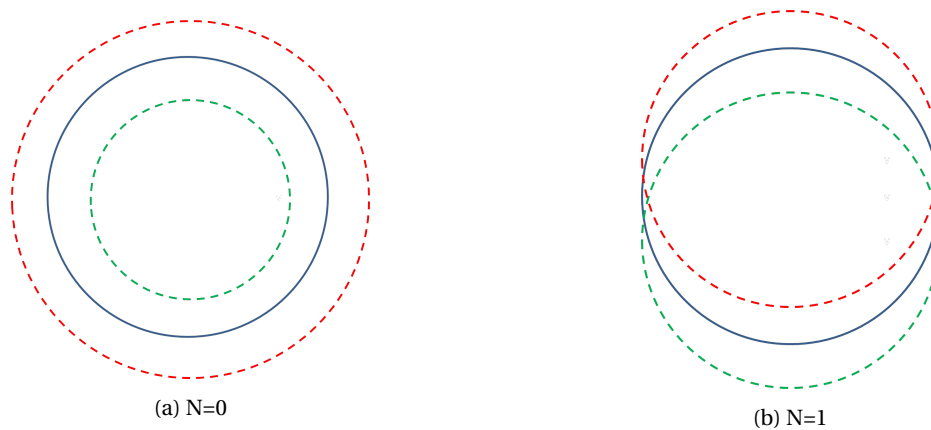


Figure 4.2: Circumferential modes of the shell. $N=0$ is the first circumferential mode. $N = 1$ is the second circumferential mode

At the pile head the total vertical load is a function of time and of the angular coordinate. However, since the purpose of the model is to calculate results also in frequency domain, a transformation of the force in the frequency domain is required.

4.2. Model Interface

The model is a rather quick and easy to configure model to predict the noise levels at different distances and heights in the fluid layer. In order to get to this outcome, a number of input parameters have to be inserted in the model interface. This section will give a short description of the model interface and parameter meanings. This will also give insight in some important settings that are of importance to insert correctly and need extra attention.

Basically, the model interface is build in a single file. This file is divided in six partitions all with a different main subject. In each partition itself, multiple characteristics that are related to the main subject of that partition can be inserted. The main subjects and related characteristics are summarized in Table 4.1 and illustrated in Figure 4.3.

Pile, Fluid and Soil

The first three partitions are reasonably straightforward. They account for the basic properties of that medium and need to be inserted once and further be left unnoticed as much as possible. In the case in which for different stages of installation the noise level have to be examined, the sea surface level relative to the pile coordinates has to be adjusted in the partition Fluid. Inserting a well thought maximum number of modes in partition Pile is favorable. Taking more modes than needed has no influence on the final results, however the computation time increases. As a result, a maximum number of modes of minimal two times the maximum sampling frequency is needed. For the resuming three partitions, some more explanation is required due to the large amount of possibilities as can be seen in Table 4.1.

Force

The partition Force is a very important partition since here the duration of the analysis is determined. This is

Table 4.1: Main subjects and related characteristics of the Spring Dashpot Model

Partition	Subject	Characteristics
(a)	Pile	Basic pile properties Spring stiffness at the edges Modal shapes Pile eigenvalues
(b)	Fluid	Basic fluid properties Number of fluid modes
(c)	Soil	Basic soil properties Seabed surface impedance
(d)	Force	Number of frequency steps Time step Amplification factor of input force Inclination of applied force
(e)	Analysis	General problem Domain Analysis type Presence of inner fluid Seabed-water interface Force type Shell edge boundary conditions Evanescent field
(f)	Grid	Grid data Points along the pile Points in water in distance and height

depended on the sampling time of the force input and the number of frequency steps inserted. These need to exceed the time the noise takes to reach the point of interest. Since the requirements of the BSH, as stated in section 2.3.3, is that at 750 m the SEL must be below 160 dB re $1 \mu Pa^2 s$ it is our interest to aim for that region in investigating the noise levels. Consequently with a speed of sound through water of 1490 m/s this takes approximately 0.5 seconds to reach 750 m.

However, acoustic dispersion is the phenomenon of a sound wave separating into its component frequencies as it passes through a material so that different frequency components travel at different speeds. As a result, the pressure wave package spreads out with the longer wavelengths moving faster and the shorter wavelengths lagging behind. Taking this phenomenon into account result in an even longer period of time which has to be accounted for by the model in order to capture all waves at 750 m. Therefore an minimum of 0.96 sec has been chosen in order to capture all waves. This means that with the current model a time step of 0.0004 sec a number of 1200 frequency is needed to reach $2 \cdot 1200 \cdot 0.0004 = 0.96$ sec analysis time. In coming up versions of the model, this feature will need to be updated to be able to work with longer time windows.

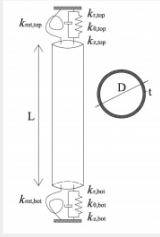
In order to insert the force, a DAT file must be generated and inserted in the folder Input. The time step in the file must match the selected time step in the interface and the selected hammer as will be discussed further below. One must also take into account that the DAT file must contain enough data to exceed the analysis time of the model. If not the case, the model will crash in an early stage.

Analysis

The partition Analysis is where the selection is made whether to analyze in frequency or time domain. In order to obtain time domain data, always first a frequency domain analysis has to be performed. This function is related to the function: General problem. When running the model in the frequency domain, one must do this ones with including the eigenproblem of the shell in order to calculated the modes of the shell. This can be combined with the forced response and is only applicable in the frequency domain. When willing to analyze thereafter the time domain response, one does not have to do the eigenproblem analysis again since this is only calculated in the frequency domain. Subsequently, when no adjustment are done to the partition

Basic pile properties

$E = 21000000 \text{ Nm}^{-2}$
 $\nu = 0.28$
 $\rho = 7850 \text{ kgm}^{-3}$
 $t = 0.08 \text{ m}$
 $D = 7.8 \text{ m}$
 $L = 80 \text{ m}$
 $\eta = 0.001$



Spring stiffness at the edges

$K_{r,top} = 55000000 \text{ Nm}^{-3}$
 $K_{\theta,top} = 55000000 \text{ Nm}^{-3}$
 $K_{z,top} = 55000000 \text{ Nm}^{-3}$
 $K_{r,bot} = 55000000 \text{ Nm}^{-3}$
 $K_{\theta,bot} = 55000000 \text{ Nm}^{-3}$
 $K_{z,bot} = 55000000 \text{ Nm}^{-3}$
 $K_{rot,bot} = 55000000 \text{ Nm}^{-3}$

Modal shapes

$n_{max} = 1$ $m_{max} = 420$

Pile eigenvalue problem (control parameters)

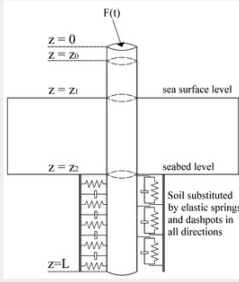
$N_{steps} = 3000000$ $Df_{step} = 0.01$
 $f_{(n=0)} = 1000$ $df_{(n=0)} = 0.1$
 $f_{(n=1)} = 500$ $df_{(n=1)} = 1.1$
 $f_{(n>1)} = 400$ $df_{(n>1)} = 2.1$

SilenceApp v.0.0.2

(a) Pile

Fluid properties

$\rho_{r,i} = 1025 \text{ kgm}^{-3}$
 $C_{r,i} = 1490 \text{ ms}^{-1}$
 $\eta_{r,i} = 0.15$
 $\rho_{r,e} = 1025 \text{ kgm}^{-3}$
 $C_{r,e} = 1490 \text{ ms}^{-1}$
 $\eta_{r,e} = 0$
 $Z_0 = 4.5 \text{ m}$
 $Z_1 = 4.5 \text{ m}$
 $Z_2 = 43.5 \text{ m}$



Number of fluid modes

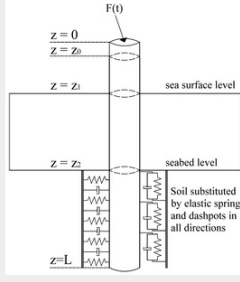
$N_{max,i} = 500$
 $N_{max,o} = 500$
 $N_{max,imp} = 400$

SilenceApp v.0.0.2

(b) Fluid

Soil properties

$E_s = 50000000 \text{ Nm}^{-2}$
 $\nu_s = 0.4$
 $\rho_s = 2000 \text{ kgm}^{-3}$
 $\xi_s = 0.01$
 $\xi_{rad} = 0.8$



Seabed surface

$Re(\zeta_s) = 1$
 $Im(\zeta_s) = 0.1$
 $P_{max} = 500$

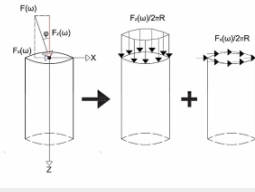
$k_r = 4.6428571 \text{ Nm}^{-3}$
 $k_z = 2.321428E \text{ Nm}^{-3}$
 $k_\theta = 2.321428E \text{ Nm}^{-3}$

SilenceApp v.0.0.2

(c) Soil

Force input data

Number of frequency steps = 1200
 $\Delta t = 0.00040$
 Number of time steps = 2400
 Amplification factor of the input force = 1
 Factor inverse transform = 2
 Inclination of the applied force = 0
 Multiplier of initial time step for output = 10



Number of time steps for output files = 2400
 Duration of analysis = 0.960000000

SilenceApp v.0.0.2

(d) Force

General problem = Eigenproblem and forced response

Frequency of the domain solution = Frequency domain analysis with actual force

Analysis type = Immersed response with modal cross coupling

Inner fluid presence = YES

Seabed-water interface = Rigid bottom

Shell edge boundary conditions = Clamped-free

Force type = IHC Force

Evanescent field = ON

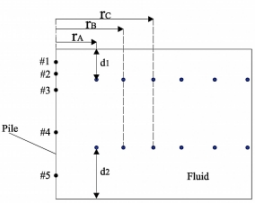
Extensive output = OFF

SilenceApp v.0.0.2

(e) Analysis

General grid of the output files (for animation)

Nr of points along z-coordinate (pile) = 2000
 Density of mesh along z-coordinate (pile) = 1
 Nr of points along theta-coordinate (pile) = 10
 Density of mesh along theta-coordinate (pile) = 1
 Nr of points along r-coordinate (fluid) = 20
 Density of mesh along r-coordinate (fluid) = 1
 Multiplier of radial coordinate for output = 50



Points at the pile (for graphs)

Point 1 = 0.1
 Point 2 = 0.3
 Point 3 = 0.5
 Point 4 = 0.7
 Point 5 = 0.9

Points at the water (for graphs)

$r_A = 0.1$ $r_D = 0.45$
 $r_B = 0.15$ $r_E = 0.65$
 $r_C = 0.25$ $r_F = 0.8$
 $d_1 = 20$ $d_2 = 2$

SilenceApp v.0.0.2

(f) Grid

Figure 4.3: Spring Dashpot Model Interface

Pile and Fluid, the eigenproblem analysis does not have to be executed again. This partition also enables to select whether to include inner fluid or not. Including the inner fluid will result in lower noise levels as a result

of the extra damping associated with the energy transferred into vibrations of the inner fluid.

For the seabed modeling there are three options, namely: rigid bottom, impedance bottom and a pressure release bottom. The rigid bottom assumes the velocity of the acoustic fluid normal to the seabed surface to be zero. The impedance bottom assumes the specific impedance of the seabed to equal that of the external fluid. At last, the pressure release bottom where the amplitude of the reflected wave is equal to the one of the incident wave.

In order to account for multiple hammer types and corresponding impact diagrams, the model delivers the option to switch between a small variety of different force types. Please mention that when selecting in the current model the IHC force, the input must be given in MN. But when selecting all other input forces the input must be given in Newtons. In coming up versions of the model, this will be updated to work uniformly.

Grid

Last partition is where the grid for the output files is defined and the mesh for the accuracy. Keeping the mesh as small as possible is favorable, but increases computational effort. The mesh in the vertical direction must fit about one-sixth of the smallest wavelength in order to get to an accurate outcome. For the selection of the point along the pile it is of importance to realize that the model has boundary conditions and therefore errors amplify close to these boundaries. As a result, selecting a point on a boundary is not advised.

For the selection of the points in the fluid layer, the picture in the interface (as also can be seen in Figure 4.3f) gives a clear description. The radial distance r can be selected to equation 4.3 and the height by inserting the distance in meters for d_1 from the seawater surface downwards and for d_2 from the seafloor upwards.

$$r = R_{shell} + (\alpha \cdot r_{max} - 1) \beta \quad (4.3)$$

In which α is the percentage of the the maximum radius and β the multiplier of radial coordinate. As example from the input parameters given in Figure 4.3f, where 20 point are selected in the radial direction. Combined with the multiplier factor β of 50, this corresponds for point D in a radial distance of 403.9 m from the vertical axis of the pile. With a radius of 3.9, this means 400 m from the outer shell position.

When all parameters inserted correctly the last partition is the Fire partition in which the final file automatically is generated, which serves as input for the executable file of the model.

4.3. Validation

The outcome of the model is validated with measured data. However, the nation of interest states is by law very strict in providing underwater raw sound data due to the possibility of detecting submarines in the area. Consequently, the only available data is from the Sound Level reports. Here the sound pressure levels and energy spectral density at three different locations is measured, two at 750 m and one at 1500 m. From this report, the energy spectral density as shown in figure 4.4a and the noise levels from figure 4.4b, both at 750 m, are most important. This is due to the fact that both are plotted against time and therefore can be related back to the three different stages as stated in table 3.4. Since the data has been extracted from only these figures and no raw data sets were delivered, error bars are included in the results to account for erroneous readings.

By validating the model on three different stages, variation in impact diagrams must be taken into account since at each of these three stages the soil penetration depth differs. From GRLWEAP, three different impact diagrams have been extracted at these three stages as also discussed in section 3.1.1. The results are shown in Figure 4.5a that, even tough the difference in soil resistance, clearly indicates nearly any difference in the impact diagram between the different stages.

Thereafter these three impact diagrams have been inserted in the Spring Dashpot model to observe the response in the frequency domain and time domain. In order to obtain a close fit with the measured data and computed data, other settings in the model are of importance to pay attention to as well.

One of these is the influence of the amount of energy which re-radiates from the soil layer into the fluid layer. This partly depends on the vibrations that travel through the soil as shear waves. In the case where these vibrations are not taken into account, like in the Spring Dashpot model, other methods should be adopted to

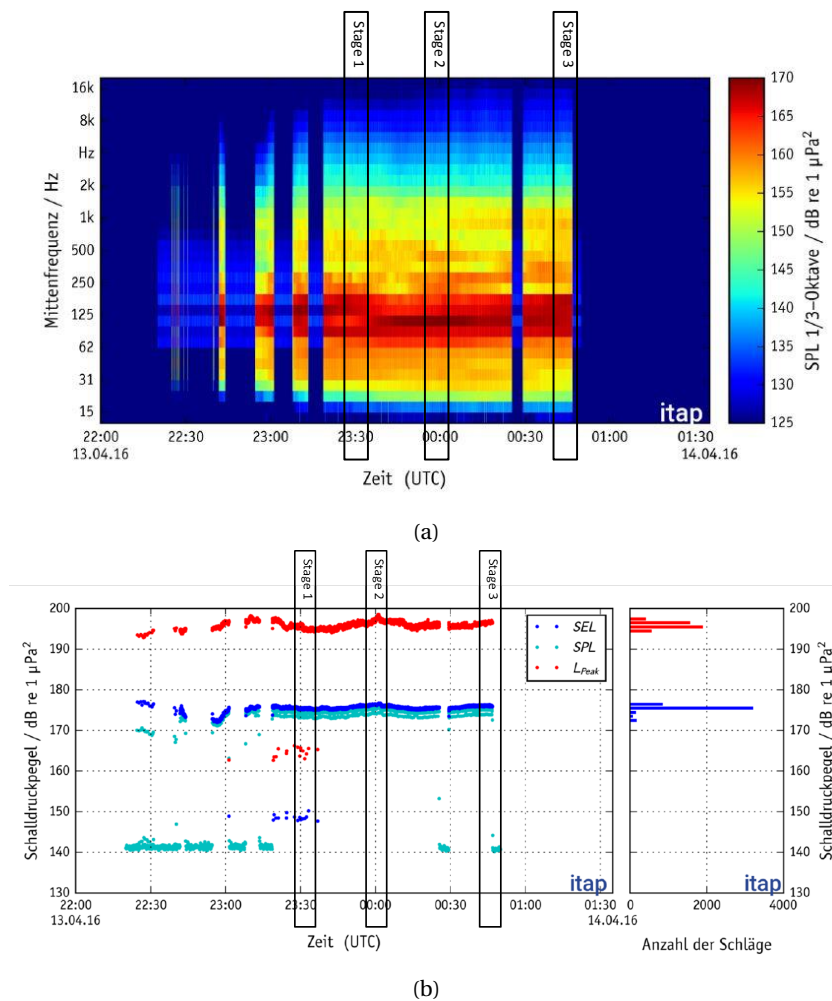


Figure 4.4: Available sound data at 750 m from the pile and 2 m above seabed (a) Energy spectral density and (b) Noise levels illustrated in SEL, SPL and L_{Peak} .

include the amount of energy that travels back from the soil. Meantime, this effect is simulated by adopting a percentage which represents the amount of energy that travels from soil to up to the fluid layer. This value is based on empirical research and is set to $\xi = 0.2$. This means that one fifth of all the energy reflecting at the soil water interface, re-radiates back into the fluid layer. The rest is absorbed into the soil layer and does not influence the final noise level in the fluid layer. However, this has only been analyzed for relatively small piles. Since here large size monopiles are considered, the low frequency propagating waves become more dominant. These low frequency wave are much less affected by the soil due to their long wavelength, and as a result less damping occurs. Hence more energy travels from the soil to the fluid layer and therefore the soil damping amplification factor must be increased. For this thesis a factor of $\xi = 0.8$ is used. In cases in which this factor is unknown a value of about $\xi = 0.5$ is advisable.

Secondly the influence of the inner fluid is examined. During pile driving the inner side of the pile is usually filled with fluid and soils. This has influence on the amount of energy which radiates into the exterior fluid layer since the inner fluid partly absorbs this energy already. Therefore the noise levels without inner fluid are expected to be higher than when including the inner fluid. Figure 4.6 shows the difference between including and excluding the inner fluid compared with the measured data. The differences are minor, but do show relative variations. Sound pressure levels decrease below the ring frequency with inner included. Above the ring frequency of 220 Hz, these differences becomes less. At the ring frequency itself, energy is lost due to the vibration of the pile. When excluding the inner fluid, the loss is less than when including the inner fluid. For further noise predictions with the Spring Dashpot model, the inner fluid is set to be included.

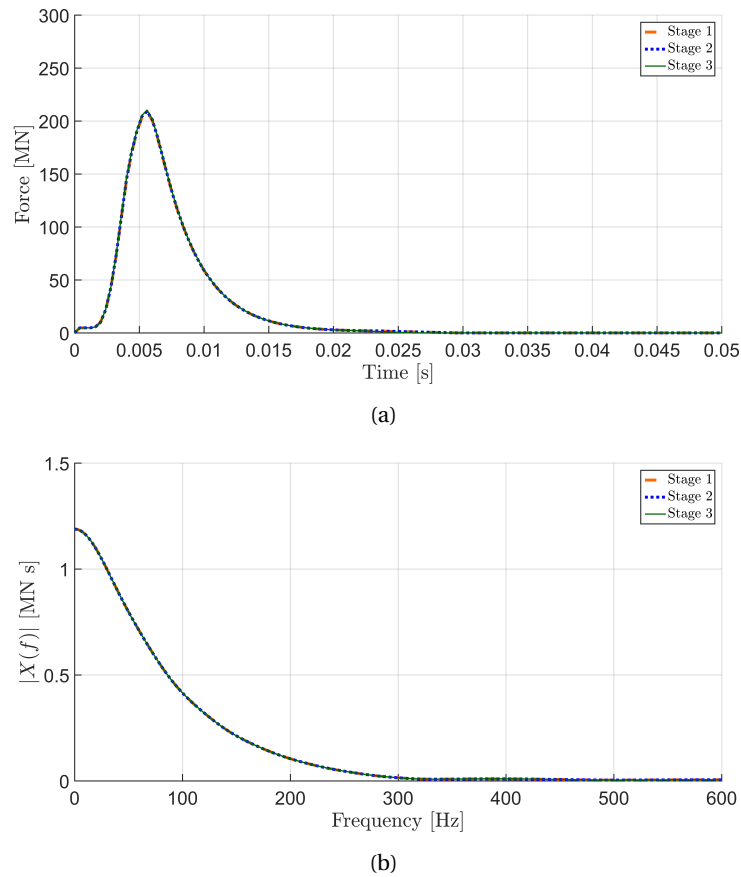


Figure 4.5: Input force of IHC S-4000 at stage 1, stage 2 and stage 3 in (a) time domain and (b) absolute excitation spectrum

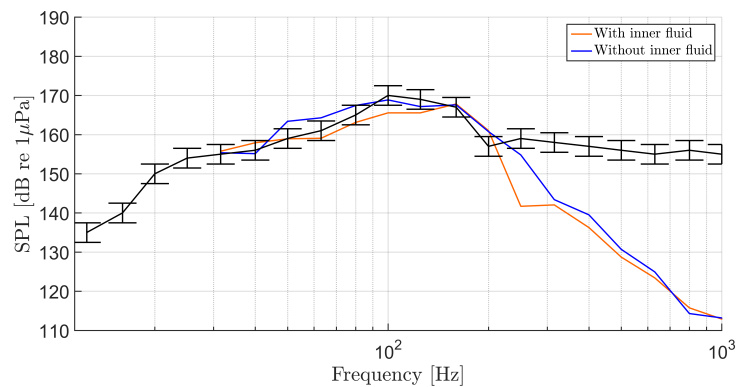


Figure 4.6: Comparison within frequency response spectrum at 750 m from piling source and 2 m above seabed with and without inner fluid.

4.3.1. Response during pile driving at different stages

Now the settings are known, the model can be used for noise predictions in order to validate the model for the three different stages in the frequency domain. Figure 4.7 shows the results after applying the different impact diagrams for different stages. The results are at a distance of 750 m from the piling source and 2 m above seabed in frequency domain. From the figures it can be seen that for the lower frequencies $f < 90$ Hz the model predicts a lower value than the real measurements. This is due to the fact that this model has no soil layer, only a spring dashpot configuration. Consequently, there is no influence of the soil region, a region where mainly low frequencies waves propagate. On the other hand, the model predicts a higher noise level between 90 Hz $< f < 200$ Hz. This can be related to the same explanation as described before. Due to the

fact that there is no soil, there is also no damping and frequencies can travel freely with only loose of energy due to the linear decrease. Just above 200 Hz a rapid drop in sound pressure level is visible in both the measured and modeled data. This is caused by the ring frequency of the pile at $f_r \approx 220$ Hz, which is obtained by equation 4.4. Around the ring frequency the majority of the energy is absorbed by the shell and almost no energy is irradiated into the fluid layer. Above these frequencies the difference between model and measurements increases, caused by the fact that the measurements still contain significant background noise. The background noise is mainly high frequency noise caused by for example vessel propulsion systems which is not considered in the model in the model predictions.

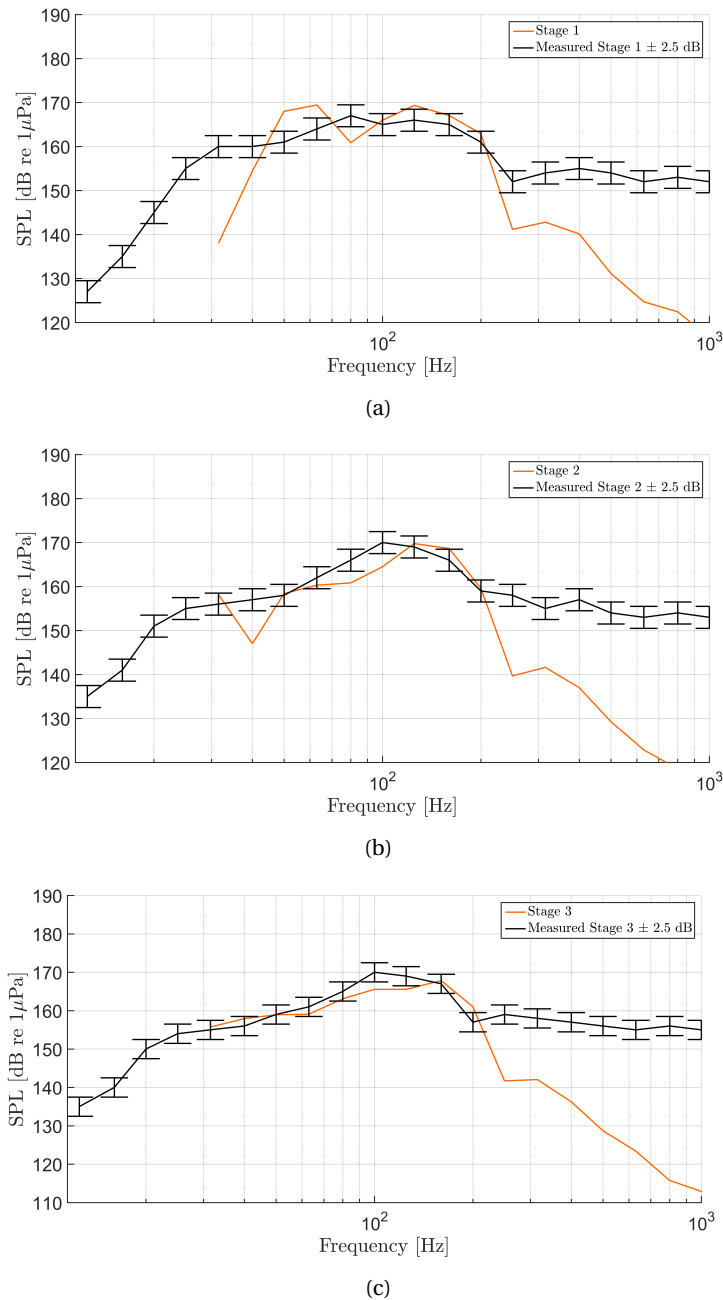


Figure 4.7: Comparison between measured data and modeled data in frequency domain for (a) Stage 1, (b) Stage 2 and (c) Stage 3 at 750 m from the pile and 2 m above seabed

$$f_r = \frac{1}{(2\pi R)} \sqrt{E/\rho(1-\nu^2)} \approx 220 \text{ Hz} \quad (4.4)$$

Having analyzed the results in the frequency domain, the focus is now placed on the analysis of the time domain. Figure 4.4b illustrates the measured data at 750 m and 2 m above seabed that contains the SEL, SPL and L_{peak} . As can be seen these are more or less the same during the whole installation, only during stage 2 they seem to be a bit higher than the rest which can indicate a change in soil structure.

The pressure field in the time domain is obtained by the inverse Fourier transform of the complex amplitudes obtained in the frequency domain. The evolution of the generated pressure wave with time for three radial distances from the surface of the pile and at two depth positions is shown in Figure 4.12. The top position is positioned at the top of the lower one-third of the water column whereas the bottom one at 2 m above the seabed. In Figure 4.8a, the reduction of the peak pressure for an increasing radial distance is clearly visible. A decrease of approximately 40% of the peak pressure value is observed between 10 m and 50 m distance. For the position closer to the seabed, as illustrated in figure 4.8b, the reduction between the same radial distances is 25%. This means a 60% increase of damping at the upper position compared to the lower position.

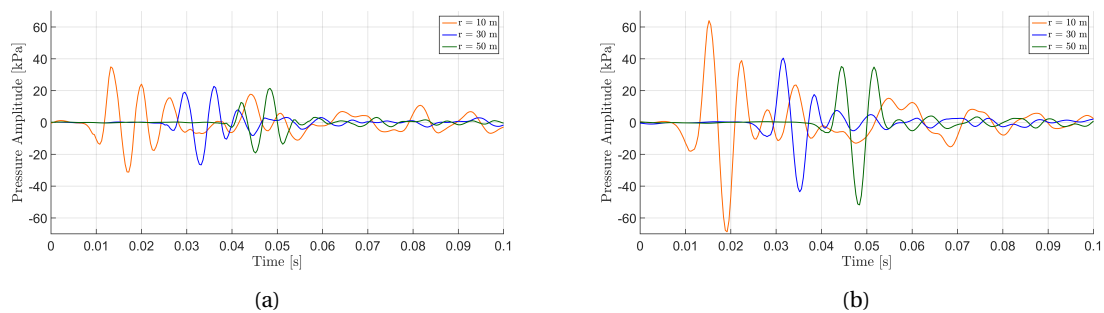


Figure 4.8: Pressure wave propagation with time of original impact diagram for three radial distances and (a) 12 m above seabed and (b) 2 m above seabed

Further from the pile surface, till 750 m, the reduction of the pressure wave between 50 m and 750 m is around 90%. This means a reduction of around 19 dB re $1 \mu Pa$. It can further be noticed that mainly high frequency compressional waves are propagating, and less dissipation of low frequency waves is present.

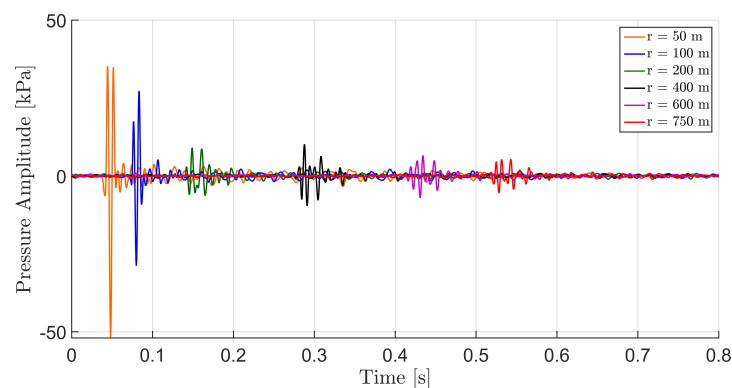


Figure 4.9: Pressure wave propagation with time of original impact diagram at 2 m above seabed

From the model predictions at 750 m and 2 m above seafloor the following results as shown in Table 4.2 were obtained for the SEL and L_{peak} . For stage 1 the model predictions are slightly overestimated, where for stage 2 and 3 the predictions are slightly underestimated. This is related to the fact that the Spring Dashpot model does not take account of sliding of the pile along the soil. It basically only consists of an elastic deformation part for the soil resistance. Meaning that with increasing energy in the pile and thus vertical displacement

of the pile material, the resistance force keeps increasing till the pile material vertical displacement starts decreasing. This high resistance force results in more energy propagating into the fluid and/or soil layer as noise, instead of energy for sliding.

In reality, the elastic resistance of the soil stops when reaching the final capacity of the soil and results thereafter in sliding of the pile. This results in a lower resistance force and thus less energy needed to drive the pile further. During stage 1, in reality significant displacement of the pile relatively to the soil takes place, this effect causes an overestimation of the noise due to the larger amount of energy which is considered as source of noise. Moving down to stage 2 and 3, where less penetration takes place in reality due to the increase of soil resistance, this effect is reduced. This is caused by means of less energy radiating into the soil for driving, and more energy radiating as noise and explains the underestimation of the model. Hence, linear models for noise prediction which essentially neglect the process of pile penetration per impact are expected to provide reliable predictions of the noise levels only when the penetration per blow is taken into account.

Table 4.2: Results of comparison from model predictions and measurements for the SEL_{05} and L_{peak} at 750 m from the pile and 2 m above seabed.

Stage	Depth	Category	Distance	Model	Measured	$\Delta SEL_{05} / \Delta L_{peak}$
	m		m	dB re 1 $\mu Pa^2 s$	dB re 1 $\mu Pa^2 s$	-
1	16.5	SEL_{05}	750	176.4	176	+0.4
		L_{peak}	750	195.6	196	-0.4
2	26.5	SEL_{05}	750	176.2	177	-0.8
		L_{peak}	750	194.9	197	-2.1
3	36.5	SEL_{05}	750	175.2	177	-1.8
		L_{peak}	750	194.8	196	-1.2

4.4. Parametric Study

In the previous sections, the response of the system has been examined after exciting with an impact hammer. As described in section 2.2.1 this results in a short pulse that induces high velocities in the pile. By enlarging the duration of the impact force, the downward propagating compressional waves will block the upward moving tension waves and therefore reduce radial displacement of the pile and hence radial velocities. To examine the effect of the enlargement of the impact force on the underwater noise, the impact diagram of the BLUE Piling hammer has been inserted to the Spring Dashpot model and discussed in this section.

However, the model is only capable of predicting for limited amount of time duration due to the application of the fast Fourier transformation. Therefore the maximum duration is connected to the amount of inserted frequency steps. Since the full impact diagram takes 2.2 sec it is impossible to insert the full impact diagram into the model. Therefore it has been chosen to only implement the main pulse between 1 and 1.5 sec as shown in Figure 4.10a. This has the highest peak force and will therefore have the most influence on the underwater noise. The option of inserting the other two pulses separately in the model and adding the final sound levels together is not desirable. Due to the large duration of time between the pulses (about 0.5 sec) the noise levels can not be considered cumulative.

4.4.1. Response in frequency domain

Applying the impact diagram from figure 4.10a to the Spring Dashpot model with the same parameters settings for the model as used for the impact hammer, results in a response in the frequency domain compared to the frequency response with an impact hammer as shown in figure 4.11.

The figure shows a clear difference in magnitude of the absolute frequency response spectrum at 750 m caused by the different frequencies which are excited by the hammers. For the IHC S-4000, the frequencies that are excited reach up to around 300 Hz. For the BLUE 25M this is much lower, namely about 50 Hz as shown in Figure 4.10b. This clearly indicates the effect of changing the duration of the impact diagram on the absolute excitation spectrum. Since the Spring Dashpot model does not model soil explicitly, the secondary noise path where waves travels from the soil up to the fluid layer, is hardly present. Consequently, the

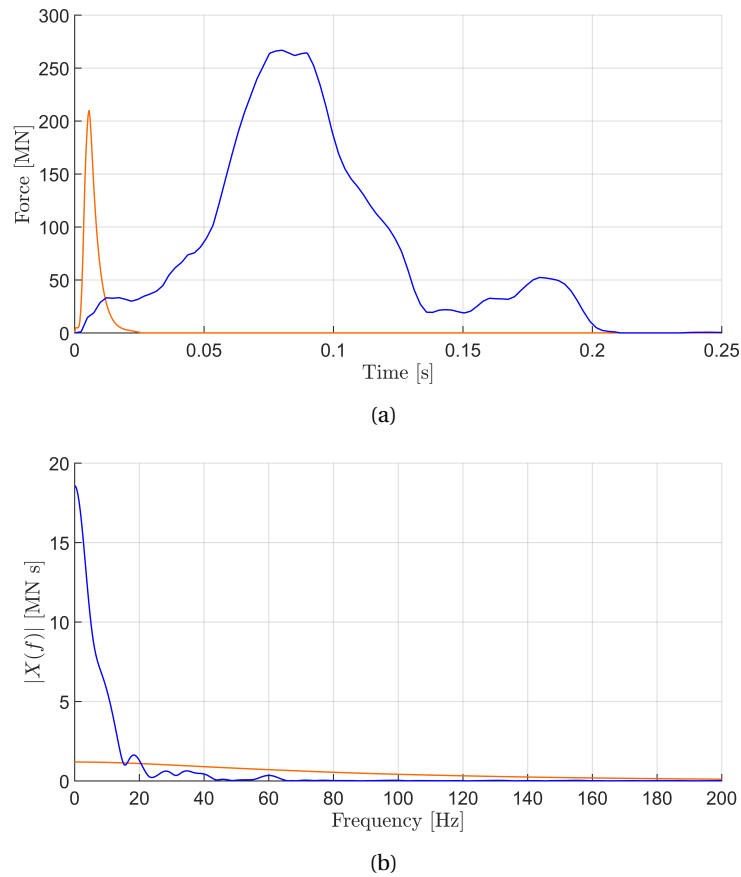


Figure 4.10: Main input force of BLUE 25M and compared to IHC S-4000 in (a) time domain and (b) absolute excitation spectrum

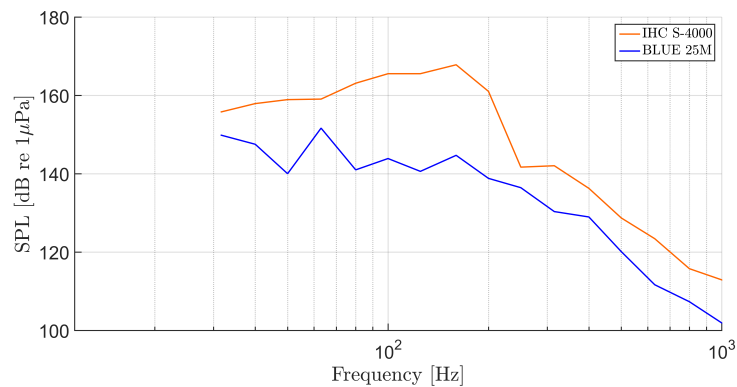


Figure 4.11: Frequency response spectrum at 750 m from piling source and 2 m above seabed after exciting with BLUE 25M and IHC S-4000.

underwater noise predictions of such a large duration of impact with the corresponding low frequencies are probably underestimated in this model.

4.4.2. Response in time domain

In the time domain, enlarging the pulse of the impact diagram such as done for the BLUE 25M with 90% compared to the one from IHC S-4000, will have significant results on the noise level. That is caused by the way the BLUE 25M creates its traveling wave in the pile. By applying a force over such a long duration of time, there is no modus for the reflected wave to travel back up the pile as it is absorbed by the downward traveling compression wave. This reduces the vibrations in the pile since now only an compression wave is traveling

downwards and no tension wave upwards any more as is the case with conventional impact hammers. Reducing the vibrations in the pile means reducing the absolute pressure wave in the fluid layer as shown in Figure 4.12 with 91%. With the definition of the SEL as stated in equation 2.10, the SEL is lowered to 158 dB at 750 m and 2 m above seabed. This is a reduction of 17.2 dB as can be seen in Figure 4.13.

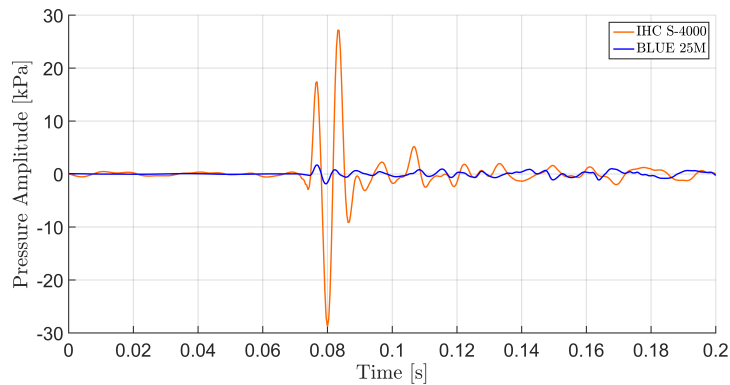


Figure 4.12: Pressure waves propagation with time for the IHC S-4000 and BLUE 25M at 2 m above seabed and 100 m from pile.

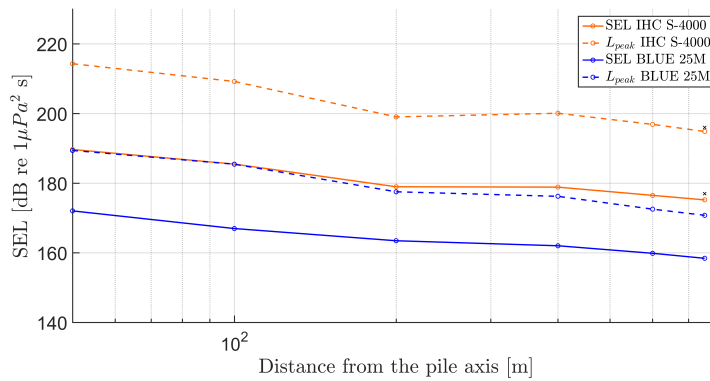


Figure 4.13: SEL and L_{peak} values for the IHC S-4000 and BLUE 25M at 2 m above seabed

4.5. Conclusions

In this chapter, a rather quick and easy to configure model is examined for the prediction of underwater noise levels during piling of large sized monopiles. The model incorporates all major parts of the system: the hammer is substituted as an external force, the pile is described as a thin cylindrical shell, the water is modeled as a compressible fluid medium and the water-saturated seabed is represented by uncoupled springs and dashpots in all directions.

A validation was performed in both frequency and time domains to quantify the accuracy during different stages of installation. Measured data from monopile installation without any noise mitigation system was compared with model predictions. Thereby also the influence of the inner fluid and the soil damping factor have been investigated in order to obtain the best fit to the measured data. This comparison revealed the influence of different stages during installation on the noise predictions. Low amount of penetration of the pile into the soil results in an overestimation of the model compared to the measured data. Further penetration into the soil results in an underestimation of the noise levels. However, the results are within an acceptable accuracy of ± 2 dB.

Finally, a parametric study was performed in order to reveal the influence of another hammer on the response of the system. With an increased duration of the impact diagram of about 90%, a significant reduction in

pressure waves and finally in the SEL was obtained. However, enlargement of the time duration results in an increase of energy carried by low frequency waves. These low frequency waves are less attenuated in the soil and therefore contribute to energy propagating through the secondary noise path. This path is not accounted in the present model. Consequently, this indicates the need for a more realistic soil description to accurately predict noise levels. Such a soil description formed the basis of the second acoustic model developed by Tsouvalas and Metrikine [2014] as discussed in chapter 5.

5

Elastic Medium Model

The here presented chapter discusses the Elastic Medium model. This model is developed to overcome the uncertainty involved in selecting springs and dashpots coefficients since these can have a large influence on the final outcome. The model differs by means of a three-dimensional description of the soil. Subsequently, the need for realistic estimation of the spring and dashpot coefficients is avoided since simple basic soil properties are only required for a complete soil description.

After the Elastic Medium model is discussed in section 5.1, a brief description of the interface of the model is given to get a first idea of the parameters used as input and available different settings (section 5.2). In order to make sure that the model predictions are in line with the reality, a validation has been conducted in section 5.3. Also the influence on the frequency spectrum for the exterior fluid layer and pressure levels are discussed. In section 5.4, the energy input in the system and the percentage output through the soil and fluid layer is analyzed that reveals a remarkable phenomenon.

5.1. A 3-D vibroacoustic model

The model described in this section extends the model presented in chapter 4, in which the soil was modelled by distributed springs and dashpots. These were attached to the shell's outer surface to represent soil elasticity and soil damping. In this model the soil is modeled as a three-dimensional elastic continuum that is terminated at a convenient depth with a rigid boundary. The total system including pile, fluid and elastic medium to represent soil layer is shown in Figure 5.1 for one soil layer.

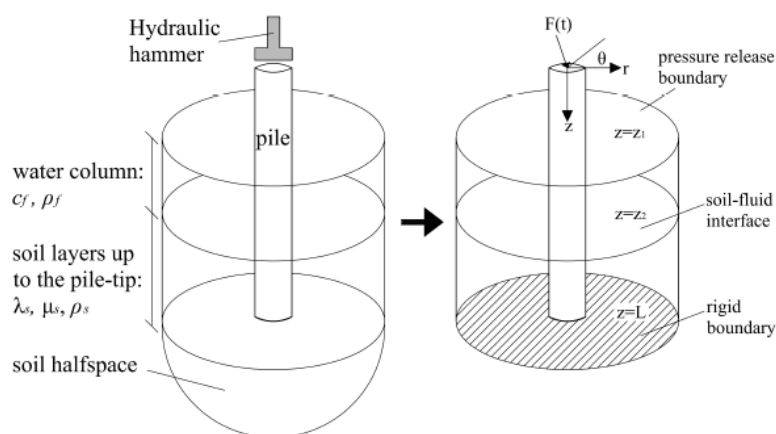


Figure 5.1: Geometry of the 3-D pile-water-soil model [Tsouvalas and Metrikine; 2014]

The soil covers the depths in the region $z_2 \leq z \leq L$ and $r > R$ and the interface at $z = L$ is the rigid boundary. In order to better represent the reality, the soil is build up from a number of different horizontal layers. These

layers can differ in material dependent quantities. For further explanation of the elastic medium model it is referred to Tsouvalas and Metrikine [2014].

5.2. Model Interface

The present model is a more advanced version of the Spring Dashpot model, mainly with regard to the soil description due to the different model structure. Inserting all parameters here is for this reason more time consuming, but otherwise similar to the Spring Dashpot model. Here a single excel file is provided to account as input file that is divided in eight partitions all with different main subjects. In each partition itself, multiple characteristics, which are related to the main subject of that partition, can be inserted. The main subjects and related characteristics are summarized in Table 5.1 and illustrated in Figure 5.2.

Table 5.1: Main subjects and related characteristics of the Elastic Medium Model

Partition	Subject	Characteristics
(a)	Pile	Basic pile properties Pile geometry
(b)	Fluid & Soil	Basic fluid properties Basic soil properties Soil Damping
(c)	Analysis	General problem Shell Theory Soil stratification Domain Analysis type Force type Shell edge boundary conditions
(d)	Shell edge	Spring stiffness at the edges
(e)	Main Control	Number of soil modes Number of fluid modes Scholte mode Number of Shell modes Number of circumferential modes Pile eigenvalues
(f)	Force	Time step Amplification factor of input force Number of approximated hammer strikes
(g)	Grid	Grid data
(h)	Points	Points along the pile Points in water in distance and height Points in soil in distance and height

Pile

The first partition is reasonably straightforward. It accounts for the basic properties of the pile that needs to be inserted once and further be left unnoticed as much as possible. In this partition, the pile geometry is inserted that also accounts for the positions of the different medium layers. The model has the ability to include two soil layers with different parameters. In this partition, the beginning of the second soil layer is inserted. Since the wave propagation is modeled in all directions, extra soil is added to account for wave propagation below the tip of the pile. In the case where for different stages of installation the noise level has to be examined, the positioning of where the fluid layer and soil layers are in direct contact to the pile has to be adjusted.

Fluid & Soil

This partition accounts for the fluid and soil properties. The fluid properties are reasonably straightforward, but the soil properties need more attention. For the soil the modulus of elasticity, Poisson ratio, density,

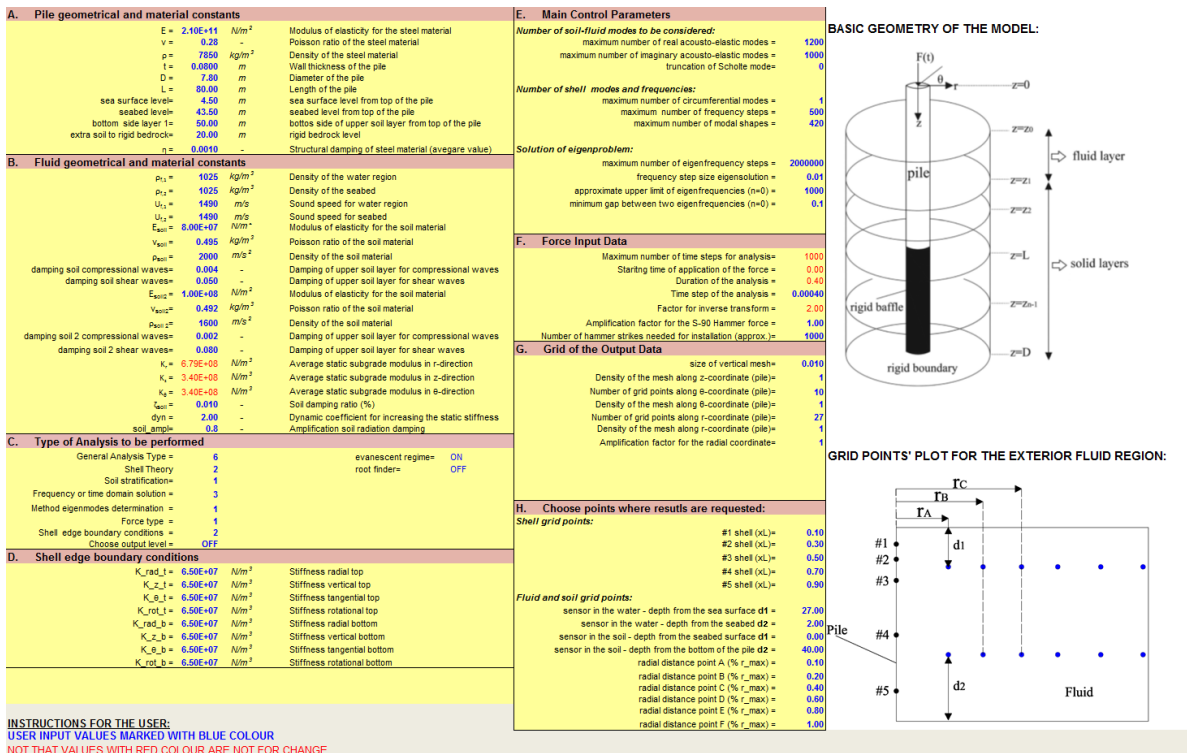


Figure 5.2: Elastic Medium Model Interface

damping of compressional waves and damping of shear waves must be inserted. The first three can be obtained from basic soil data, meanwhile the latter two need more work. Modulus of elasticity, Poisson ratio and density characterize the velocity of the compressional c_p and shear c_s wave. With these quantities, the attenuation of the compressional and shear waves that depends on the grain size are derived as described in Buckingham [2005] by means of the grain size distribution.

Analysis

The partition Analysis is where the selection is made what is desired to analyze. The model has seven functions to choose from, but all are related to each other.

1. Eigenproblem of the shell
2. Eigenproblem of the soil-fluid region
3. Forced response of the coupled system
4. Eigenproblem of the soil-fluid region + Forced response of the coupled system
5. Forced response of the in-vacuo shell
6. Eigenproblem of the shell + Eigenproblem of the soil-fluid region + Forced response of the coupled system
7. Calculation of plots and results

This means that when changing some parameters, per definition not the entire analysis has to be performed again. If one changes the force and/or the frequency steps, only need to re-run function 3. Changing the position of the output points only requires a re-run of function 7. If the properties of the soil or fluid layers are changed, then re-run function 4. Adjusting the pile properties but not the soil or fluid layer properties, means function 1+3. Finally, when changing everything function 6 must be used which includes all previous functions.

In order to account for multiple different hammer types and shapes, the model delivers the option to switch between a small variety of different force types. Keep in mind that when selecting the actual force function,

the input must be given in MN, but when selecting all other input forces the input must be given in Newtons. In coming up versions of the model, this will be updated to work uniformly.

Main control

In this partition the most important function is the amount of modal shapes and number of frequency steps. The modal shape determines the amount of modes taken into account. Choosing this value too "low" results in incomplete analysis but choosing this value too "high", results in a very time consuming analysis. Accordingly it is of importance to choose the maximum number of frequency steps (with a maximum of 690 in the current version of the model) in correspondence with the associated modes. By taking the maximum mode which corresponds with twice the maximum number of frequency steps, this problem is covered.

Force

From the selection in previous partition the maximum number of frequency steps corresponds to the total analysis duration. This is due to the application of the Discrete Fourier Transform (DFT). As a results, a fixed frequency-time relation takes place. This feature will be updated in the upcoming version of the model.

In order to insert the force, a DAT file must be generated and inserted in the folder Input. The time step in the file must match the selected time step in the interface and the selected hammer as will be discussed further below. One must also take into account that the DAT file must contain enough data to exceed the analysis time of the model. If not the case, the model will crash in an early stage.

Grid & Points

Last partition is where the grid for the output files is defined and the mesh for the accuracy. Keeping the mesh as a fraction of the smallest wavelength is favorable, but increases computational effort. For the selection of the point along the pile it is of importance to realize that the model has boundary conditions and consequently errors at that location. Selecting a point on the boundary is as a result of that not advised.

For the selection of the points in the fluid layer, the picture of the interface at the right bottom gives a clear description. For both the fluid as for the soil layer, six points can be selected in the radial direction r according to equation (5.1) and the height by inserting the distance in meters for d_1 from the seawater or seabed surface downwards and for d_2 from the seafloor or depth from bottom op pile upwards.

$$r = R_{shell} + (\alpha \cdot r_{max} - 1) \beta \quad (5.1)$$

When all is inserted correctly the last step is to press the create input file button that creates the final file automatically that serves as input for the executable file of the model.

5.3. Validation

This section describes the procedure of validating the Elastic medium model. Ideally this is done by the same procedure as the validation of the Spring Dashpot model in section 4.3. Due to the use of the DFT

However, the current Elastic medium model has a limitation in analysis time due to the application of the DFT. As a result the maximum analysis time for this particular case is 0.6 seconds. From Table 3.7 it is clear that the limiting velocity is that of the shear waves of 269 m/s . Hence with an analysis time of 0.6 seconds this results in a maximum distance to be analyzed of 160 m. Taking further account of damping results finally in a maximum distance of around 100 m. This is lot less than the with the Spring Dashpot model where the 750 m boundary got to be reached due to the neglect of shear waves in the soil.

No measurements are performed within the 750 m region, which means no data is available to validate the Elastic medium model within 100 m. As a result, the validation has been performed in a more pragmatic method. By means of the logarithmic trend of the noise levels obtained withing 100 m, and extrapolating to 750 m. The SEL and L_{peak} can finally be obtained and compared with measured data. To compare the response of the Elastic medium model within the 100 m range, the results are compared with the Spring Dashpot model. Therefore the same parameters for the Elastic Medium model are inserted in the Spring Dashpot model.

The system is excited with the impact diagram from Figure 5.3a with corresponding frequency spectrum from Figure 5.3b. This is identical to the one obtained from GRLWEAP in section 3.1.1 and used for validation of

the Spring Dashpot model.

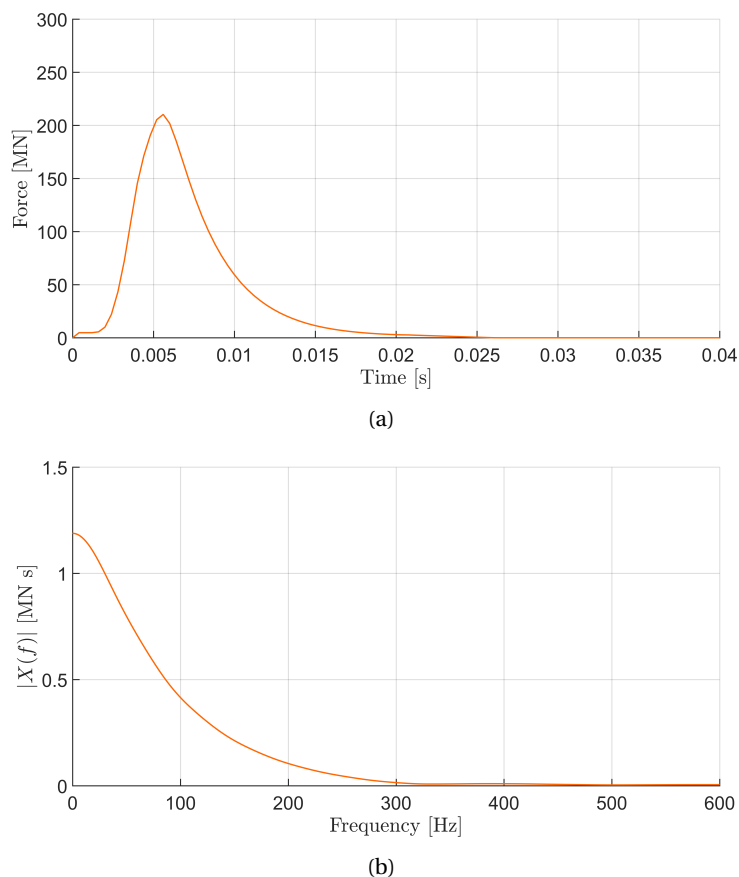


Figure 5.3: Input force of the IHC S-4000 at stage 3 in (a) time domain and (b) absolute excitation spectrum

The specific input parameters, wave speeds and attenuation factors are presented in Table 3.6 and Table 3.7. Even though the model is capable of inserting two soil layers, for simplicity only one layer has been adopted in this study.

5.3.1. Response during pile driving at different stages in frequency domain

The obtained response in the frequency domain for both models is here discussed. The frequency spectrum from Figure 5.4 is obtained at 100 m from the piling source and 2 m above seabed. Important to notice is the influence of the cut-off frequency on the result. The cut-off frequency is related to shallow-water wave propagation. Deep-water wave propagation is a function of the upward refracting sound-speed profile that permits long range propagation without significant bottom interaction. Meanwhile for shallow-water wave propagation, which is for water depth down to 200 m, the sound-speed profile is downward refracting or nearly constant over depth, meaning that long range propagation takes place exclusively via bottom interacting. As a consequence, the important reflection paths either become the soil reflected path or the water surface-soil reflected path. Taking accordingly the correct attenuation factor, presented in Table 3.7, of the soil into account is of importance. The cut-off frequency is a common feature in acoustic to mark the frequency below no modes can propagate in the fluid layer and consequently radiate into the soil layer. Hence, there is a critical frequency below which the shallow-water channel ceases to act as a waveguide, causing energy radiated by the source to propagate directly into the seabed. The cut-off frequency is calculated by: [Jensen et al.; 2011]

$$f_0 = \frac{c_w}{4D\sqrt{1 - \left(\frac{c_w}{c_b}\right)^2}} \quad (5.2)$$

In which c_w is the speed of sound in the fluid layer, c_b speed of sound in the seabed and D the water depth. For the here adopted parameters this results in a cut-off frequency of 26 Hz. Meaning all energy in the frequencies below 26 Hz will propagate directly into the seabed and have no effect on the acoustic pressure waves in the fluid. Having introduced the cut-off frequency influenced by the speed of sound through the seabed, the case where no seabed is taken into account but only a rigid bottom can be examined, namely the Spring Dashpot model. Here c_b goes to infinity meaning a cut-off frequency of 9.6 Hz.

Second reason of attenuation in the fluid layer in shallow water is the coupling of acoustic energy into shear waves in the soil water interface. Soil conditions play an important role in here since the stiffer the soil, the higher the shear wave velocity and thus more influence of the shear waves. Where for a more sandy soil, and thus less stiffness, negligible shear waves effects are encountered. This mainly affects the low frequency waves.

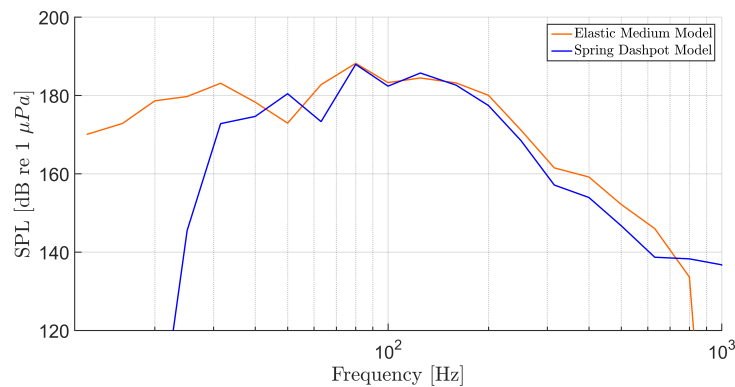


Figure 5.4: Frequency spectrum in the fluid at 100 m and 2 m above seabed for Elastic Medium Model and Spring Dashpot Model

From the figure, the influence of the soil immediately becomes clear compared to the Spring Dashpot model. The response above 100 Hz is similar for the Spring Dashpot model and the Elastic medium model. The main difference is in the lower frequency area, $f < 100$ Hz, due to the better soil interaction of the present model. Consequently a relative high sound pressure level in the lower frequency area is obtained. This is caused by the influence of the shear and Scholte waves as these travel with a lower wave speed. Thereby it must be mentioned that due to the limited computational analysis time and the correlated analyzed distance from the source, the wave numbers are an important topic. The wavelength of a 10 Hz wave in fluid is around 150 m, which is more than the analyzed distance of 100 m. As a consequence, their influence is overestimated in the present approach.

In order to analyze the influence of the low frequency waves at the region, a comparison of the frequency spectrum with increasing distance from the seabed is performed and presented in Figure 5.5. The difference in pressure levels between the two distances indicates the influence of the secondary noise path and the presence of Scholte waves near the soil water interface. Also due to the large size of the monopile, and corresponding relative low ring frequency of 220 Hz, the low frequency waves become more dominant. As a result the frequency spectrum might look wrong compared to previous research. These studies have mainly focused on relative small diameter piles, and for this reason result in a relative high ring frequency. The influence of the low propagating frequencies with small diameters piles is less, which consequently shows nearly any low frequency waves in the frequency spectrum. Analyzing the influence of the low frequency waves is therefore of importance.

5.3.2. Response during pile driving at different stages in time domain

Figure 5.6 shows the time signal of the computed data at 50 m from the pile and 2 m and 12 m above seabed after one impact.

This shows the difference between the main pressure wave around 50 ms with a velocity equal to the wave speed in water, and the minor second pressure wave around 25 ms. Moving up in the fluid layer, the second pressure wave is lost indicating influenced by soil deformation. The influence of the first pressure wave is

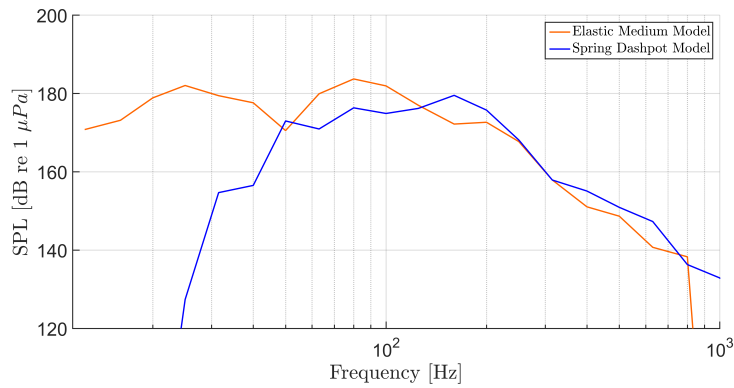


Figure 5.5: Frequency spectrum in the fluid at 100 m and 12 m above seabed for Elastic Medium Model and Spring Dashpot Model

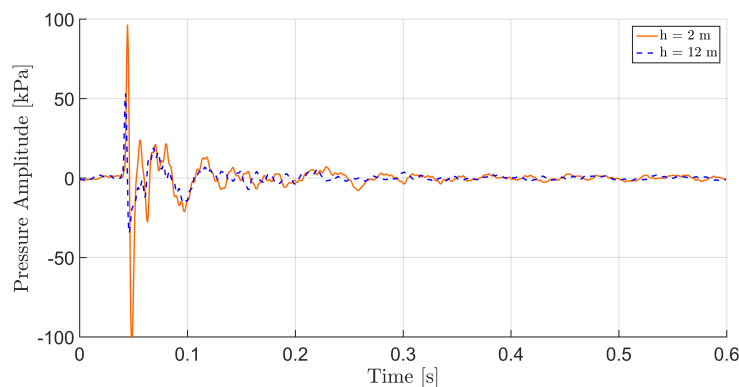


Figure 5.6: Pressure wave propagation in time in fluid layer at two heights from the seabed and 50 m from pile

mainly related to the radial component of the particle velocity instead of the vertical velocity as indicated by Figure 5.7. This means the first pressure wave consist of only compressional waves and is accordingly caused by the primary noise path. The compressional pressure wave near the seabed is 1.8 ms after the compressional pressure wave at 12 m above seabed. This indicates an inclination angle of $\tan^{-1}(2.7/10) \approx 15.1^\circ$ compared to the vertical axis of the pile. Figure 5.8 illustrates the sound waves inclinations angles to the vertical pile axis as here obtained and in the following next section. For the second pressure wave there is a combination of radial and vertical velocities in the fluid layer, meaning that this pulse is influenced by a Scholte wave in the soil. The low frequency energy, indicated in the fluid layer response, is caused by the Scholte waves. Since the energy carried by these waves is confined in a localized zone close to the interface, they experience less attenuation in comparison to other propagating waves and consequently retain their energy.

Figure 5.9 shows the vertical polarization of the soil response that indicates the presence of dominant shear waves. The inclination of the shear fronts to the vertical pile axis is estimated to be $\sin^{-1}(240/5120) \approx 2.6^\circ$ by the difference in wave speed velocity in soil and pile. The inclination of the compression front to the vertical axis is estimated to be $\sin^{-1}(1890/5120) \approx 21.7^\circ$. It is important to note here that the Scholte waves generate pressure fluctuations in the fluid layer that can be particularly strong close to the seabed. The geometrical and material damping is relative high causing the Scholte wave to not propagates far in distance. Figure 5.10 illustrates the evolution of the wave propagation in the soil for 10, 50 and 100 m. This reflects the strong velocity decay in the relative short distance compared to the target distance of 750 m. The vertical velocity component in the fluid decays with 93% over 90 m distance, the vertical particle velocity component in the soil layer decays with 97% over 90 m distance. As a result, the vertical particle velocity in the soil reduces in amplitude around 1.04 times faster than in the fluid layer.

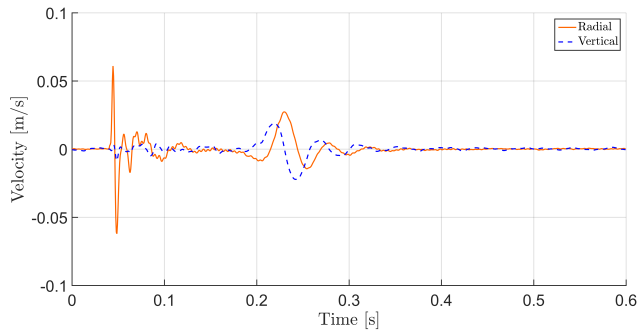


Figure 5.7: Vertical and radial velocity in fluid layer at 50 m from pile and 2 m above seabed

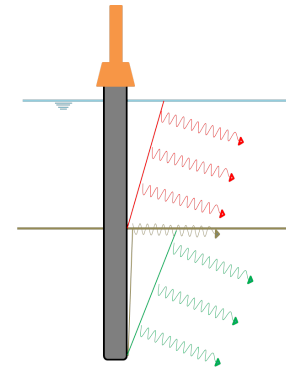


Figure 5.8: Inclination of propagating waves at fluid, soil-water interface and soil layer

5.3.3. Conclusions

Since the model predictions reach a horizontal distance of 100 m, and measured data is only available at 750 m, the SEL_{05} and L_{peak} levels have been extrapolated as shown in Figure 5.11. The obtained results are summarized in Table 5.2 and compared with the measured data. It is important to note here that by extrapolating the computed data a significant inaccurate response is obtained, but the only method to compare model results with measured data.

This shows an interesting phenomenon, namely that the closest to the seabed measured point results in a higher SEL and L_{peak} than at 12 m above the seabed. This is mainly related to the influence of the nearby soil and hence the shear and Scholte waves. The influence of the soil interaction on the far field is not possible to conclude on due to the use of the DFT. For this reason concluding on the noise levels at 750 m close to the seabed and further up from the seabed is not accurate and hence recommend to improve for further investigation. As a result, Table 5.2 summarizes the SEL_{05} and L_{peak} at two distances: 100 m and 750 m. Both results are compared with the Spring Dashpot model, and the results at 750 m are also compared with the measured data.

Large differences are revealed between both models and measured data due to the difference in soil modeling and the high uncertainty of the attenuation factors and soil elasticity. A crucial point in the analysis is to correctly estimate the attenuation of the Scholte wave with increasing distance from the source. Which on its turn is sensitive to the choice of α_p and α_s , the attenuation coefficients of the compressional and shear waves, respectively. The selection of the attenuation coefficients is done in section 3.3.2, but remains highly uncertain. Consequently, a parametric study is conducted in section 5.5 to gain more insight in the sensitivity of the attenuation factors and the soil elasticity.

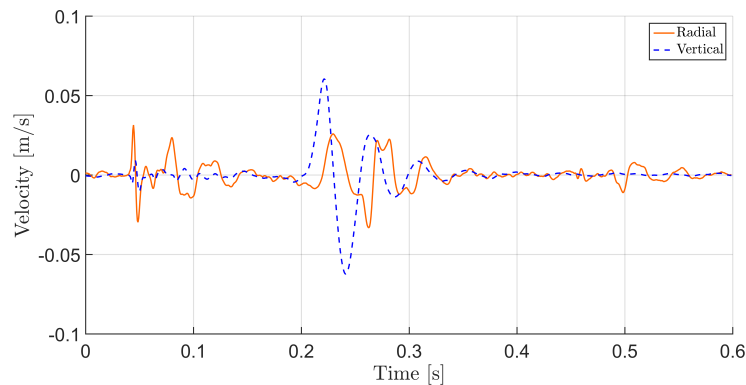


Figure 5.9: Vertical and radial particle velocity propagation in soil layer at 50 m from pile at soil-water interface

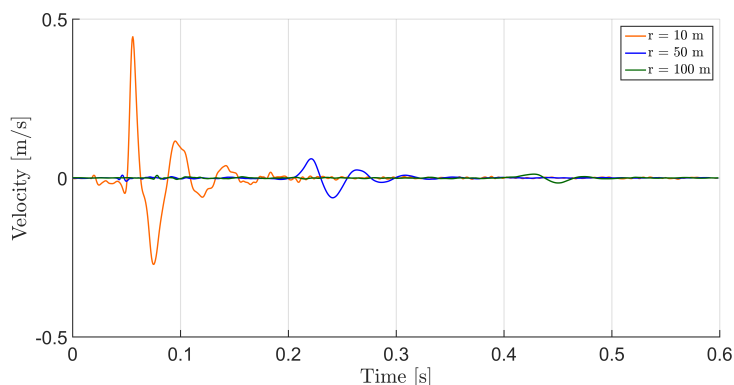


Figure 5.10: Vertical particle velocity in soil layer at 10, 50 m and 100 m from pile at soil-water interface

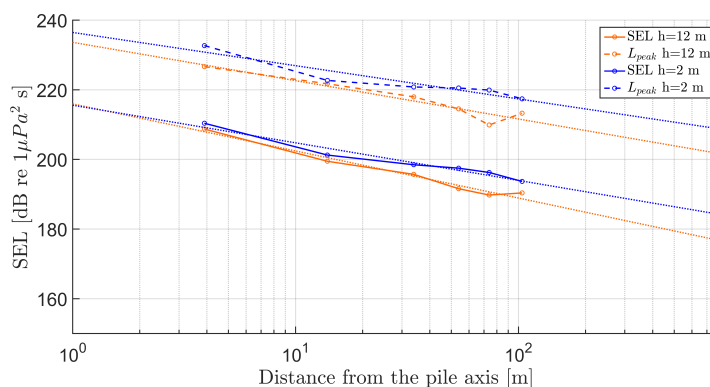


Figure 5.11: Noise levels, SEL_{05} and L_{peak} , evolution at $h = 2$ m and $h = 12$ m above seabed. The black marks at 750 m represent the measured SEL_{05} and L_{peak} .

Table 5.2: Comparison between computed SEL_{05} and L_{peak} with Elastic Medium model, Spring Dashpot model and measured data at 2 m above the seabed

Category	Distance m	Spring Dashpot model dB re $1\mu Pa^2 s$	Elastic Medium model dB re $1\mu Pa^2 s$	Measured dB re $1\mu Pa^2 s$ Error ± 2.5 dB	$\Delta SEL_{05} / \Delta L_{peak}$ -
SEL_{05}	100	175	194		+19
L_{peak}	100	201	217		+16
SEL_{05}	750		184	177	+7
L_{peak}	750		209	196	+13

5.4. Energy propagation

Another advantage of the present model is the ability to analyze the energy flow through the pile caused by the hammer impact and quantifying the amount of energy radiating into different layers. The focus is mainly placed, and discussed separately, on quantifying the amount of energy that:

1. Is irradiated directly into the fluid region, also referred as the primary noise path
2. Is carried by the Scholte waves that travel along the seabed-water interface and induce low-frequency pressure pressure fluctuations close to the seabed, also referred as the secondary noise path

5.4.1. Energy input into the pile

First the flux of energy through a cross section of the shell due to the compressional motion is calculated by taking the integral along the circumference of the product of the distributed axial force acting along the

z-direction and the vertical velocity of the mid-surface of the shell. In this case a cylindrical and symmetric shell is considered so the equation can be simplified by:

$$P_{shell}(z_0, t) = 2\pi R N_{zz}(z_0, t) \frac{\delta u_z(z_0, t)}{\delta t} \quad (5.3)$$

Since the energy that is transmitted to the shell is dependent on the velocity per height, and the velocity difference at each location, the energy flux will vary along the height of the pile as shown in Figure 5.12. This reveals the energy flux at three positions along the height of the pile and their relative differences. The energy diminishes as the resulting pulse from the hammer propagates downwards. This is due the radiation of the energy into the exterior medium and energy dissipation in the soil region. Remarkable is the amount of energy reflected from the downward traveling wave after hitting the seabed-water interface. First the speed for the compressional wave through the shell is estimated by the time and distance difference between the front of the first two pulses, resulting in 5120 m/s . Thereafter, the first reflected pulse reaches the same point again after around 15 ms. This corresponds to a traveled distance of about 75 m, which is slightly more than twice the vertical distance between the soil water interface and the position of that point. As a consequence when the downward propagating wave in the pile reaches the soil water interface, part of the energy is reflected upwards in the pile. In this case to an amount of about 10% of the energy carried by the initial pulse is reflected upwards. This is lower than for the case of smaller piles presented by Tsouvalas and Metrikine [2015] where an amount of around 15% reflected energy was determined with a pile of 0.92 m diameter in less dense soil.

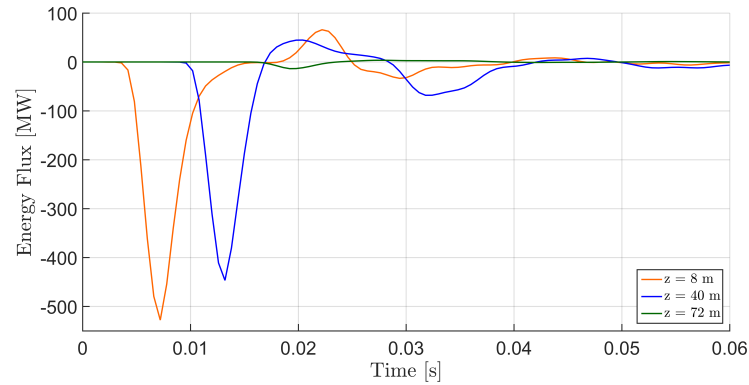


Figure 5.12: Energy flux at different heights along the pile (measured from the top) during stage 3

The ability to calculate the accumulated total energy per cross section of the pile is taken into account by equation 5.4 and illustrated by Figure 5.13.

$$E_{p,n}(z = z_0) = \int_{t_0}^{t_0+T} dt \int_0^{2\pi} P_{shell}(z_0, t) d\theta \quad (5.4)$$

Here a total inserted energy by the hammer into the system of around 1900 kJ is shown. The majority, about 90% of the inserted energy, is lost in the lower half of the pile which is embedded into the soil from 43.5 m. The remaining 10% of the input energy is radiated from the upper half of the pile into the fluid layer. This implies that the percentage of energy that efficiently radiates in the form of compressional waves by the primary noise path is relatively small. This percentage includes both the energy transferred into the pressure waves irradiated from the surface of the pile as well as the energy released into the Scholte waves.

5.4.2. Energy launched into the soil and fluid layer

In the previous subsection, it became clear that the amount of energy irradiated into the fluid layer is much lower than the energy which irradiates into the soil layer. This can also be visualized for the energy radiation along radial distance as done in Figure 5.14. The figure presents the percentage of total inserted energy that radiates along the radial distance from the pile. Accordingly three cases; soil, fluid and the cumulative of both are presented. This gives insight how the inserted total impact energy in the pile diffuses over distance between the soil and fluid layer.

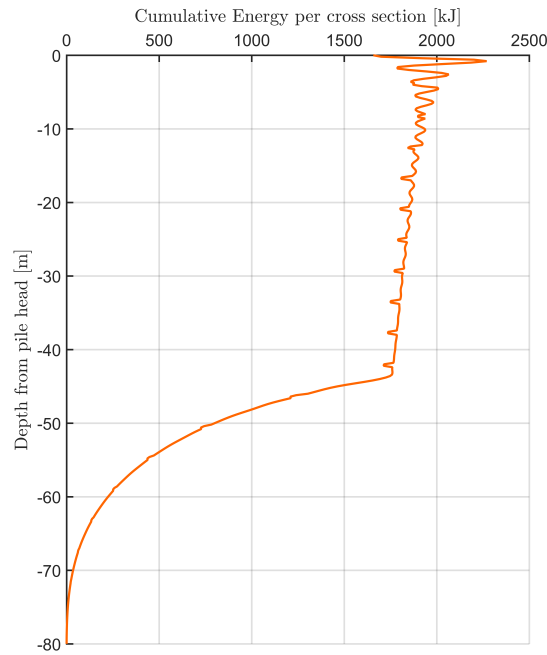


Figure 5.13: Cumulative energy along the pile

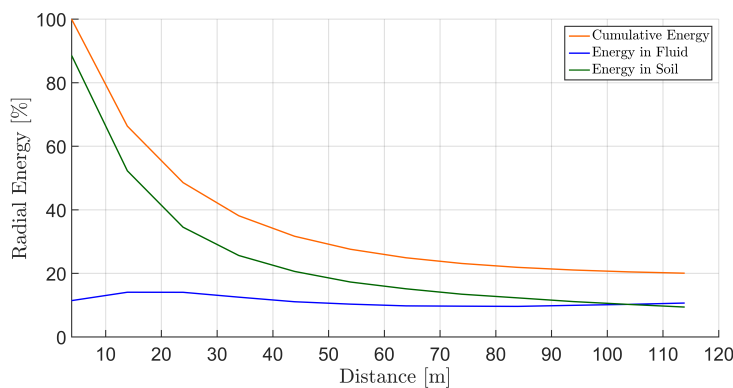


Figure 5.14: Percentage energy radiated into the soil and fluid layer during stage 3

At the pile surface, so zero radial distance, the radiated energy into the soil accounts for around 90% of the total input energy in the form of compressional, shear and Scholte waves. The remaining approximately 10% of the input energy irradiates into the fluid layer. As the distance from the pile increases, the amount of energy radiated into the fluid increases to around 14%. The energy radiated through the soil has a strong decay indicating a powerful transition of energy from the soil towards the fluid layer. To get a better view of the energy propagation between the two layers, attention is given to the instantaneous power radiated through a cylindrical surface. This can provide valuable insight regarding the amount of energy carried by different waveforms in the fluid and soil layer. Calculated by the surface integral of the normal component of the acoustic intensity over the water depth, Figure 5.15 shows the result for the fluid layer at four radial distances. The intensity is the average rate of flow of energy through a unit area that is normal to the direction of propagation. The intensity is defined by the product of the sound pressure and particle velocity.

Close to the pile surface the energy carried by the compressional and Scholte waves are indistinguishable. But when moving further from the pile surface, the differences increases and becomes visible. Two energy blocks

become visible from which the first one in time is related to the compressional wave front and the second is related to the energy carried by the Scholte wave that arrives much later in time than the compressional wave. It can be noticed that with increasing radial distance from the pile, both energy blocks decrease in magnitude. The strong decay of the second energy block, indicating the energy carried by the Scholte wave, does not have significant influence on the energy transmitted to the fluid as illustrated in Figure 5.14. For points positioned a few wavelengths away from the soil-water interface, the contribution of the Scholte wave can naturally be neglected.

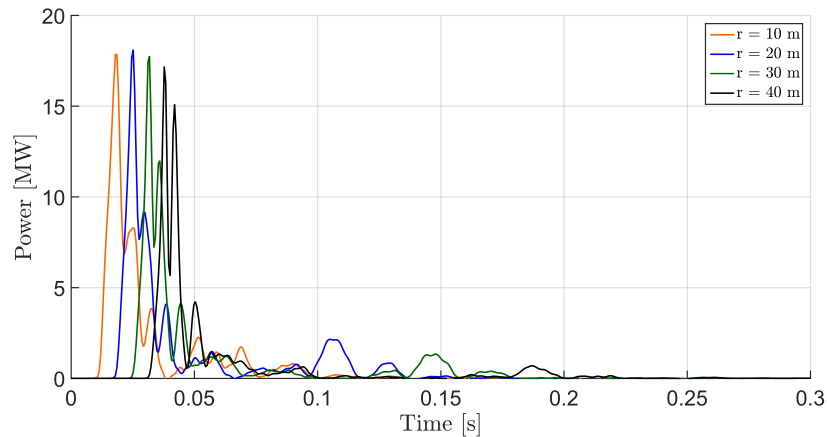


Figure 5.15: Instantaneous acoustic power in the fluid layer at four radial distances from the surface of the pile

The same method can be applied to the soil layer where the instantaneous power is calculated by the surface integral of the surface traction and the soil particle velocity vector. The instantaneous power in the soil layer is shown in Figure 5.16 for the similar four radial distances. The difference between the compressional, Scholte and shear waves becomes clear after 20 m distance from the pile. There the fast propagating compressional wave around 0.03 sec, and the shear and Scholte wave above 0.08 sec become visible. At 10 m distance, only a relative small part of around 12% of the total radiated energy in the soil is carried by the faster propagating compressional waves. Further away from the pile, at 40 m, the energy carried by the compressional wave has remain constant. However, the energy carried by shear and Scholte waves has decreased significantly with 90% compared to the energy at 10 m radial distance. From the total amount of energy propagating at 40 m through the soil, 40% is carried by the shear and Scholte waves. This means that a large part of the energy carried by the shear and Scholte waves is damped out. On top of that, it can be observed that the magnitude of acoustic energy radiated into the soil layer is significantly larger close to the pile than the acoustic energy radiated into the fluid. Moving further away, the energy carried by the soil becomes significantly smaller compared to the fluid layer.

From here it can be confirmed that only a small amount of the direct inserted energy in the pile is transformed into acoustic radiating energy in the fluid layer. However, the energy carried by the Scholte and shear wave that arrive later in time at the specific location, decrease with around 90% due to material dissipation within 30 m. As a result, the final propagating distance of the energy carried by the shear and Scholte wave is questioned.

A relative large part of the carried energy in the fluid layer is due to the fast propagating compressional waves. From the approximated 10 - 14 % of the total inserted energy, 15% travels as shear and Scholte waves and 85% in the form of compressional waves through the fluid layer. For the soil layer, around 86 - 90% of the total inserted energy travels through the soil. From the latter percentage, 88% travels as shear and Scholte waves and 12% in the form of compressional waves.

This means that of the total inserted energy, around 12% is attributed to the pressure wave generated by the compressional waves in the fluid layer, the so called primary noise path. On top of that, around 2% of the total input energy radiated into the fluid layer is carried by the Scholte waves at the soil water interface, the secondary noise path.

Although the results give a strong quantitative indication of the energy introduced into the fluid and soil

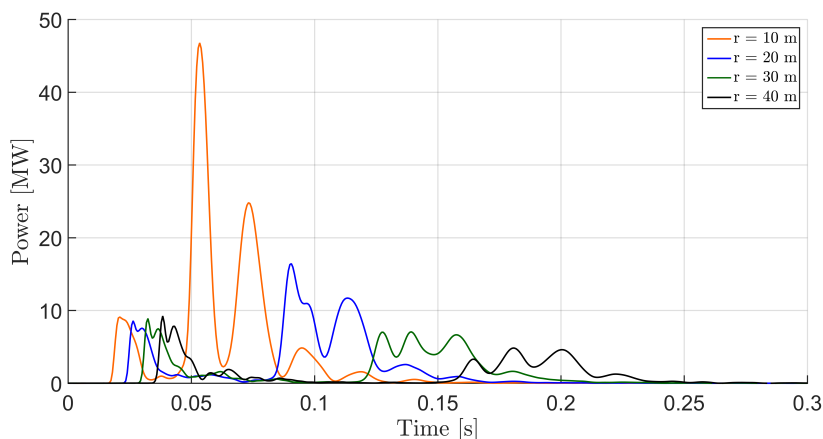


Figure 5.16: Instantaneous acoustic power in the soil layer at three radial distances from the surface of the pile

layer during piling, it is important to notice that in reality the losses in distance in the soil are expected to be larger. In the present model the soil is abruptly terminated with a rigid boundary at the maximum depth which results in a confinement of the energy into the waveguide. In reality, part of the energy will radiate into deeper soil layers which is not accounted for in the present model. The effect of the truncated medium is taken into account by a slightly increase in soil attenuation. Hence, the prediction of present model are expected to provide an upper boundary of the actual situation.

5.5. Parametric study

In order to assess the sensitivity of the elastic medium model, a study of how the uncertainty in the output can be appointed to different input is performed. The influence on the frequency spectrum of different physical quantities like soil elasticity and attenuation factor is here to be evaluated. Furthermore, the influence of two soil layers compared to one soil layer is analyzed. This enables the modelling of a marine top layer and a more dense sub layer. The material properties of the shell together with the geometry is summarized in Table 5.3. The applied force is from the original IHC S-4000 impact hammer, shown in Figure 5.3b.

For the first two parametric studies, three different cases are considered. The first case has an decrease of 50% in the then to analyze parameter, and the third case an increase of 100%. The second case serves as a reference case with the same settings as analyzed in section 5.3. For the sensitivity study of the multiple soil layers, only two cases are considered. The case with the multiple soil layer differs in all parameters of the soil conditions. The response is presented as the frequency spectrum of the pressure levels for two vertical distances from the seabed. Furthermore, the vertical velocity in the soil due to the propagating wave in time domain is analyzed for two radial distances. Finally, the (extrapolated) noise level at 750 m is presented.

Table 5.3: Material constants and geometrical parameters of the pile

Parameter	Value	Unit
E	$2.1 \cdot 10^{11}$	N/m^2
ν	0.28	-
ρ	7850	kg/m^3
η	0.001	-
z_1	4.5	m
z_2	43.5	m
z_3	20	m

5.5.1. Influence of soil elasticity

Due to the limited known specific soil information, a significant uncertainty in wave speed for both compressional and shear waves is present. As a result, it is interesting to examine the influence of different soil elasticity and corresponding wave speed. Three cases are considered whose properties are summarized in table 5.4. Case I corresponds to a soft soil layer, like marine sediment. Case III corresponds to a very stiff soil layer. In all three cases, the attenuation factors for the shear and compressional wave are remained constant.

Table 5.4: Three cases with different soil elasticity and corresponding compressional and shear wave velocities. The properties are based on reference Case II. Case I has a 50% decreased soil elasticity and Case III an 100 % increased soil elasticity with regard to Case II.

Layer	Depth m	E MN/m^2	ν -	ρ kg/m^3	c_p m/s	c_s m/s	α_p dB/λ	α_s dB/λ
Case I	36.5	210	0.487	1936	1200	191	1.2	3.8
Case II	36.5	420	0.487	1936	1697	270	1.2	3.8
Case III	36.5	840	0.487	1936	2400	382	1.2	3.8

The pressure levels are illustrated in Figure 5.17, for Case I, II and III. As can be noticed, reducing the soil elasticity with 50%, and hence the wave speeds, reduces the pressure levels in both vertical distances from the seabed. Close to the seabed, $h = 2$ m, the response is larger due to the influence of the soil. Over the entire frequency band width differences are observed. For frequencies higher than 200 Hz, the reduction of pressure levels is around 6 dB re $1\mu Pa$. Moving up in the fluid layer to $h = 12$ m, the difference is of the order of ± 3 dB re $1\mu Pa$. Remarkably however is the increase of pressure levels between 63 and 200 Hz at $h = 12$ m. Due to the decrease in soil elasticity, the amplitude of the compressional propagating wave through the fluid has increased at $h = 12$ m. This can be explained since a smaller portion of the input energy is absorbed by the soil and consequently a larger portion is left to radiate in the form of pressure waves into the fluid. Therefore the influence of the primary noise path, resulting in the compressional wave, increases. The main difference is located in the low frequency band width, below 200 Hz. Close to the seabed, the difference increases due to the affect of the high amount of low frequency waves propagating through the soil. When increasing the soil elasticity in Case III, similar results occur when decreasing the soil elasticity. The main influence is noticeable in the low frequency band width.

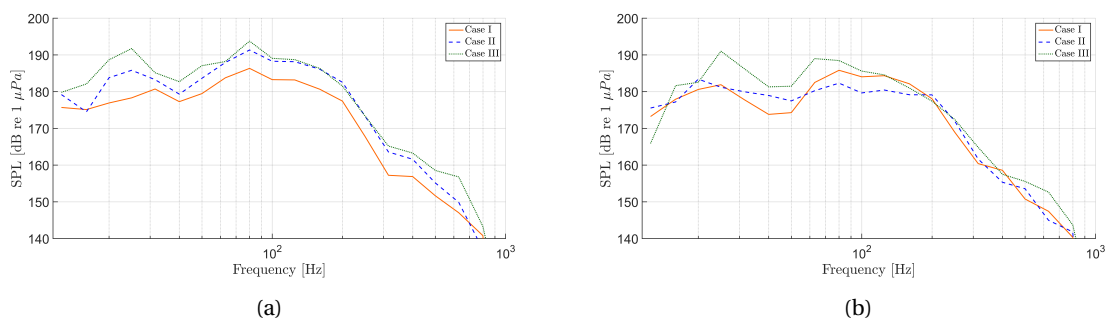


Figure 5.17: Pressure levels in 1/3-octave bands for Case I, II and III at 50 m from the pile and (a) $h = 2$ m above seabed and (b) $h = 12$ m above seabed

In Figure 5.18, the vertical velocity at the soil-water interface is shown for two radial distances from the pile. At the soil-water interface, mainly Scholte waves are present. The stiffer the soil, the higher the speed of the Scholte waves. The fast arriving small oscillations that are observed, are related to the compressional pressure waves in the soil and/or fluid layer. The oscillations that follow are related to the shear waves. With increasing distance into the soil with regard to the soil-water interface, the velocities in the soil decreases similar. This is due to the influence of the Scholte waves only close to the soil-water interface. Due to the decrease of the soil elasticity in Case I, the amplitude of the Scholte wave velocity decreases. Similar occurs with increased soil elasticity in Case III, where the amplitude of the Scholte wave increases and hence its influence.

Finally, the effect of of the soil elasticity and corresponding wave velocities is examined on the noise levels in

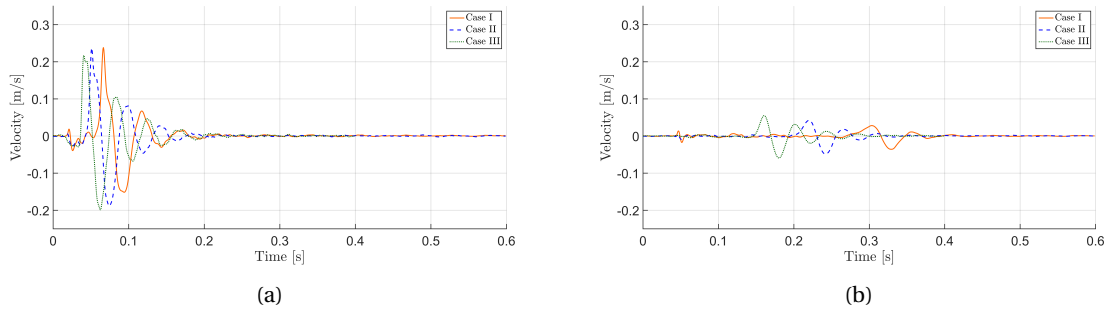


Figure 5.18: Vertical velocity propagation for Case I, II and III at soil-water interface and (a) at $r = 10$ m and (b) at $r = 50$ m

the fluid layer. This is illustrated in Figure 5.19 for all three Cases at 2 m above the seabed. As was expected, due to the decrease of soil elasticity in Case I, the SEL_{05} and L_{peak} at 750 m decrease, 9 dB and 10.5 dB respectively. On the contrary, the SEL_{05} barely increase with increasing soil elasticity. The L_{peak} even decreases slightly. A general conclusion is that for less stiff soil the pressure and corresponding noise level in the fluid layer decrease. The influence is large at frequencies below 200 Hz and close to the soil-water interface. Selecting the correct soil elasticity is therefore highly important.

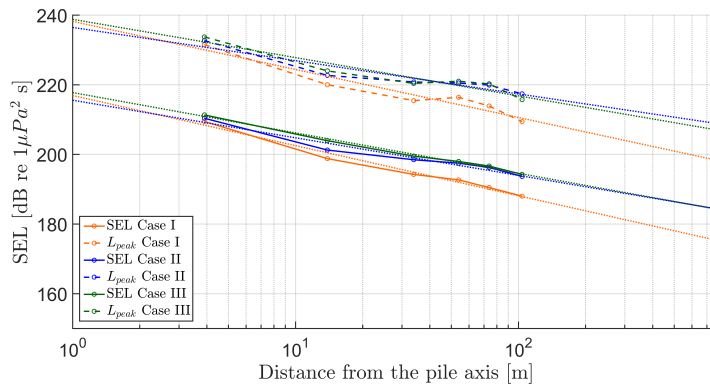


Figure 5.19: Noise levels, SEL_{05} and L_{peak} , evolution for Case I, II and III at 2 m above seabed. Extrapolated to 750 m. The black marks at 750 m represent the measured SEL_{05} and L_{peak} .

5.5.2. Influence of soil attenuation

In this section, the influence of the attenuation factors in the soil is evaluated. The attenuation factor represents the decay of the intensity of the response. This is partly due to the geometry of the propagating wave, and partly due to the an-elastic properties of the material through which it travels. As a consequence, correctly estimating the attenuation factor is of importance. Three cases are considered whose properties are summarized in table 5.5. In all three cases, the soil elasticity and corresponding wave velocities for the shear and compressional wave remain constant.

Table 5.5: Three cases with different soil attenuation factors. The properties are based on reference Case II. Case I has a 50% decreased attenuation factor and Case III an 100 % increased attenuation factor with regard to Case II.

Layer	Depth m	E MN/m^2	ν -	ρ kg/m^3	c_p m/s	c_s m/s	α_p dB/λ	α_s dB/λ
Case I	36.5	420	0.487	1936	1697	270	0.6	1.9
Case II	36.5	420	0.487	1936	1697	270	1.2	3.8
Case III	36.5	420	0.487	1936	1697	270	2.4	7.6

From Figure 5.20, it becomes rather fast clear how much affect the soil attenuation has on the pressure levels in the fluid layer with the current soil conditions. Almost no difference is observed between the three cases. Only in the very low frequencies, below 25 Hz, and close to the seabed a minor difference of less than 1 dB re $1\mu Pa$ is noticeable. This is influenced by the increase of the soil vertical velocity. As illustrated in Figure 5.21, the decrease in attenuation factors results in an increase of the vertical velocity. The first small oscillations refer to the fast arriving compressional waves. The later, and larger, oscillation refers to the shear wave. The later is much more influenced by the adjustments made to the attenuation factors. This is correlated to the fluctuation of the noise levels in the low frequency band width in the fluid layer.

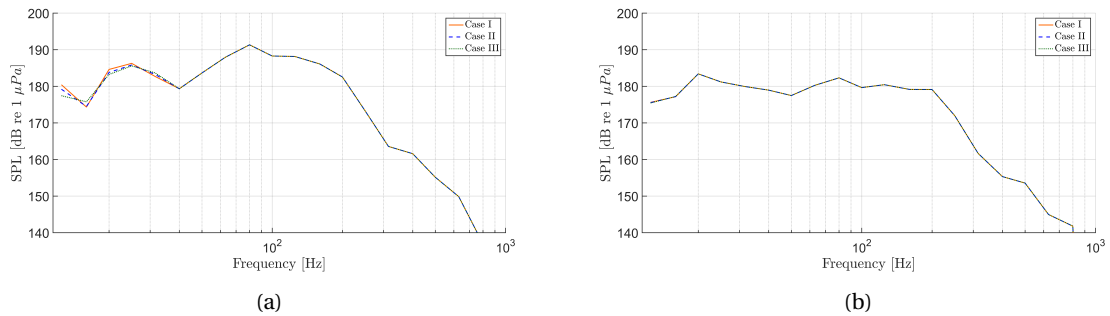


Figure 5.20: Pressure levels in 1/3-octave bands for Case I, II and III at 50 m from the pile and (a) $h = 2$ m above seabed and (b) $h = 12$ m above seabed

The contribution of the attenuation factor on the final noise level in the fluid is negligible as shown in Figure 5.22. No difference in the noise evolution is noticeable. In general, it can be concluded that in order to predict the noise levels in the fluid layer, the attenuation factor must be in the right order of magnitude, but does not require a high accuracy. This enables to reduce the uncertainty of selecting an attenuation factor in the soil.

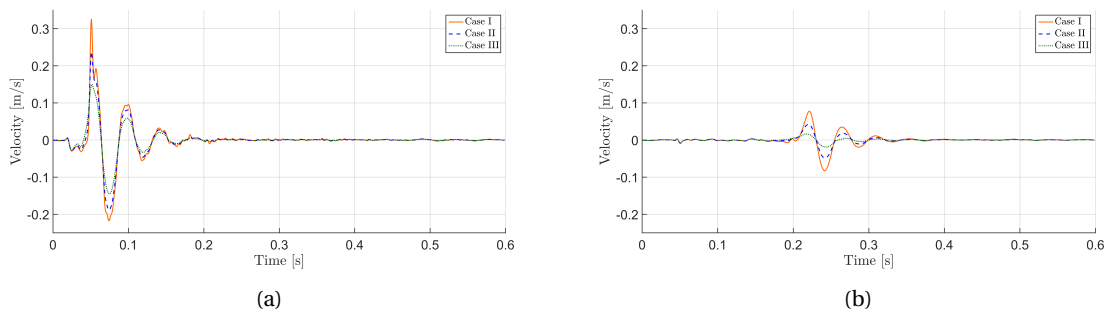


Figure 5.21: Vertical velocity propagation for Case I, II and III at soil-water interface and (a) at $r = 10$ m and (b) at $r = 50$ m

5.5.3. Influence of two soil layers

Having analyzed the sensitivity of the soil elasticity and soil attenuation factors on the response in the fluid layer, we proceed now with the analysis of two soil layers. Having two soil layers represents the conditions in reality better since this allows propagating waves in the soil to diverse into multiple velocities and inclination angles. The input parameters are summarized in Table 5.6 for two cases. Case I represents the same soil conditions as used previous as reference case. Case II represents the two layered soil, from which the top layer is defined as fine sand and the bottom layer more dense sand.

The pressure levels are illustrated in Figure 5.23 for Case I and II. As can be noticed, introducing multiple soil layers with the here presented specific parameters results in a reduction of the sound level. For the higher frequencies, the reduction is minimal. However, in the low frequency range the influence is more visible. Due to the decrease of the soil stiffness for the upper soil layer, the same principle as during the analysis of the soil elasticity occurs. As the elasticity decreases, the wave speed of the propagating waves through the soil de-

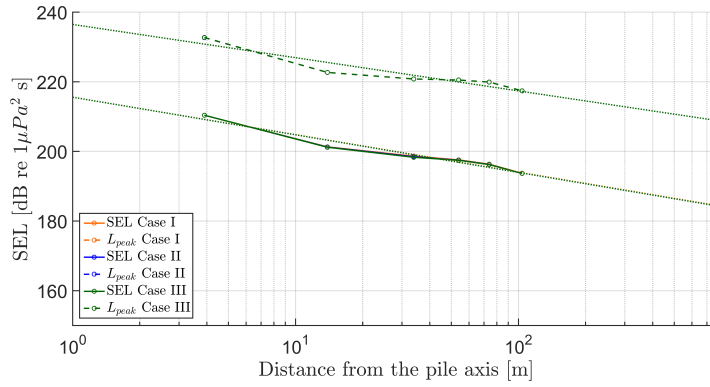


Figure 5.22: Noise levels, SEL_{05} and L_{peak} , evolution for Case I, II and III at 2 m above seabed. Extrapolated to 750 m. The black marks at 750 m represent the measured SEL_{05} and L_{peak} .

Table 5.6: Two cases with different soil layers and related parameters

Case	Layer	Depth m	E MN/m^2	ν -	ρ kg/m^3	c_p m/s	c_s m/s	α_p dB/λ	α_s dB/λ
Case I	Fluid	39	-	-	1025	1490			
	Soil	36.5	420	0.487	1936	1685	276	1.2	3.8
Case II	Fluid	39	-	-	1025	1490			
	Fine sand Sand-Silt-Clay	10 26.5	430 740	0.486 0.478	1906 2000	1669 1723	276 354	1.2 1.3	3.8 4.8

crease and therefore increases the cut-off frequency. This, on its turn influences the propagating modes and hence the frequency spectrum in the fluid layer. The Scholte wave propagates with less amplitude along the soil-water interface. Furthermore, the Scholte wave produces only pressure fluctuations in the water close to the soil-water interface and not further up into the fluid layer. Therefore the difference further up in the fluid layer becomes less.

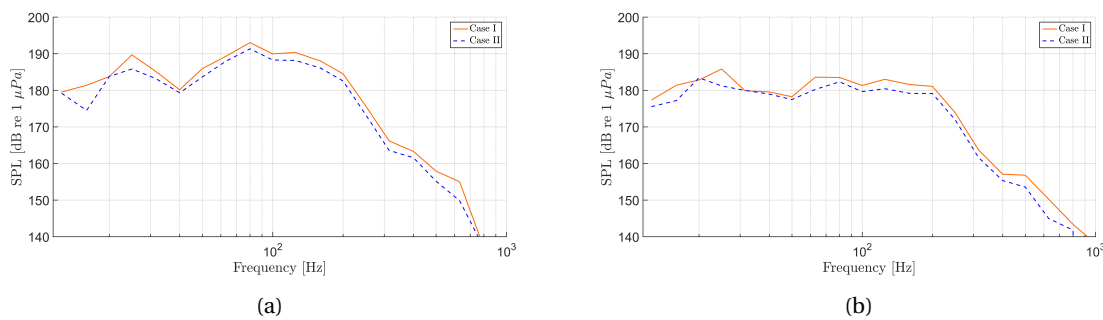


Figure 5.23: Pressure levels in 1/3-octave bands for Case I and II at 50 m from the pile and (a) $h = 2$ m above seabed and (b) $h = 12$ m above seabed

Finally, from observing Figure 5.24 it can be concluded that introducing two fluid layers does not significantly influence the final noise levels. It must be mentioned that the two fluid layers that are encountered in this analysis, do not differ significantly which might influence the analysis. Therefore the results are not expected to differ significantly. However, the present executed sensitivity analysis aims to gain insight in the consideration whether to select one or two soil models when the parameters are well known. To conclude, when the parameters are known, the difference in the fluid layer is minimal and hence not necessary to include.

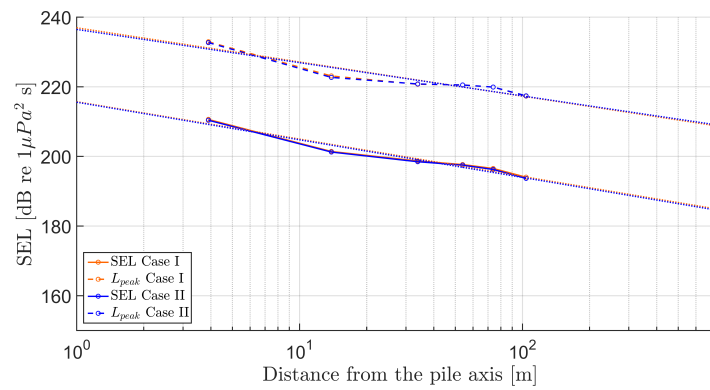


Figure 5.24: Noise levels, SEL_{05} and L_{peak} , evolution for Case I, II and III at 2 m above seabed. Extrapolated to 750 m. The black marks at 750 m represent the measured SEL_{05} and L_{peak} .

5.6. Conclusions

In this chapter, a more advanced model is presented compared to the model in the previous chapter. The main advantage of the here presented model is the addition of a soil layer. The soil is described as a three-dimensional elastic continuum able to support compressional, shear and Scholte waves. The fluid layer is described as a three-dimensional compressible medium with a pressure release boundary describing the sea surface. During this chapter, insight is gained in the model interface, parameters to be selected and corresponding response to generate a prediction of noise levels and wave propagation paths.

A validation of the model is performed in the time domain. However, no measurements are performed within the computed range, resulting in a comparison of the extrapolated noise levels at 750 m only. Due to the extrapolation, the model predictions are overestimating the noise levels at 750 m. This is mainly caused by the large influence of the energy at low frequencies carried by waves traveling along the soil-water interface.

Hereafter, an extensive analysis is performed on the noise propagation in the near field ($< 100m$) after impact on a large sized monopile. The analysis shows for the present soil condition a large influence of the soil. From the total inserted energy at the top of the pile, approximately 86-90% radiates into the soil layer in the form of compressional, shear and Scholte waves. The remaining energy radiates directly into the fluid layer. From the latter, around 12% is attributed to the compressional waves propagating directly into the fluid layer, the so called primary noise path. A smaller part of approximated 2% of the total input energy radiates as the secondary noise path in the form of Scholte waves along the soil-water interface. The attenuation of the Scholte wave is less in comparison with other propagating modes due to the relative slow wave speed. However, the Scholte wave produces only pressure fluctuations in the fluid close to the soil-water interface and not further up into the fluid layer. Their influence shows to be limited at longer distances, but the amount of energy lost in them is essential in order to be able to get a fair impression of the energy transferred into acoustic waves in the fluid layer.

For the Elastic Medium model, a sensitivity analysis of the soil parameters is performed. The influence of the following three parameters on the final response is examined, i) soil elasticity, ii) attenuation factors for the propagating waves in the soil layer and iii) multiple soil layers. The analysis shows a large diversity of the response to different soil elasticity's and corresponding wave velocities. For relative less stiff soil, the pressure and corresponding noise level in the fluid layer decrease. The influence is large at frequencies below 200 Hz and close to the soil-water interface. As a result, estimating a correct soil elasticity is crucial. Furthermore, the soil attenuation factors show to have negligible influence on the final noise levels in the fluid layer. The factor must be in the right magnitude of the analyzed soil material, but no high accuracy is required. Finally, the influence of two soil layers is analyzed. The analysis shows a minor influence on the noise levels in the fluid layer. Consequently, the influence is not significant when including multiple soil layers in order to predict the noise levels in the fluid layer correctly.

6

Pile Driving Analysis

Pile driving has become a highly important aspect of the whole underwater noise theme. During a pile driving analysis, all sort of important factors like bearing capacity and piling time are analyzed and predicted. This eventually also results in the amount of energy that needs to be inserted in the pile-soil system to be able to penetrate the pile to the desired depth. The energy and corresponding maximum peak force strongly correlate to the final underwater noise level. As a consequence, predicting these parameters correctly is of importance to be able to predict underwater noise levels and take appropriate measures. During this thesis, two types pile driving analysis were performed:

1. Analysis with existing hammers to obtain impact diagram to insert in acoustic models
2. Analysis with non-existing hammers by inserting an adjusted impact diagram to check drivability

The first type of analysis is perform with GRLWEAP, a pre-driving computational analysis tool for simulating pile response based on the solution of one-dimensional wave equation. Here all sorts of hammers can be selected to analyze the response on drivability. Theory behind GRLWEAP, and drivability models in general, is discussed in section 6.2. Adjusting the impact diagram to reduce the underwater noise level and verifying its drivability can not be performed with GRLWEAP. Consequently an own made pre-driving computational analysis tool is adopted for the second analysis listed above. Model description and validation is elaborated in section 6.3. Ahead of the models some more background information concerning pile foundations is given in section 6.1.

6.1. Mechanism of soil reaction

The final goal of the pile driving analysis is to assure sufficient bearing capacity of the pile. The bearing capacity is the total reaction force of the soil in response to the force exerted by the impact stroke on the pile. This consists out of two resistance types, namely the tip and shaft resistance. For pile driving there is a significant difference between the two, since the occurring resistance is based on different types of events. Settlement of a pile is caused by elastic and plastic deformation of the soil that can be separated into the following categories:

1. Loading: Under applied load, the soil will deflect elastically until the ultimate resistance, elastic limit, is reached. The hereby corresponding displacement is the quake value.
2. Sliding: The soil plastically deforms after exceeding the ultimate resistance.
3. Unloading: After removal of the load the elastic deformation will rebound to the final set. The final elastic deformation without load is zero, where the plastic deformation will remain without load.

During pile driving, stress waves are transmitted from the pile to the soil. As a result, the motion of the pile and the cyclic loading in the soils is transient in nature. The soil in the surrounding of the pile can store energy, elastic loading, and absorb energy because of plastic dissipation or structural damping. Plastic dissipation occurs in the highly strained zones nearby the pile in which soil undergoes plastic deformation. Damping originates from the nonlinear response of the soil. Usually expressed in the form of the damping

ratio, which represents the percentage of the input energy that is absorbed in the soil during a full stress cycle.

As the pile moves downward after each blow, it induces shear stress in the soil along its shaft. A thin shear band is formed around the pile at the moment the limit shaft resistance is reached. All plastic deformation happens inside that shear band. The soil outside the shear band remains elastic deflected. The soil region in the near field absorbs most of the energy, with the remaining energy propagating to the far field as radiation damping. If the pile were perfectly rigid, only vertical shear waves would radiate from the pile shaft. In reality, compressional waves are also generated because the pile is deformable and the upper sections of the pile are set in motion earlier than the lower sections as the hammer pulse travels downwards. However, the effect of compressive waves is much less significant, and the vertical shear wave dominates the mode of deformation around the pile shaft. Because of the high velocity of pile motions and the large induced strain rates in the soil, the strength of the soil inside the plasticity zones is likely to be higher than under static conditions. As a result, the limit shaft and base capacities are expected to be dependent on the pile velocity. This means that, in addition to structural damping and radiation damping, there will be energy absorption due to viscous damping inside the plastic zones [Loukidis et al.; 2008].

6.2. Theory of Pile Driving Models

Widespread interest in the method of pile driving analysis was started in 1960 by Smith [1960]. He used a numerical solution to investigate the effect of factors as ram weight, ram velocity, cushion and pile properties and the dynamic behavior of the soil during driving based on the one-dimensional wave equation. Most of the pile driving models nowadays are constructed in analogy to the dynamic pile driving model of Smith where he suggested the idealization of the pile system according to a series of mass, springs and dashpots as illustrated in Figure 6.1. This counts for the pile as well as for the hammer system. The action of each mass and each spring is calculated separately in each time interval. This way a mathematical determination may be made of stresses and pile displacement, against any amount of ground resistance. For the soil, the three earlier presented basic principles are taken into account for determination of the resistance; loading, sliding and unloading. These are based on the principle that the soil can compress elastically for a certain distance and thereafter plastically.

The soil resistance corresponding to a deformation is denoted by the ultimate bearing capacity R_u . This is the total reaction force of the soil in response to the force exerted by the hammer stroke on the pile. As here described, Figure 6.2 shows the assumed static load deformation that occurs as the pile moves through the soil. After the load is removed from the pile the final set is reached which is equal to the maximum displacement minus the quake. However, this principle fails to take into account the influence of time. Some piles penetrate the ground more rapidly than others that results in more instantaneous resistance. To overcome this effect, the viscous damping factor dependent on the velocity is introduced. The static resistance together with the dynamic resistance is the total soil resistance. This differs from the ultimate bearing capacity of the pile, since due to the temporary influence of the damping resistance, this will not contribute and so should not be taken into account. This principle works the same for the shaft resistance as for the tip resistance, only differs in specific values. Where the soil along the shaft mainly has to do with sliding, under the tip a different phenomena occurs. The soil under the tip of the pile is displaced with a certain velocity causing in an higher damping factor than along the shaft.

One of the first computer programs which were able to perform similar calculations was developed by Goble and Rausche [1986] and was named WEAP. After a few updates it was renamed to GRLWEAP, which is currently amongst many available programs the most widely used one. GRLWEAP software is pre-driving computational analysis tool for simulating pile response based on the solution of one-dimensional rod wave equation. GRLWEAP does not directly use the energy approach, but it rather uses the concept of energy losses and energy transfer as results of the pile driving. The most common analysis used in GRLWEAP is the bearing graph which is used to establish driving criteria in the field to assure quality assurance of piles. In the bearing graph calculations, an ultimate capacity is assumed and the corresponding set is calculated based on the resistance along the shaft and resistances at tip. Furthermore, the soil input is included in the program that allows to give detailed input of unit shaft and unit tip resistance per depth.

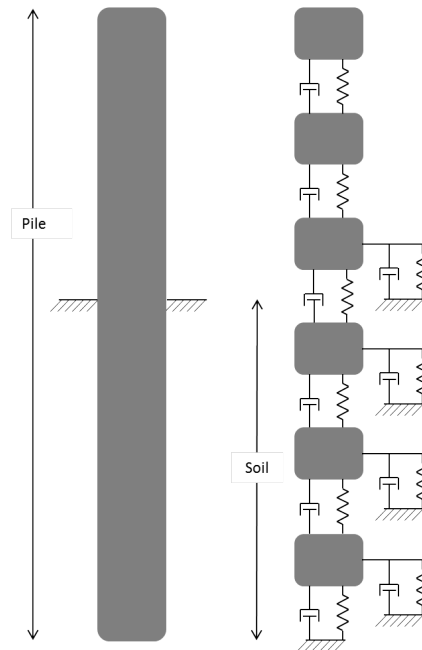


Figure 6.1: Schematic representation of drivability model based on method of Smith [1960]

However, the aim of this thesis is to obtain an impact diagram which is able to reduce underwater piling noise, but keeping the drivability unimpaired. Accordingly the adjusted impact diagram must encounter a drivability analysis. GRLWEAP is based as discussed above on the dynamics occurring between hammer and pile-soil interaction in which a lot of different hammers can be selected. Unfortunately, this results in no adjusted impact diagram that can be inserted. Since the hammer-pile dynamics is not the scope of this thesis, GRLWEAP can not be used for this purpose. Hence, in order to be able to perform a drivability analysis of the adjusted impact diagram, a new drivability model must be constructed.

6.3. Drivability Model

This section will discuss the theory of the drivability model developed by TU Delft and self made applicable for this research. The purpose of the model is to perform a simple check whether the pile reaches enough depth within sufficient time. The here adopted method is rather pragmatic, since it is not the main goal of this thesis. However, it is similar to the method as GRLWEAP uses and thus as the standard in the pile driving industry.

6.3.1. Basic theory of drivability model

The wave theory that describes the forward motion of the body under the action of a single hammer stroke and stress and acceleration occurring in the body as well as in the surrounding soil, is the basis for the pile driving theory. The wave equation is given as:

$$\frac{\partial^2 D}{\partial t^2} = c^2 \frac{\partial^2 D}{\partial z^2} \quad (6.1)$$

where D is the longitudinal displacement of a mass element of the pile along its vertical coordinate z and t in time. c represents the velocity of propagation of stress waves along the pile. In order to translate this mathematical relation with appropriate boundary conditions into a discrete numerical model, the pile is subdivided into $m = 1 \dots N$ segments which each have a mass. All of these masses are connected by springs with a spring constant K_m that represent the elasticity of the pile. Figure 6.1 visualizes the over here describe model building. According to Smith [1960], the formulas in the model assumes the corresponding scheme as follows in which the superscripts denotes the next time interval or mass:

$$D_m^n = D_m^{n-1} + 12\Delta t \cdot V_m^n \quad (6.2)$$

$$C_m^n = D_m^{n-1} - D_{m+1}^{n-1} \quad (6.3)$$

$$F_m^n = C_m^n K_m \quad (6.4)$$

$$Z_m^n = F_{m-1}^n - F_m^n - R_m^n \quad (6.5)$$

$$V_m^n = V_m^{n-1} + \left(\frac{Z_m^n}{W_m} \right) \Delta t \quad (6.6)$$

The spring constants of the pile elements are related to the elastic properties of the pile material and can be calculated by equation 6.7 and the spring constant of the shaft friction by equation 6.8.

$$K_m = \frac{\pi R_{pile}^2 E_{pile}}{\Delta L_m} \quad (6.7)$$

$$K_m^{soil} = \frac{R_m^u}{Q_{shaft}} \quad (6.8)$$

ΔL_m is the length of the spring K_m , D_m^n is the displacement of a mass block, C_m^n is the compression of a spring and F_m^n is the force exerted by a spring. Resulting in the net force on a mass element Z_m^n . Finally V_m^n is the velocity of a mass element. The model assumes a constant displacement over all springs along the pile axis noted as ΔL .

Aside of the parameters characterizing the pile material, the properties of the surrounding soil must be enclosed in the pile driving theory. This is of importance to finally come to a penetration resistance. Each weight of the pile system has a soil spring associated with it. Consequently the distribution of the soil resistance along the axial direction of the pile can be specified by proper choice of the constants that describe each individual soil spring. The spring can deform elastically to a limiting deformation Q , before plastic deformation sets in and no additional load is required to increase the deformation. Figure 6.2 shows the assumed static load deformation that occurs as the pile moves through the soil.

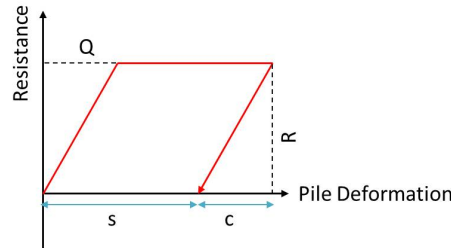


Figure 6.2: Static Bearing capacity and Quake

The yield of the spring stiffness along the shaft and at the tip during loading is corresponding with the quake by equation 6.9. During sliding, there is no further increase in static resistance but only dynamic resistance with increased displacement by equation (6.10).

$$R_m = (D_m - D_m^{soil}) K_m^{soil} (1 + J_{soil} V_m^{n-1}) \quad (6.9)$$

$$R_m = (D_m - D_m^{soil}) K_m^{soil} + R_m^u J_{soil} V_m^{n-1} \quad (6.10)$$

In the equation above, D_m^{soil} is the displacement of the soil element connected to a particular pile element along the pile axis and J_{soil} is the damping constant of the soil associated with mechanical energy stored in the system. For the quake Q , GRLWEAP uses a pre-defined very common value of 2.54 mm for the tip and shaft. It must be mentioned here that this value does not take the large size of the monopile into account. However, in order to keep the drivability analysis similar to one done by GRLWEAP, this value has been adopted for this drivability model as well. Research done by Middendorp and Verbeek [2004] unveils that the loading quake is not similar as the unloading quake and suggest a value of 80% of the loading quake. The soil resistance corresponding to a deformation is denoted by the ultimate bearing capacity R_m . This is the total

reaction force of the soil in response to the force exerted by the hammer stroke on the pile.

Now that all formula's are known, the final pile and soil displacement can be evaluated. In order to make the impact diagram sufficient to drive the pile into the soil, the pile displacement at the tip must be able to overcome the quake value and thus has a set.

6.3.2. Validation of drivability model

This section the validation of the drivability model is discussed. The validation is performed with computed data from GRLWEAP and computed data from the here presented drivability model after impact with the IHC S-4000 hammer.

To create a fine mesh of the pile similar to the one used in GRLWEAP the presented parameters in Table 6.1 are adopted and inserted in the drivability model. The mesh size must correlate with a time interval that is small enough to capture a wave with the adopted wave speed. As a result the time interval of $(5120 * 2)/1 = 10240 \text{sec}^{-1}$ was selected.

Table 6.1: Input parameters for drivability model. The parameter m is the amount of masses and n is the amount of time steps to take

Parameter	Value	Unit
n	1000	-
m	80	-
dt	10240	sec^{-1}
dx	1	m
c	5120	m/s
E	2.1	GPa
$Q_{loading}$	2.54	mm
J_{shaft}	0.164	s/m
J_{tip}	0.492	s/m

Exiting the system with the IHC S-4000 hammer, the impact diagram of which is illustrated in Figure 3.3, results in a force propagation through the pile as shown in Figure 6.3. This shows the force distribution at the top, mid and bottom (Tip) segment of the pile computed with GRLWEAP and the drivability model. As can be seen, the force distribution at all three segments is nearly identical in the first main pulse. The second pulse however, which is the reflected wave as can be seen by decreasing time difference when moving down the pile, exhibits more differences. This is due to the simplicity of the model. Finally, this will not make any difference to the vertical tip displacement due to the significant lower peak force of the reflected wave resulting in not being able to overcome the quake. Only the first main peak is able to do so and thus most of importance to predict correctly, which is done in this model.

Figure 6.4 shows the cumulative input energy comparison at the top of the pile for both models during stage 3. This reveals a good overlap between both models during the energy build up phase, and a slightly but negligible difference afterwards. The larger difference after 0.035 sec is because of the reflected wave causing an upwards vertical velocity in the pile, resulting in the energy to settle around a new value. In the drivability model this is not taken into account. Hence, it can be noticed that the downward propagating waves in the pile, which cause the final sliding of the pile, are modeled the same as the standard drivability models like GRLWEAP. This can be substantiated by Figure 6.5 where the dynamic resistance against the tip displacement is given. Part one, from zero displacement till the quake value, is the elastic loading path where resistance is build. Part two, from the quake till maximum displacement, is the plastic loading path, characterized by sliding of the pile. Here the static resistance force remains constant and only the dynamic, which depends on the velocity, resistance increases slightly. From the moment the vertical velocity in the pile starts becoming negative again, meaning no further sliding, the displacement decreases along the unloading part till 80% of the quake.

Finally, the governing factor of the whole drivability analysis, the displacement of the pile tip, can be examined and compared to results from GRLWEAP. Figure 6.6 shows the displacement of the three segments versus

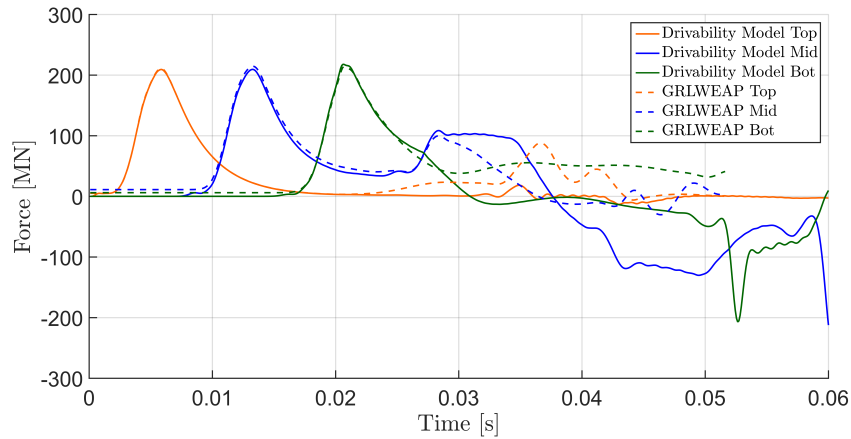


Figure 6.3: Force propagation along pile from drivability model and GRLWEAP at three cross sections of the pile during stage 3

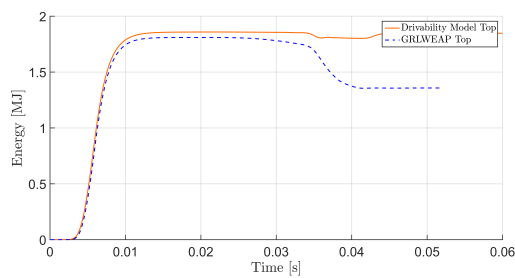


Figure 6.4: Cumulative energy from drivability model and GRLWEAP during stage 3

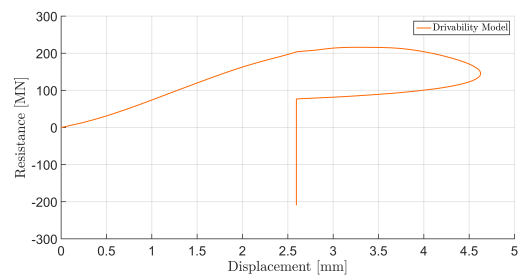


Figure 6.5: Tip Resistance from drivability model during stage 3

the time and Figure 6.7 zooms in on the tip displacement. Likewise the loading path is almost identical, only the unloading differs. From the results of GRLWEAP it can be seen that after a short duration, the displacement tends to shift towards a constant value. This value corresponds with the predictions from the drivability model for the tip. The mid and top section must finally also converge till the tip displacement value after time.

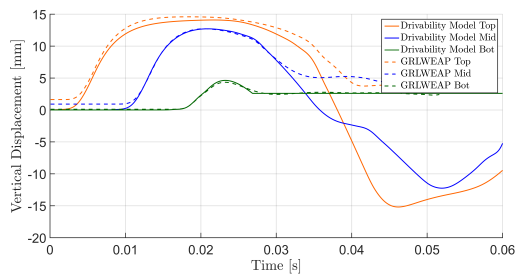


Figure 6.6: Vertical displacement from drivability model and GRLWEAP at three section of the pile during stage 3

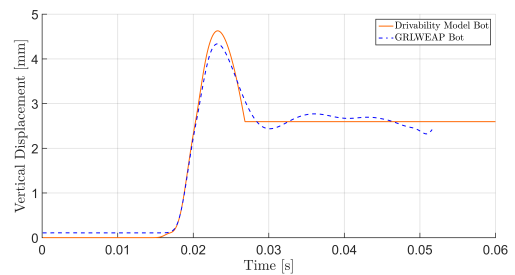


Figure 6.7: Vertical displacement from drivability model and GRLWEAP at tip of the pile during stage 3

6.4. Conclusions

In order to keep the drivability with the optimized impact force unimpaired, a basic non-linear drivability model is developed based on mass, springs and dashpots. The drivability predictions match with the predictions of GRLWEAP. Consequently, the drivability model is applicable to use. This makes it now able to validate any adjusted impact diagram on its drivability. During chapter 8 this is performed and discussed.

A crucial point in the analysis is the influence of the large size diameter of the monopile. Increasing the size

results in a change of dynamics in the monopile. Subsequently, the pile driving analysis procedure is affected. The non-linearity is limited to the description of the sliding of the pile into the soil with locally reacting non-linear springs. Furthermore, no radial springs are taken into account that account for the increased shaft area of a large sized monopile.



Model Comparison

During this research four different models are used. Two models for acoustic anal and two models for drivability predictions. All four models are listed below:

1. Spring Dashpot Acoustic Model
2. Elastic Medium Acoustic Model
3. GRLWEAP
4. Drivability Model

The Spring Dashpot and Elastic Medium acoustic model are used to predict and analyze the noise generated during the installation process. This has been done after excitation with the IHC S-4000 impact hammer and a parametric study with the BLUE Piling hammer. GRLWEAP and the drivability model developed by the TU Delft, are used during this thesis for analyzing the pile drivability. With GRLWEAP the impact diagram that is required to overcome the bearing capacity till a proper penetration depth is obtained. Subsequently, the impact diagram serves as input for both acoustic models and is later on optimized in order to reduce the underwater noise during pile driving activities. For the optimized impact diagram, it must be assured that it is capable of driving the pile towards the required penetration depth. For this purpose the drivability model of the TU Delft is developed.

Accordingly, the present acoustic models can only be used for noise predictions and not for sliding of the pile along the soil. On the contrary, both drivability models do account for sliding but not for noise evolution. All four models are finally used together in order to reduce the underwater piling noise, consequently their similarities must be justified.

All four models are based on the one-dimensional wave equation in the shell, which is dependent on the propagating velocity. Hence, the velocity in the shell is a fundamental quantity that serves as a base for all four model responses. For both acoustic models, the pile is described by the thin shell theory which includes the effects of shear deformation and rotational inertia. The velocities propagating in the shell are the foundation of the final propagating pressure waves. For the drivability model, the velocities in the shell determine the displacement of the pile with regard to the soil. As a consequence, by justifying the equality of the velocities in the shell, all four models can mutually be compared. The force evolution in the shell is examined by the energy evolution due to its dependency of velocity and force. When both physical characteristics are justified, all four models can independently be used. The here presented section will zoom into the comparison at the top of the pile for the velocity level and energy level.

7.1. Velocity Comparison

To start with, the velocity profile due to vertical material compression in a cross section of the pile is compared. In general no disturbance is allowed to propagate faster than the wavefront propagating through the pile. For the steel material of the pile, the compressional wave can propagate with a speed of about $c_p = \sqrt{E/\rho} = 5172m/s$. This estimation is based on an one-dimensional longitudinal model for the pile

with no surrounding medium. The actual speed is slightly different depending on whether the pile is surrounded by fluid or soil and on the dispersion characteristics of the shell. Positions which lie ahead of the first wavefront propagating through the pile should remain undisturbed. Figure 7.1 illustrates the vertical velocity against time after impact in a cross section at 8 m from the top of the pile for all four models.

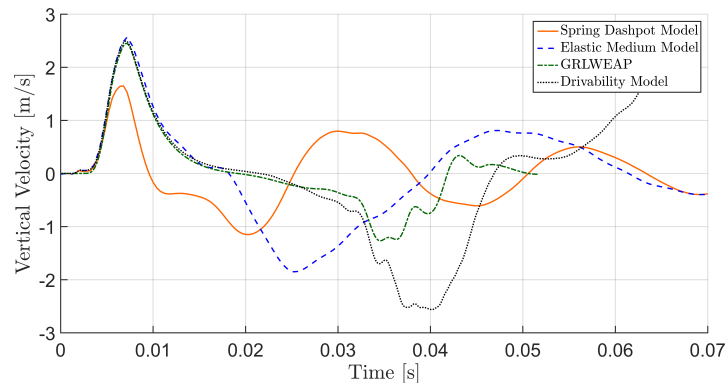


Figure 7.1: Vertical velocity at 8 m from the pile top after impact for all four models

The first peak is related to the downward propagating vertical velocity through the shell of the pile due to the impact of the hammer. The positive vertical velocity indicates the downward propagating wave. On the contrary, the negative vertical velocity indicates the upward propagating wave. It can be seen that both acoustic models show a shorter time period between the downward and upward propagating wave in comparison to the drivability models. This highlights a difference in modeling methods between the drivability and acoustic models.

In the Spring Dashpot model, the soil is substituted by uncoupled elastic springs and viscous dampers in all directions along the part of the shell which is embedded in the soil. The magnitude of the total damping usually depends on a number of parameters such as the excitation frequencies, the geometry of the soil-pile interface, the geometrical boundaries, the mode of the oscillation and the stress-strain characteristics of the soil [Tsouvalas and Metrikine; 2013]. Here, the substitution of the soil is done by a collection of springs and dashpots, who are independent on previous summed parameters. This introduces large uncertainties into the calculations. In the Spring Dashpot model, the soil material damping is expressed in terms of equivalent damping ratios through the entire excited frequency range for a certain strain rate. The spring coefficients are assumed constant throughout the frequency range with average values retrieved from their corresponding stiffness. In order to remove the uncertainty of defining the spring and dashpot coefficients, the Elastic Medium model was developed. By a three-dimensional description of the soil, the need for realistic estimation of the spring and dashpot coefficients is avoided since simple basic soil properties are only required for a complete soil description.

In order to further investigate the affect of the soil on the wave propagation through the pile, the vertical velocity per time step through the length of the pile is shown in Figure 7.2 for all models. For the Spring Dashpot model it is remarkable to observe that the vertical velocity is already present in the soil embedded region just after impact. This indicates an influence of the downward propagating wave on the soil modeling. Due to the long time duration of the impact force, a large amount of low frequency waves are excited. The model is solved in the frequency domain and account for frequency dissipation. At low frequency, the wavelength is long and the front of these waves may be already close to the soil layer just after impact. Subsequently, the pile starts deforming together with the soil and hence influence the stiffness of the complete system. Consequently the vertical velocity from the initial moment in time is influenced in the Spring Dashpot model. Both drivability models are solved in time domain and hence not account for frequency dissipation.

Another observation in the Spring Dashpot result from Figure 7.2a is the negative velocity at the back of the propagating wave front. The same observation is done in Figure 7.2b for the Elastic Medium model after around 0.014 sec. Due to the elasticity of the shell, and the fact that in both acoustic models the pile is clamped at the tip and free at the top, the vertical velocity becomes negative at the back of the wave front.

This affect is not taken into account in both drivability models and hence differ in their response as illustrated in 7.2c and 7.2d. Due to the representation of the soil in the Spring Dashpot model, this affect is enlarged as springs do not account for the non-local soil reaction. This affect is however of importance due to the large amount of low frequency waves with corresponding long wavelengths and hence non local reactions. By changing the soil elasticity, the affect of the soil resistance on the vertical velocity propagation is examined.

7.1.1. Influence of Soil Elasticity

To reveal the uncertainty of the spring and dashpot coefficients in the Spring Dashpot model, the response on the vertical velocity in the pile is further examined. By varying the soil elasticity, the spring and dashpot coefficients are influenced. Accordingly, four cases are considered in which the soil elasticity is varied, ranging from 0.01 to 10 times the reference value of 50 MPa. The reference case is based on the parameters adopted in chapter 4. The inserted soil elasticity values and corresponding spring stiffness's are summarized in Table 7.1.

Table 7.1: Four cases with different soil elasticity. The properties range from 0.01 to 10 times the reference soil elasticity value of Case III

Layer	Depth m	E MN/m^2	ν -	ρ kg/m^3	k_r MN/m	k_z MN/m	k_θ MN/m
Case I	36.5	0.5	0.4	2000	113.7	56.8	56.8
Case II	36.5	5	0.4	2000	1137.7	568.8	568.8
Case III	36.5	50	0.4	2000	11377	5688.5	5688.5
Case IV	36.5	500	0.4	2000	113770	56885	56885

In Figure 7.3 the vertical velocity in the pile at 8 m distance from the top is shown for the four cases. It can be noticed that the variation of the spring coefficients influences the vertical velocity in the pile. Decreasing the soil stiffness with a factor 100, increases the the vertical velocity with a factor of almost 2. On the contrary, increasing the spring stiffness with a factor of 10, results in a decrease of a factor of 5.5. The stiffer the spring, the more negative velocity at the back of the wavefront is present.

In Figure 7.1 it can be observed that the vertical velocity in the Spring Dashpot model turns negative at 8 m from the top of the pile after around 0.014 sec. With a propagating velocity through the steel material close to $5172m/s$, the wave is reflected after around 72 m. This is close to the distance of the wave traveling from the selected cross section at 8 m from the top of the pile, till the seabed and back. However, from the findings obtained from Figure 7.2 it is unlikely that the reflection is caused by the instant contact with the seabed. More likely is an overestimation of the overall stiffness of the modeled soil. With the large amount of low frequencies and hence long wavelengths, the pile starts to deform instantly with the soil. Consequently, the stiffness of the soil and pile are combined. Resulting in an overestimation of the complete stiffness. Due to the uncertainty of the spring and dashpot coefficients, an overestimation of the soil stiffness and damping has occurred in chapter 4. There the adopted value for the soil elasticity was 50 MPa and selected based on previous work done by Tsouvalas and Metrikine [2013]. In which the author also indicates the uncertainty of selecting the correct coefficients. For both drivability models, the soil is different represented and the downward propagating wave is reflected at the tip of the pile.

As a result of the high stiffness of the soil, the frequency depended propagating waves in the pile are influenced. The impact forces excites a number of frequencies depending on its frequency band width. In this research, due to the large amount of energy to be inserted during the pile driving process, the excited frequencies are relative low. This means that a large amount of low frequencies are excited, which have a relative large wavelength. Consequently, the large wavelengths are reflected when reaching the position in the pile where the surrounding medium passes from fluid into soil. This is the position where the surrounding stiffness increases. The large wavelength waves can therefore not propagate completely and hence influence the vertical velocity in the pile. This decreases the evolution of the vertical velocity.

The Elastic Medium model and both drivability models have a better representation of the soil stiffness and damping. As a result of the large uncertainty, and due to the now know effect of the soil elasticity on the vertical velocity response, the model comparison is continued with an corrected soil elasticity value. One that does match the response of the other three models and hence makes it possible to compare the response

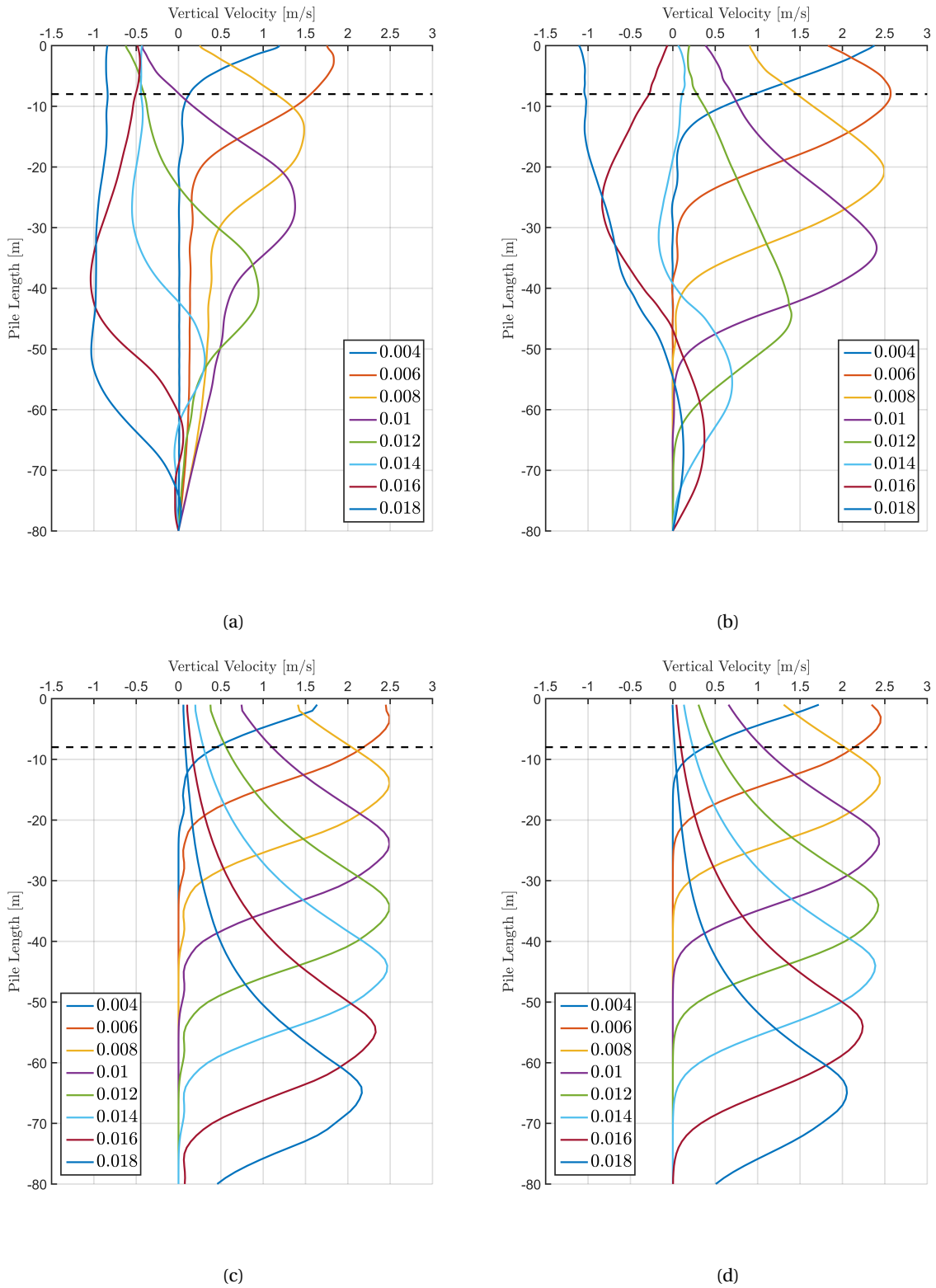


Figure 7.2: Vertical velocity propagation along length of pile for a) Spring Dashpot Model, b) Elastic Medium model, c) Drivability model and d) GRLWEAP. The black dotted line indicates the 8 m cross section position

mutually.

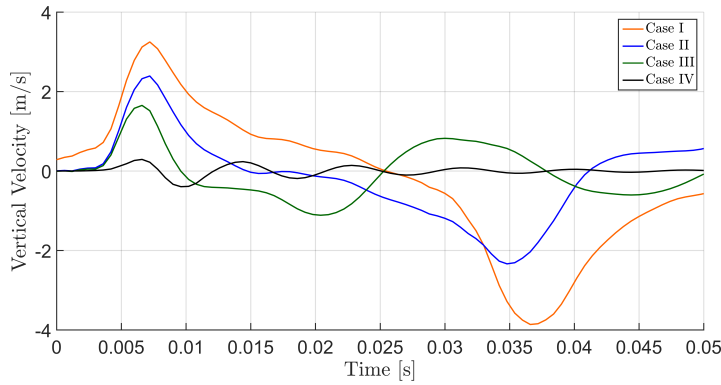


Figure 7.3: Comparison of different soil spring stiffness at 8 m from the top of the pile for the vertical velocity

7.1.2. Corrected Velocity Comparison

In previous subsection it was shown that the spring stiffness in the Spring Dashpot model was set too high compared to the Elastic Medium model soil representation and both drivability models. As a result, and to indicate the similarities between the models, the soil elasticity is here corrected to a value that represents the soil stiffness better. The peak vertical velocity of the downward propagating wave must be of around 2.4 m/s . This is between the response of case I and II in Figure 7.3. Consequently, the here adopted soil elasticity has a value of 2.4 MPa. This results in a vertical velocity propagation along the length of the pile as illustrated in Figure 7.4. This reveals the influence of the soil elasticity on the velocity of the downward propagating wave. Low frequency waves with long wavelengths are less affected by the soil resistance. Resulting in a similar vertical velocity profile along the pile as both drivability models. Finally, for all four models together the vertical velocity versus time is shown in Figure 7.5.

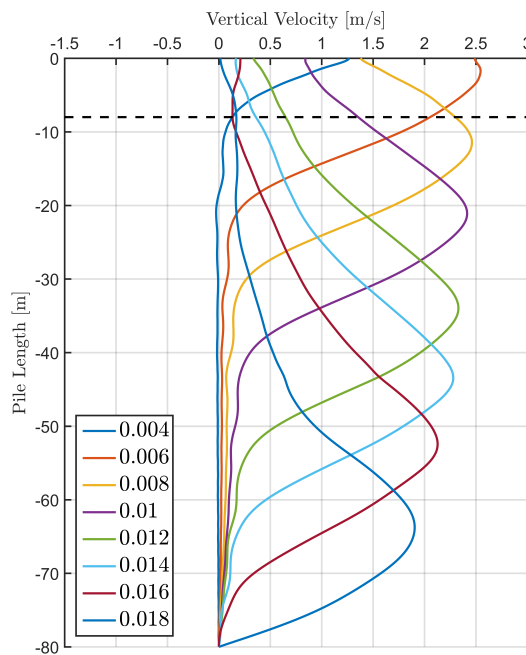


Figure 7.4: Vertical velocity propagation along length of pile for the corrected soil elasticity of the Spring Dashpot Model. The black dotted line indicates the 8 m cross section position

From here it can be seen that the predictions of the vertical velocity in the pile of the Spring Dashpot model

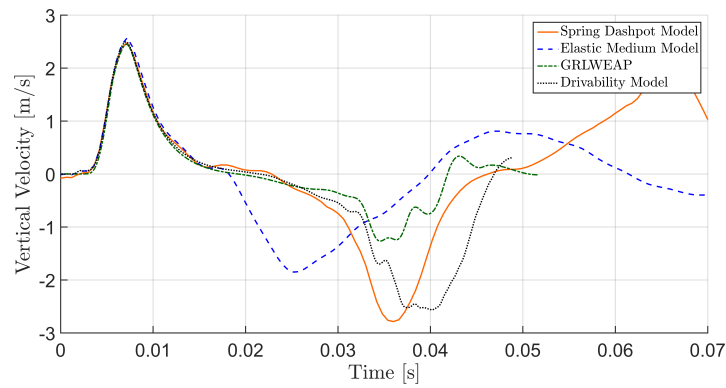


Figure 7.5: Vertical velocity at 8 m from the pile top after impact for all four models. With the soil elasticity of the Spring Dashpot model corrected in order to fit the results.

match with the other three models. On top of that, a remarkable observation is done. The velocity evolution after some time, the time needed to travel till the tip of the pile and back, fits the predictions of the drivability models to a certain extent. Especially the comparison between the TU Delft drivability model and the Spring Dashpot model are reasonably similar. Both are based on a distribution of springs and dashpots to represent the soil. This means that the Spring Dashpot might be able to encounter for sliding of the pile as well. Having a combination of both acoustic prediction and drivability would make the model more useful.

The drivability model was updated with a soil model, in which the friction data is inserted as calculated in section 3.1. This results in a soil resistance force along the shaft and tip of the pile per depth. The gradient of the bearing capacity versus the quake value of the soil, as illustrated in Figure 6.2, represents the resistance force of the soil by:

$$k_z = \frac{R}{Q} \quad (7.1)$$

Subsequently, per soil layer, the model calculates the stiffness of the soil along the shaft and tip. The drivability model only consists of vertical springs and dashpots, and hence no radial affects are taken into account. The soil damping is inserted as a factor and is depth independent. Based on the influence of the soil stiffness, the vertical velocity in the pile is calculated. As a result, a representation of the soil is relative simple obtained and could be of use for the Spring Dashpot model. Table 7.2 compares the obtained spring stiffness of the drivability model and the Spring Dashpot model in the vertical direction for two soil elasticities. Obtaining insight in the spring stiffness on this matter, could result in more accurate soil predictions.

Table 7.2: Vertical spring stiffness for Drivability model and Spring Dashpot model.

Layer	Depth <i>m</i>	Drivability Model	Spring Dashpot Model <i>E_{soil} = 50MPa</i>	Spring Dashpot Model <i>E_{soil} = 2.4MPa</i>
		<i>k_z</i> <i>MN/m</i>	<i>k_z</i> <i>MN/m</i>	<i>k_z</i> <i>MN/m</i>
S1	2.0	268.2	5688.5	268.2
S2	10.2	268.2	5688.5	268.2
S3	16.9	908.2	5688.5	268.2
C1	19.7	438.6	5688.5	268.2
S4	23.2	1325.7	5688.5	268.2
S5	24.7	417.8	5688.5	268.2
C2	26.2	438.6	5688.5	268.2
C3	28.1	438.6	5688.5	268.2
S6	29.9	1709.6	5688.5	268.2
S7	32.4	2516.7	5688.5	268.2
S8	37.0	2006.3	5688.5	268.2

The results of the comparison of spring stiffness reveal an overestimation of the stiffness in the 50 MPa soil elasticity case in the Spring Dashpot model. On the contrary, the drivability model and the 2.4 MPa soil elasticity in the Spring Dashpot model show similar spring stiffness in the upper layer. This is remarkable since the soil elasticity is selected based on the vertical velocity, resulting in a similar spring stiffness in the upper layer. Moving further down, the stiffness in the drivability increases due to the soil conditions. Since the Spring Dashpot model does not account for variations in depth, the complete soil stiffness is underestimated when only fitting the soil stiffness to the upper layer. As a result, the noise levels increase and the prediction loses accuracy. Hence, introducing multiple soil layers with a variety in spring stiffness is favorable. The Elastic Medium model has a slightly different vertical velocity evolution path. The main peak is well predicted. But when moving further, a negative velocity occurs due to the earlier defined low frequency influence.

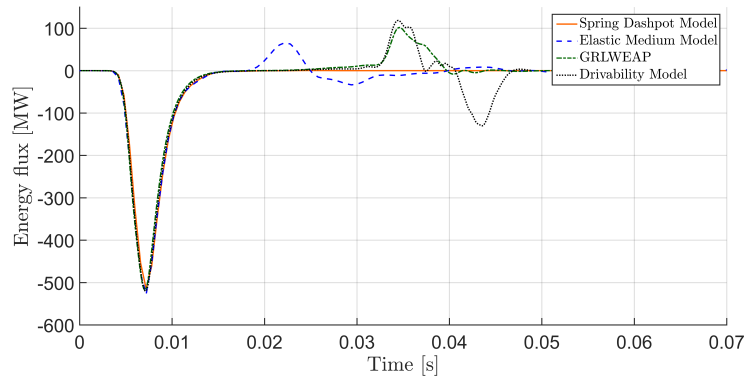


Figure 7.6: Energy flux at 8 m from the pile top after impact for all four models

7.2. Energy Comparison

Having analyzed the vertical velocity in the pile, the focus is now placed on the analysis of the energy level in the pile. To start with, in Figure 7.6, the energy flux per model is plotted at the same positions as before. The energy flux is calculated by the product of the vertical velocity and the force at that position. This indicates a corresponding force in the pile for the different models at the presented cross section. The Spring Dashpot model has no capability to extract the force per cross section in the pile. As a result, the here presented energy flux is the product of the vertical velocity and the inserted input force. Nevertheless, the difference in the force distribution between the input and after 8 m is negligible.

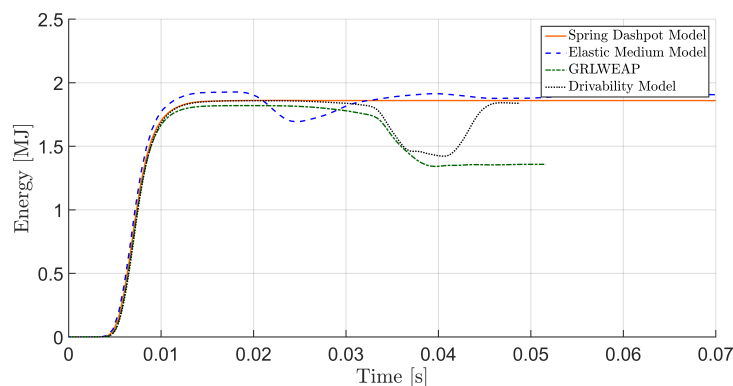


Figure 7.7: Cumulative energy at 8 m from the pile top after impact for all four models

Finally in Figure 7.7 the cumulative energy for all four models is shown. This shows the total amount of energy inserted into the system. All four models predict a similar energy input into the system. Only difference is in the reflected wave due to the different soil interaction. In general, it can be concluded that due to the

energy similarities, the force propagation through the pile is similar for the Elastic Medium model, GRLWEAP and the TU Delft drivability model.

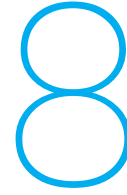
7.3. Conclusions

Four different models are used during this research. Two models for acoustic predictions, namely the Spring Dashpot model and the Elastic Medium model. Two models for drivability predictions, namely the GRLWEAP drivability program and the TU Delft drivability program. The vertical velocity propagation is the base of the final propagating pressure waves in both acoustic models. For the drivability models, the velocity in the shell determines the displacement of the pile with regard to the soil. By comparing the velocity in the shell for all four models, the similarity of the working principle of the models is justified. The results show a different vertical velocity propagation for the two acoustic models compared to the two drivability models.

Due to the long time duration of the impact force, a large amount of low frequency waves are excited. The acoustic models are solved in the frequency domain and account for frequency dissipation. At low frequency, the wavelength is long and the front of these waves has already been close to the soil layer just after impact. As a result the pile starts deforming together with the soil in the Spring Dashpot model. Furthermore, the soil material damping and spring stiffness are assumed constant throughout the frequency range. Consequently, the stiffness of the complete system and hence the vertical velocity from the initial moment in time is influenced. In the Elastic Medium model the soil is better represented by a three-dimensional description of the soil. The description of the soil is not influenced by the excited frequencies. Therefore, the vertical velocity in the pile is not influenced through the complete system from the initial moment in time. Consequently, the vertical velocity propagation in the Elastic Medium model and both drivability models are similar. Only the Spring Dashpot model has a strong deviation which is therefore further investigated.

To reduce the effect of the increased stiffness of the complete system in the Spring Dashpot model, the effect of the soil elasticity on the vertical velocity is examined. The results show a large influence of the soil elasticity and hence increase the uncertainty of selecting the correct parameters. By reducing the soil elasticity, the vertical velocity propagation in the pile is adjusted to an equal propagation path as the other three models. Consequently, a fair comparison between all four models is guaranteed. Furthermore, the energy levels are examined to satisfy the force distribution over the length of the pile for all four models. By taking the product of the vertical velocity and the force, the energy level was obtained. It is shown that for all four models the force distribution is equivalent.

A remarkable observation was done that revealed a similarity of the Spring Dashpot model and the TU Delft drivability model. For the Spring Dashpot model a large uncertainty is present in selecting the vertical spring stiffness. However the soil model of the drivability model does this more accurate. The model is also based on vertical springs and dashpots. Consequently, a comparison of the vertical spring stiffness is conducted. This revealed a similarity of the upper soil layer spring stiffness in the drivability model and the spring stiffness of the Spring Dashpot model over the complete penetration depth. This enables the prediction of soil conditions in the Spring Dashpot model with more certainty. Combining these two models into one acoustic and drivability model is recommended for further work.



Force Optimization

In the previous chapter all models that are developed and used during this thesis are discussed and evaluated. The different acoustic models and both drivability models have proven their differences and similarities with regard to soil interaction. Since for the acoustic models no sliding of the pile is taken into account and for the drivability models no noise propagation, chapter 7 is committed to prove their similarities. The present chapter brings all four models together into practice in order to investigate ways to reduce noise levels directly at the source during installation of large sized monopiles.

This is done by adjusting the excitation spectrum of the hammer force in such a way that the amplitude pressure spectrum in the fluid layer is reduced. This means a reduction of the amplitude pressure wave in the fluid layer, and hence by definition of the SEL, a reduction of the noise level. In order to achieve this goal, first a general introduction in the Fourier transformation and basic properties is presented in section 8.1. Thereafter in section 8.2 the method of adjusting the absolute excitation spectrum is introduced and described. This is subdivided into first describing the properties that the method has to meet. Thereafter a simple scaling and more acoustic optimized method are described. These methods enable to minimize the vibrations response of the whole system in the fluid layer, and finally reduce the noise level at 750 m from the pile. In section 8.3 the final adjustments to minimize the noise levels are made to the excitation spectrum and transformed to time domain. The transformation to time domain is needed to insert the adjusted impact diagram in the drivability model in section 8.4. When drivability is ensured, the obtained adjusted time trace is implemented in both acoustic models in section 8.5 and 8.6 to finally examine the noise propagation, soil interaction and noise levels.

8.1. Function Analysis

In order to determine how the force is optimized, it is of importance to fully understand the way the shape of the force in time domain correlates to the amplitude spectrum in the frequency domain. This is of importance since during transformation from frequency domain to time domain, the phase information must correctly taken into account. To find the correct correlation between time domain and frequency domain, first a more detailed background about the Fourier Transform is given.

8.1.1. Fourier Analysis

The Fourier Transform is a major cornerstone in the analysis and representation of signals in linear, time-invariant systems. Much of its usefulness stems directly from the property of the Fourier Transform which makes a transformation from time domain to the frequency domain and back possible and is defined as:

$$\begin{aligned} X(f) &= \int_{-\infty}^{\infty} x(t) e^{-i2\pi f t} dt \\ x(t) &= \int_{-\infty}^{\infty} X(f) e^{i2\pi f t} df \end{aligned} \tag{8.1}$$

In which the first one is the Forward Transform and the second the Inverse Transform and $x(t)$ represents the

time domain of the signal x and $X(f)$ the frequency domain of the signal x . The Fourier transform is valid for both periodic and non-periodic $x(t)$ that satisfy certain minimum conditions. All signals encountered in the real world easily satisfy these requirements.

The Discrete Fourier Transform

To compute the Fourier Transform digitally, a numerical integration is performed which results in an approximation to the true Fourier Transform called the Discrete Fourier Transform. There are three distinct difficulties with computing the Fourier Transform. First, the desired result is a continuous function. However, there will only be the possibility to calculate its value at discrete points. Second is that in order to evaluate the integral, use is made of the principal that this is the same as computing the area under a curve. This is done by the summation of the areas of narrow rectangles under the curve. The final problem is that even with this summation approximation to the integral, this results in a summation from minus infinity to plus infinity and subsequently in an "infinite" long calculation. Accordingly the transformation is done for a finite time interval that results in the Discrete Fourier Transform (DFT) definition:

$$X_k = \sum_{n=0}^{N-1} x_n e^{-i2\pi kn/N} \quad (8.2)$$

The Fast Fourier Transform

In order to compute the Discrete Fourier Transform, the Fast Fourier Transform (FFT) has been developed to eliminate the excessive amounts of computational time. This basically is an algorithm to compute the DFT with one extra assumption, namely that the number of samples N is even number. This allows certain symmetries to occur and hence reducing the number of calculations from N^2 towards $N \log(n)$ and consequently reducing computational time. Finally, resulting in a function that is an approximation of the desired Fourier Transform and only a transform of a finite time record of the input [Agilent Technologies; 2000].

8.1.2. Fourier transformation properties

The Fourier transformation decomposes any function into a sum of sinusoidal basic functions. Each of these basic functions is a complex exponential of a different frequency. As a result of that the Fourier Transform gives an unique way of viewing any function as the sum of simple sinusoidal functions. Using the definition of the Fourier Transform from equation 8.1, the integral is evaluated. The solution is a sinus function that changes amplitude over different frequencies:

$$\begin{aligned} X(f) &= \int_{-T/2}^{T/2} A e^{-i2\pi f t} dt \\ X(f) &= \frac{A}{-i2\pi f} \left[e^{-i2\pi f t} \right]_{-T/2}^{T/2} \\ X(f) &= \frac{A}{-i2\pi f} \left(e^{-i\pi f T} - e^{i\pi f T} \right) \\ X(f) &= \frac{AT}{\pi f T} \left(\frac{e^{i\pi f T} - e^{-i\pi f T}}{2i} \right) \\ X(f) &= \frac{AT}{\pi f T} \sin(\pi f T) \end{aligned} \quad (8.3)$$

This reveals that with increasing time duration a narrow and constrained frequency spectrum follows. Exactly the opposite takes place when decreasing the time duration where a more wider spectrum is obtained. This results in a conclusion that rapidly changing functions (short time duration), require more high frequencies content. Functions that move slower (longer time duration) will contain less high frequency waves and hence more low frequencies. The amplitude varies with different amplification factors A in time domain. This will only have an influence on the amplitude of the function, and no influence on the time period.

To be able to adjust an excitation spectrum in frequency domain, and thereafter transform in a mathematically correct way to time domain, the following basic Fourier transformations properties may be taken into account:

- Shift
- Linearity
- Scale
- Rayleigh Energy Theorem

Shift

There are two basic shift properties of the Fourier Transform.

1. Time Shift

$$x(t - t_0) = X(f) e^{-i2\pi f t_0} \quad (8.4)$$

2. Frequency Shift

$$x(t) e^{-i2\pi f_0 t} = X(f - f_0) \quad (8.5)$$

This shows there is the ability to shift the curve in the time and frequency domain. By extracting or adding a real valued number $x(t - t_0)$ to the time trace and the same for the frequency domain $X(f - f_0)$. Shifting a function in one domain corresponds to a multiplication by a complex exponential function in the other domain. This results from the distraction and can be further evaluated by substitution of $u = t - t_0$ and $du = dt$ into:

$$\begin{aligned} X(f) &= \int_{-\infty}^{\infty} x(t - t_0) e^{-i2\pi f t} dt \\ X(f) &= \int_{-\infty}^{\infty} x(u) e^{-i2\pi f (u + t_0)} du \\ X(f) &= e^{-i2\pi f t_0} \int_{-\infty}^{\infty} x(u) e^{-i2\pi f u} du \\ X(f) &= X(f) e^{-i2\pi f t_0} \end{aligned} \quad (8.6)$$

It can be noticed that due to a shift in time, the amplitude of the spectrum $X(f)$ remains the same and accordingly no change in the frequency content takes place. However, since the complex exponential function $e^{-i2\pi f t_0}$ always has a magnitude of 1, the time delay t_0 changes the phase of the function but not its magnitude. The time-shifting property identifies the fact that a linear displacement in time corresponds to a linear phase factor in the frequency domain.

Linearity

If two functions $x(t)$ and $g(t)$ are added, the Fourier Transform of the resulting function is simply the sum of the individual Fourier Transforms resulting into $X(f)$ and $G(f)$, respectively.

$$\begin{aligned} X(f) &= \int_{-\infty}^{\infty} (x(t) + g(t)) e^{-i2\pi f t} dt = \int_{-\infty}^{\infty} x(t) e^{-i2\pi f t} dt + \int_{-\infty}^{\infty} g(t) e^{-i2\pi f t} dt \\ X(f) &= X(f) + G(f) \end{aligned} \quad (8.7)$$

Due to the fact that the Fourier Transform is linear, this also results in the property of the case when k is any constant and multiplied with a function $x(t)$, then the Fourier Transform is also multiplied by the same constant.

$$\begin{aligned} X(f) &= \int_{-\infty}^{\infty} kx(t) dt \\ X(f) &= kX(f) \end{aligned} \quad (8.8)$$

Scale

A function can be scaled in frequency domain and time domain, keeping the phase information intact by:

1. Time scaling

$$x(at) = \frac{1}{|a|} X\left(\frac{f}{a}\right) \quad (8.9)$$

2. Frequency scaling

$$\frac{1}{|a|} x\left(\frac{t}{a}\right) = X(af) \quad (8.10)$$

A stretch in the time or frequency domain by a given factor a leads to a compression in the frequency or time domain by same factor a . There is also a corresponding amplitude change in the frequency domain. This is needed to keep the energies of the signals in both domains equal by the Rayleigh Energy Theorem.

Rayleigh Energy Theorem

Also referred as Parseval theorem usually refers to the result that the Fourier transform is unitary. Meaning that the integral of the square of a function is equal to the integral of the square of its transform.

$$\int_{-\infty}^{\infty} |x(t)|^2 dt = \int_{-\infty}^{\infty} |X(f)|^2 df \quad (8.11)$$

8.2. Method description

Now the basic properties of the Fourier transformation are known, the properties for the force optimization are discussed. This is of importance to clearly set the margins what the goal of using the Fourier transformation during this thesis is. As discussed earlier, the goal of this thesis is to reduce underwater noise during installation of offshore monopiles by adjusting the absolute excitation spectrum of the force. By assuming a constant transfer function of the complete system, the vibration response spectrum is manipulated and hence underwater noise is minimized. As a result, the minimization of the vibrations must be performed in the frequency domain, where the outcome (the optimized impact diagram) must be presented in time domain.

Adjusting the absolute excitation spectrum can be done in multiple ways, each having its own advantages and disadvantages. Most important is to bear in mind that the adjustments must be performed in the frequency domain to gain an optimal process and when transforming to time domain, phasing must be correctly taken into account. As a consequence the method of applying any obtained absolute excitation spectrum, without real and imaginary parts, to the inverse Fourier Transformation is not adequate by means of incorrect phase information that into account. Vice versa, by applying the Fourier Transformation in order to obtain any desired frequency spectrum from time domain is a sub-optimal process that is not desirable. Hence another method had to be conducted that fits the requirements of adjusting the frequency domain and taking account of phase information during transformation towards time domain.

In order to do so, a few basic properties are chosen to account for as stated below. Each of the three conditions is thereafter discussed.

1. Adjust impact diagram by adjusting absolute excitation spectrum.
2. Excitation spectrum must contain energy at zero frequency
3. The impact diagram must be realistic

The first condition is of importance to obtain an optimal method of adjusting the absolute excitation amplitude spectrum. Taking this as base case, a method in order to take phasing into account when going from frequency domain into time domain must be obtained. As a result it is of importance to first look into what phase is and what it means. The Fourier transform of a function of time itself is a complex-valued function of frequency. Consisting of a real and an imaginary part. The absolute value of this complex-valued function represents the amount of that frequency present in the original function, and the complex argument $\arctan = \frac{Im}{Re}$ is the phase offset of the basic sinusoidal in that frequency. Knowing consequently the real and imaginary part is of importance in taking account of the phase. However, the absolute excitation spectrum on itself, the magnitude of the function, is generated by the square root of the squared real and squared imaginary part. As a result, when transforming the gained absolute excitation spectrum to time domain, the real and imaginary parts are unknown and consequently phasing is not taken into account. Normally in this case, a random phase is chosen for every frequency in order to take account for the phasing. By applying different random phases and then by means of Fourier transformation from time domain to frequency domain, a realistic time trace can be obtained. However, here a large amount of frequencies are taken into account and hence the chance of obtaining a realistic time trace in this way is rather unrealistic and consequently even

more sub-optimal.

The second property states that the absolute excitation spectrum must contain energy at zero frequency. When this is not the case, so when $X(0) = 0$, this results in:

$$\begin{aligned} X(f) &= \int_{-\infty}^{\infty} x(t)e^{-i2\pi ft} dt \\ X(0) &= \int_{-\infty}^{\infty} x(t)1 dt \\ X(0) &= 0 \end{aligned} \tag{8.12}$$

Subsequently $x(t) = 0$ to satisfy this condition. The Fourier transformation is actually the same as the summation of the area of the time trace multiplied with $e^{-i2\pi ft}$ as shown in equation 8.1. As a result, when transforming the function with $X(0) = 0$ to the time domain, this means that summation of the time trace around the time axis must be zero. Subsequently, the time trace must contain positive and negative force values. This is in contradiction with the property. In the case of do applying energy at zero frequency, by example $X(0) = 1$, this results in $x(t) = 1$. Which means on its turn that the time trace will vary around the value of 1, but can still be positive and realistic. Hence, it can be concluded that the function must always contain energy at zero frequency, resulting in a realistic and positive time trace.

The third and last property is in order to satisfy a realistic impact diagram. This means the adjusted impact force must be able to obtain in reality, and favorably by an impact hammer. This is due to its large amount of settings that can be adjusted.

8.2.1. Simple Scaling Approach

With the three properties as stated above, the approach of adjusting the excitation spectrum can be described. Since taking correct account of the phase information while transforming from frequency to time domain is of importance, the here adopted method remains its phase information while adjusting. It uses the real and imaginary values of an actual time trace on an impact hammer. By property three, the real function is symmetric and the imaginary function is anti-symmetric as shown in Figure 8.1. The time trace that is shown here is that of the IHC S-4000 obtained from GRLWEAP.

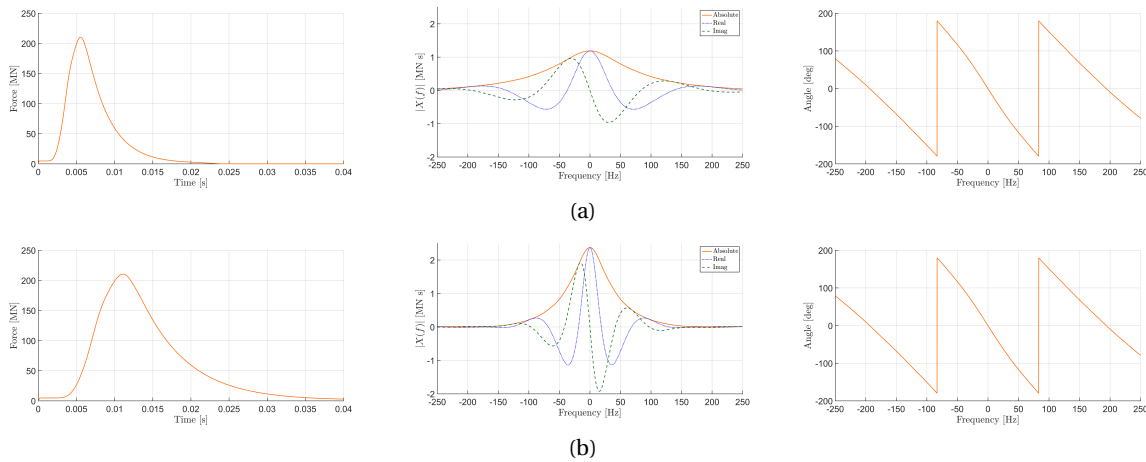


Figure 8.1: Simple scaling approach of the time trace, excitation spectrum and phase distribution for (a) before applying (b) after applying

By means of equation 8.9 and 8.10, scaling is applied to the original excitation spectrum. This makes it possible to adjust the frequency band width to any desired range in order to evade dominant acoustic frequencies. Here, a dominant acoustic frequency serves as reference point till were the excitation spectrum band width reaches. Figure 8.1 illustrates the process of the simple scaling approach on the IHC S-4000 excitation spectrum. The top figures illustrate the time trace, excitation spectrum and phase distribution before applying and the lower figures after applying the simple scaling approach. By scaling with a factor of 2, the band width of the excitation spectrum decreases and the amplitude increases. Consequently, the time duration of the

impact force is enlarged with a factor of 2, while keeping the phasing unimpaired.

8.2.2. Acoustic Optimization Approach

The simple scaling approach as described above has the disadvantage that it can only excite frequencies below a selected dominant frequency within the transfer function. Removing energy at different frequencies is subsequently not possible and the main energy is located in the very low frequency band width. In order to overcome this limitation, a more acoustic optimization approach has been adopted. This method uses the same principal as the simple scaling approach where the original impact diagram of an impact hammer is used as a base. By scaling this function, the main pulse can be adjusted to whatever frequency band width of interest. The band width of the excitation spectrum of the acoustic optimization approach is wider than the simple scaling approach in order to not excite important frequencies.

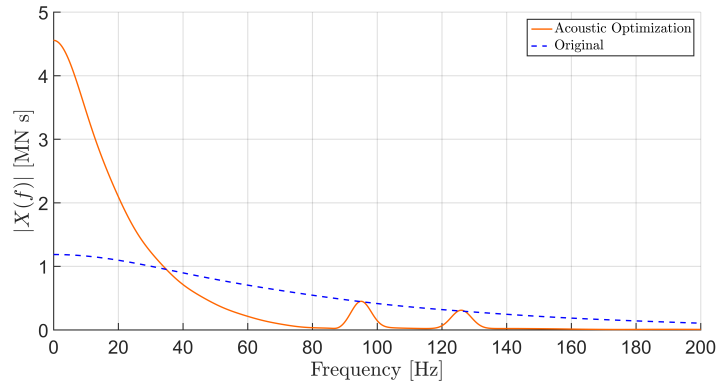


Figure 8.2: Absolute excitation spectrum of original impact diagram and from both adjusted impact diagrams

Figure 8.2 illustrates this method in which the dotted curve is the original absolute excitation spectrum of an impact hammer which covers a broad spectrum of frequencies. By scaling towards a lower frequency band width excited by the hammer, energy is removed from certain dominant acoustic frequencies. Areas where no energy has been removed due to the absence of dominant acoustic frequencies, energy is added by means of an exponential function. Its Fourier transformation is a well known one, namely: [Brigham; 2005]

$$\begin{aligned} x(t) &= \left(\frac{\alpha}{\pi}\right)^{0.5} e^{-\alpha t^2} \\ X(f) &= e^{-\frac{\pi^2 f^2}{\alpha}} \end{aligned} \quad (8.13)$$

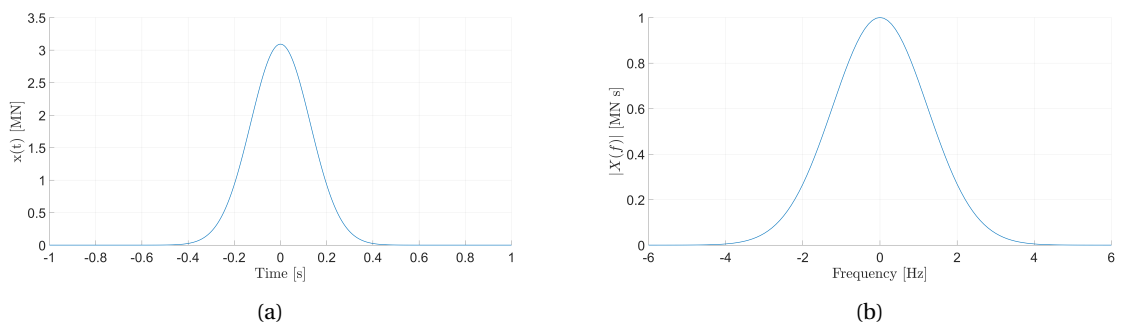


Figure 8.3: Exponential function in (a) time domain and (b) frequency domain

And illustrated by figure 8.3a in time domain and 8.3b in frequency domain. The main advantage of this function is that due to the properties of the exponent, the phase influence is lost during transforming from frequency domain to time domain and vice versa. When multiplying the function with the Fourier exponent $e^{-i2\pi ft}$ the following occurs:

$$\begin{aligned}
x(t) &= \left(\frac{\alpha}{\pi}\right)^{0.5} e^{-\alpha t^2} \\
X(f) &= \left(\frac{\alpha}{\pi}\right)^{0.5} \int_{-\infty}^{\infty} e^{-\alpha t^2} e^{-i2\pi ft} dt \\
X(f) &= \left(\frac{\alpha}{\pi}\right)^{0.5} \left(\int_{-\infty}^{\infty} e^{-\alpha t^2} \cos(2\pi ft) dt - i \int_{-\infty}^{\infty} e^{-\alpha t^2} \sin(2\pi ft) dt \right) \\
X(f) &= \left(\frac{\alpha}{\pi}\right)^{0.5} \int_{-\infty}^{\infty} e^{-\alpha t^2} \cos(2\pi ft) dt \\
X(f) &= \left(\frac{\alpha}{\pi}\right)^{0.5} \int_{-\infty}^{\infty} e^{-\alpha t^2} \left(\frac{e^{i2\pi ft} + e^{-i2\pi ft}}{2} \right) dt \\
X(f) &= e^{-\frac{\pi^2 f^2}{\alpha}}
\end{aligned} \tag{8.14}$$

Accordingly no phase information is needed and the function in frequency domain can simply be added on top of the scaled function obtained by the method described in section 8.2.1. Thereafter, all properties as stated in section 8.2 are still fulfilled and hence adjusting the absolute excitation spectrum can start.

8.3. Adjusted Absolute Excitation Spectrum

In order to find an impact diagram which finally reduces the SEL at 750 m, it is of importance that the applied adjustments to the corresponding frequency spectrum result in a fit with the regions that correspond with less response in the transfer function of the system. Since by assuming that the absolute excitation spectrum squared $|\frac{r}{\zeta}(\omega)|^2$ times the transfer function of the system $S(\omega)$ is the vibration response spectrum $S_r(\omega)$, and a reduction of the vibration response spectrum result in a lower SEL, the fit of the absolute excitation spectrum to the transfer function is of importance.

$$S_r(\omega) = \left| \frac{r}{\zeta}(\omega) \right|^2 S(\omega) \tag{8.15}$$

Bear in mind that during determining of the impact diagrams, no hammer-pile dynamics are being considered. This is a different scope and for this reason not considered here. Three types of impact diagrams are considered during this thesis, namely: 1) A typical Impact hammer impact diagram, 2) BLUE Piling impact diagram and 3) Adjusted impact diagram by adjusting the absolute excitation spectrum.

As discussed in 2.2.3, BLUE Piling is a new technique in pile driving using falling water to create the energy needed to drive the pile into the soil. In order to create this falling water, an internal combustion with LNG is created which blows the water up. Since creating the energy source is part of the whole blow cycle, one blow takes significant time. Namely around 2 seconds including the combustion, falling water and wave traveling back through the pile as shown in Figure 3.4 which is obtained from GRLWEAP.

However, both Acoustic Models are not able due to computational reasons to analyze such a large time periods. As a result, the main peak due to the falling water is considered as main noise source. Since this one has the highest amplitude it will have the most influence on the SEL. Thereby taking into account that this blow takes place about 0.5 sec after the previous, smaller in amplitude blow. Hence the created pressure waves by the previous blow will not be caught up by the next blow. Accordingly it can be assumed that they will not have a cumulative effect and thus can be analyzed separately. Figure 8.4 illustrates the time trace and corresponding absolute excitation spectrum for both hammers.

Something what immediately becomes clear is the significant difference in time duration between the two hammers. While for the IHC S-4000 a time duration of one pulse is approximately 0.02 sec, the BLUE 25M approximately takes 0.2 sec. An increase of 10 times, which is huge difference. Enlargement of the duration of the pulse is related to a decrease of the frequency band width. As a result, the BLUE 25M has an extremely low frequency band range to be excited.

The impact diagrams for the IHC S-4000 and the BLUE 25M have been obtained in chapter 3 and analyzed and discussed in chapter 4 and 5. The remaining last impact diagram, the adjusted impact diagram by adjusting the absolute excitation spectrum is discussed in the present chapter. The method to do so has been described in section 8.2.2 and will here be implemented in order to obtain an absolute excitation spectrum

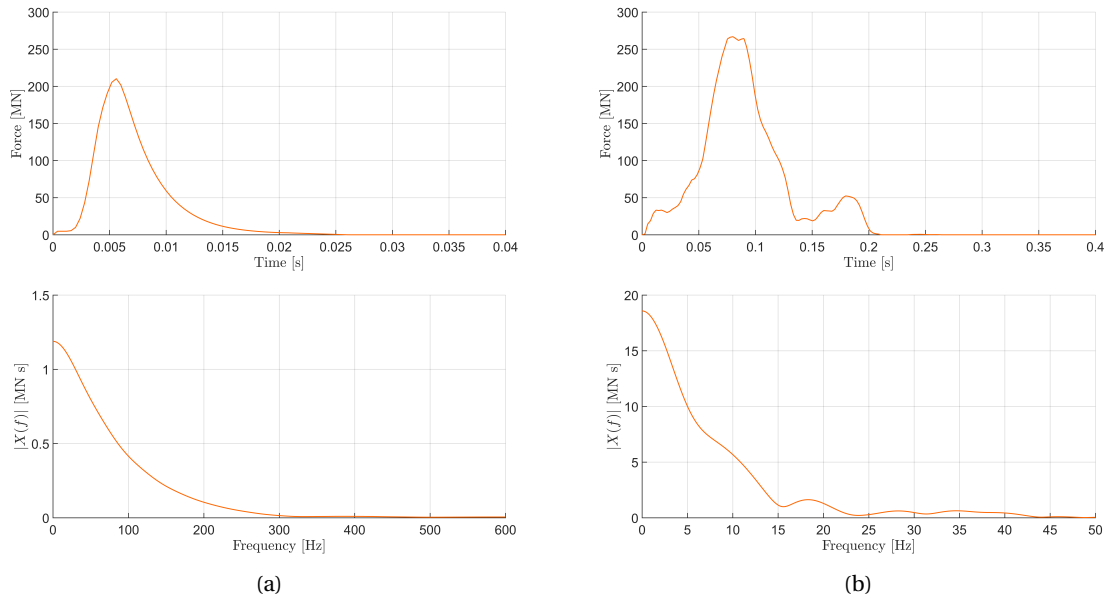


Figure 8.4: Impact diagram and absolute excitation spectrum of (a) Impact hammer IHC S-4000 with 1800kJ and (b) BLUE Piling hammer BLUE 25M with 31000 kJ

that reduces the acoustic response after excitation.

The first step is to match the absolute excitation spectrum with the transfer function of the system to evaluate dominant acoustic frequencies within the frequency range to be excited by the force. Consequently the transfer function of the system must be obtained first. By evaluating equation 8.15, and imagining a constant absolute excitation spectrum of 1, the vibration response spectrum would be similar to the transfer function of the system $S_r(\omega) = S(\omega)$. This results in all frequencies to be evenly excited. Adopting this approach, both acoustic models possess a function where the applied force is a fictive constant force in the frequency domain of 1 MN s, to obtain the transfer function. This results in a transfer function of the fluid layer for both models as shown in Figure 8.5.

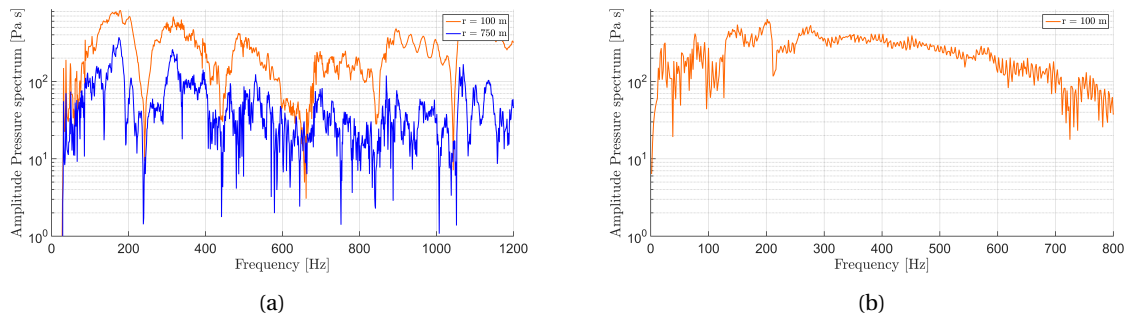


Figure 8.5: Transfer function of fluid layer obtained from (a) Spring Dashpot Model at 100 and 750 m from the pile and (b) Elastic Medium Model at 100 m from the pile. Both 2 m above seabed

When comparing both, insight is created into the area where most of the energy is transmitted and lost. Conversely this gives information which frequencies are naturally damped and which are not (or less). From figure 8.5 it can be noticed that frequencies above 500 Hz tend to have a lower response than the lower frequencies. However, a frequency of 500 Hz corresponds to a time duration of $\frac{1}{500} = 0.002$ sec. This is so short, that it would not be feasible to achieve in reality for very large hammers and is thus not further considered. As a result, the lower frequencies are more of interest and hence zoomed into in Figure 8.6. Basically, the radial acceleration of the pile results into pressure waves in the fluid layer. But not all of these motions contain

enough energy to propagate far in distance due to material and geometrical dissipation. The decay in amplitude pressure spectrum for frequencies till 300 Hz are visible in Figure 8.6. Frequencies that are naturally already enough damped out at 750 m from the pile, are of interest to excited with more energy than others. Others should be avoided by removing the energy at those frequencies. Consequently, the absolute excitation spectrum must fit the transfer function resulting in a reduction of the vibration response spectrum. To do so, three steps are taken into account:

1. Obtain dominant acoustic frequencies
2. Remove energy from excitation spectrum at dominant acoustic frequencies
3. Obtain corresponding time trace

The here enumerated steps are described in the coming subsections.

8.3.1. Dominant acoustic frequencies

In this subsection, the process of obtaining the dominant acoustic frequencies of the transfer function is described. The dominant frequencies that have a high acoustic response, must be obtained in order to be able to adjust the excitation spectrum. Reducing the response at these frequencies has influence on the final vibration response spectrum.

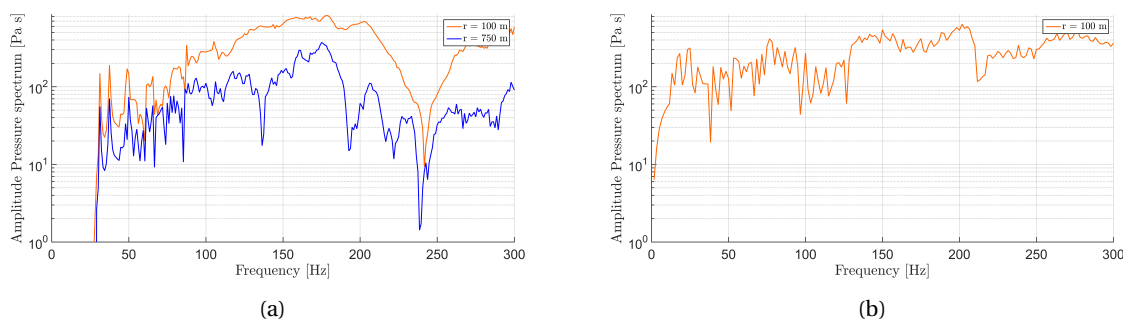


Figure 8.6: Transfer function of fluid layer obtained from (a) Spring Dashpot Model at 100 and 750 m from the pile and (b) Elastic Medium Model at 100 m from the pile. Both 2 m above seabed.

As illustrated in Figure 8.6, the relative peaks correspond to the modes and eigen frequencies of the pile as also summarized in Table 8.1. From here it can be concluded there is a large amount of eigen frequencies around 200 Hz. This is logic due to the influence of the ring frequency of the pile at 220 Hz. However, since everything is excited with the same amount of energy in the frequency domain, the relative influence of each eigen frequency on the final amplitude pressure spectrum is not so evident. The relative difference becomes better distinguished after exciting with the original IHC S-4000 impact diagram due to the energy distribution within the amplitude excitation spectrum of the force. The amplitude pressure spectrum of the validation case is shown in Figure 8.7 for both models.

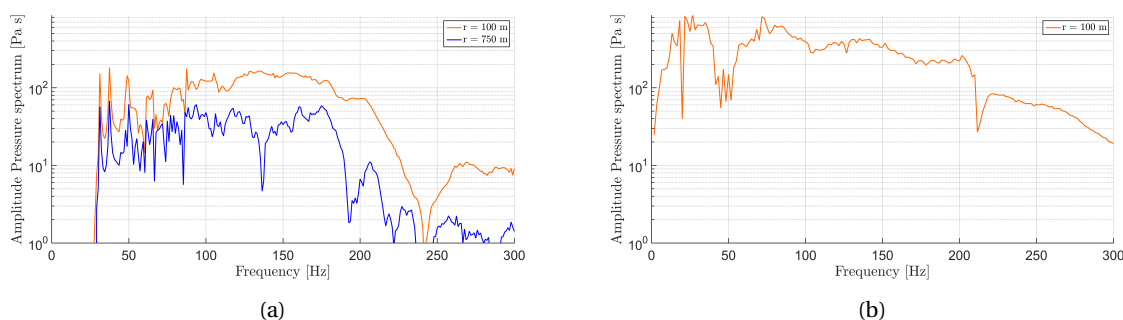


Figure 8.7: Amplitude pressure spectrum of the fluid layer after excitation with the IHC S-4000 from (a) Spring Dashpot Model at 100 and 750 m from the pile and (b) Elastic Medium Model at 100 m from the pile. Both 2 m above seabed.

From Table 8.1, some of the eigen frequencies from the first and second circumferential modes are clearly visible in Figure 8.7. From the result of the Spring Dashpot model, three peaks in the low frequency region are visible. These refer to 31, 38 and 48 Hz. The first eigenfrequency corresponds to the first wavenumber of the radial propagating wave caused by the axial deformation in the second circumferential mode. The third eigenfrequency of 48 Hz correlates to the second eigenfrequency of the first circumferential mode. The first eigenfrequency of the first circumferential mode, 16 Hz, is below the cut-off frequency and as a result does not propagate in the waveguide.

Removing energy in the excitation spectrum at these frequencies in order to minimize underwater noise is highly favorable. Notice the large areas between the lower 1 till 5 modes of the first circumferential mode and the first two modes of the second circumferential mode. These are also visible in the illustrated transfer functions. This means there is a region with low acoustic response. Subsequently, it is of interest to select a region to excite with the excitation spectrum which is in the band width below the cut-off frequency of the propagating modes. Due to the depth of the fluid layer, there will be a cut-off frequency, and noise energy with a lower frequency will be affected by the waveguide. The relationship between the modes and cut-off frequencies is given by: [Jensen et al.; 2011]

$$f_0 = \frac{(m - 0.5)c_w}{2D\sqrt{1 - \left(\frac{c_w}{c_b}\right)^2}} \quad (8.16)$$

Consequently the first mode for N=0 corresponds to a cut of frequency of 26 Hz as earlier stated. The second mode corresponds to 78 Hz. As a result, exciting below the cut-off frequency of that mode, will result in less wave propagation into the far field through the fluid layer. As the waves are not reflected when hitting the seabed and hence can not propagate through the waveguide. This effect is less visible in Figure 8.7 for the Spring Dashpot model. Due to the fact that there is no propagating wave in the soil layer in this model, no difference in cut-off frequencies is taken into account. Resulting in all modes to propagate into the far field.

Table 8.1: Eigen frequencies of first (N=0) and second (N=1) circumferential mode

Mode	1	2	3	4	5	6	7	8	9
Eigen frequency N = 0	16.2	48.4	80.3	111.5	141.2	167.3	186.3	196.9	202.1
Eigen frequency N = 1	31.5	114	231.4	362	490.4	607.3	709.4	796.2	869.2
Mode	10	11	12	13	14	15	16	17	18
Eigen frequency N = 0	204.9	206.5	207.5	208.2	208.8	209.1	209.5	209.7	209.9
Eigen frequency N = 1	930.2	981.1	1023.8	1059.8	1090.2	1116.1	1138.3	1157.4	1174.1

8.3.2. Remove energy from excitation spectrum

With the method as described in section 8.2.1 and 8.2.2 and having discussed the requirements in the frequency domain, the adjusted excitation spectrum can be obtained. This is done with the simple scaling and the acoustic optimization method.

First the main range of the energy in the excitation spectrum is determined. By means of the cut-off frequency per propagating mode from equation 8.16, the range of 78 Hz has been selected for the main pulse. This means that the noise energy with a lower frequency will be affected by the waveguide, and propagates into the soil layer. The main pulse in the excitation spectrum will excite frequencies till the third mode of the first circumferential mode. As a result, a lot of energy is then excited in frequencies below the cut-off frequencies of the second propagating mode and hence not propagating through the fluid. In the excitation spectrum, mode 4 and 5 of the first circumferential mode must be avoided to reduce acoustic response. In the regions between the modes, the energy can maintain. This results in two absolute excitation spectrum's as shown in Figure 8.8 for the simple scaling approach and the acoustic optimization approach.

Even though this is beyond the scope of this thesis the here presented absolute excitation spectrum's are based on a real impact hammer and should correspond to an impact diagram in time domain that is mechanically possible.

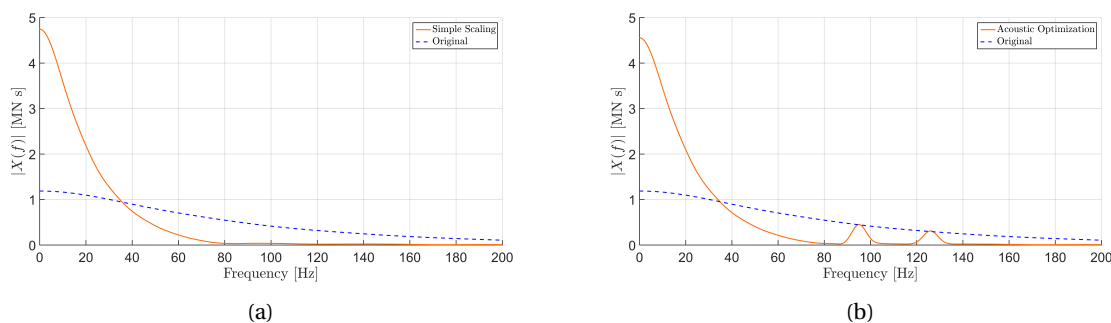


Figure 8.8: Adjusted Absolute Excitation spectrum with (a) simple scaling approach and (b) acoustic optimization approach

8.3.3. Obtain Time Trace

In order to implement the adjusted absolute excitation spectrum into the drivability model and both Acoustic Models the time trace must be obtained. According to the same method as described in section 8.2.1 and 8.2.2, this is done for the two adjusted excitation spectrum's as described in the previous section. By means of the inverse Fourier transformation it is possible to obtain the function in Time domain as shown in figure 8.9.

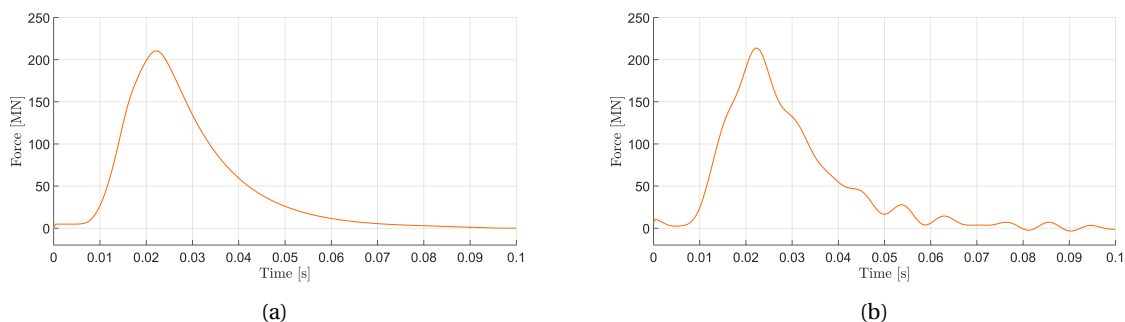


Figure 8.9: Time trace of adjusted absolute excitation spectrum with (a) simple scaling approach and (b) acoustic optimization approach

For the simple scaling approach this results in a relative normal impact hammer time trace, only with a longer duration. For the acoustic optimization approach, the obtained time trace looks not so different from the original as well. This is due the relative small amplitude of the added energy regions. In the case they would be set to a larger amplitude value, the sinusoidal function due to the addition of the exponential function, would result in a larger amplitude in time domain. Also notice the fact that the peak force level has remained constant for all transformations in time domain. This is done by applying the Rayleigh theorem that corrects for the extra added energy in order to achieve a fair comparison between the different time traces. This affects the noise predictions as well as the drivability predictions.

8.4. Drivability Analysis

In order to assess the drivability of the adjusted absolute excitation spectrum's, the spectrum's are implemented in the own constructed drivability model. By inserting the impact diagram and soil conditions of the specific area, an estimate of the displacement at that location can be obtained. This is also the way how to compare different impact diagrams with each other. Meaning that in the case an impact diagram results into zero displacement, the applied force is insufficient and the results of the acoustic models are irrelevant. Only when the force is sufficient to penetrate the pile into the soil, the results from the acoustic models can be compared with each other.

One must place a special remark to this drivability analysis in advance. Due to the enlargement of the impact diagram, the dynamics in the pile decrease as it is velocity depended. As a result the settling time of the soil increases and less displacement occurs. This affect is not taken into account during this research. Here the standard method, based on GRLWEAP, for the industry is applied. on top of that, the enlargement of the pile

dimensions tend to increase the affect of the shaft resistances compare to the tip resistance. With smaller piles the shaft resistance is less than the tip resistance. Due to the increased pile surface area, the shaft resistances increases and should be taken into account bu the drivability model by radial springs and dashpots. Again, for a fair comparison between GRLWEAP and the drivability model, this is not included.

Figure 8.10 shows the drivability analysis of both the simple scaling as acoustic optimized impact diagram. The drivability analysis is performed in stage 3, so final penetration. Here the soil resistance is at its maximum. If the impact force is able to overcome the resistance here, it must be able to overcome the resistance force in less high layers as well.

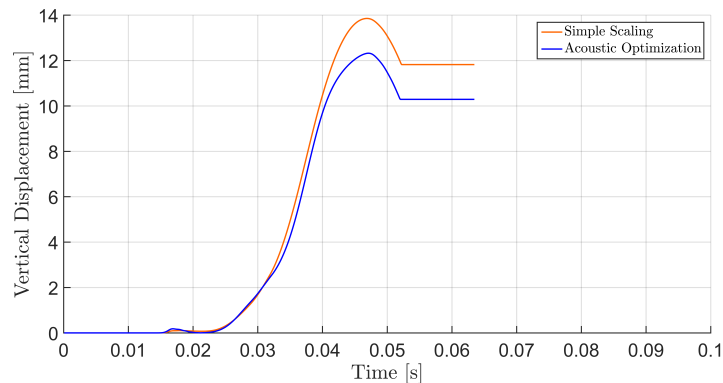


Figure 8.10: Tip displacement after impact with simple scaling and acoustic optimized impact diagrams

It can be noticed that their is sufficient vertical displacement with both impact diagrams. In the final stage of penetration, the original impact diagram needs an average of 98 blows/25 cm. The simple scaling and acoustic optimized impact diagram need, 21 and 24 blows/25 cm, respectively. As a result, noise predictions with the acoustic models can be conducted in the next sections.

8.5. Noise predictions with Spring Dashpot Model

In this section the result of adjusting the absolute excitation spectrum with regard to the acoustics is discussed. In previous section it is proven that with a comparable model as GRLWEAP, which is the industry standard in terms of drivability analysis, both adjusted impact diagrams show sufficient vertical displacement. This ensures their ability to drive a pile into the soil.

The noise predictions are performed with both acoustic models in order to get also the correct potency of the soil interaction and hence the secondary noise path. First the results from the Spring Dashpot are discussed in the present section. The Spring Dashpot model is a rather quick and easy to configure model to examine the propagation of the underwater pressure waves and the final noise levels during piling. The input settings of the model are exactly the same as used in previous analysis as described in section 3.3. The only difference is the input force. These are now the impact diagrams as presented in Figure 8.9.

8.5.1. Response during pile driving in frequency domain

Figure 8.11 shows the frequency spectrum for the three impact diagrams evaluated at 750 m from the pile in the third octave band. As can be noticed, the shift of energy in the absolute excitation spectrum follows by a reduction of the pressure amplitude in the frequency regions where less energy is applied. For the simple scaling and acoustic optimized impact diagram, most of the energy is delivered below 80 Hz. This affect becomes more clear when analyzing the near field after 50 m wave propagation as shown by Figure 8.11a. Here it can be observed that below 40 Hz, which is the point where the amount of energy in the adjusted impact diagrams exceeds the original impact diagram, the response in pressure levels is higher for the adjusted impact diagrams. With a difference of around 5 dB at 20 Hz, which corresponds to around 1.7 times higher amplitude pressure wave. However these waves, due to the cut-off frequency of 26 Hz, are not capable of traveling trough

the fluid layer and will naturally damp out. Consequently at 750 m they are not visible any more.

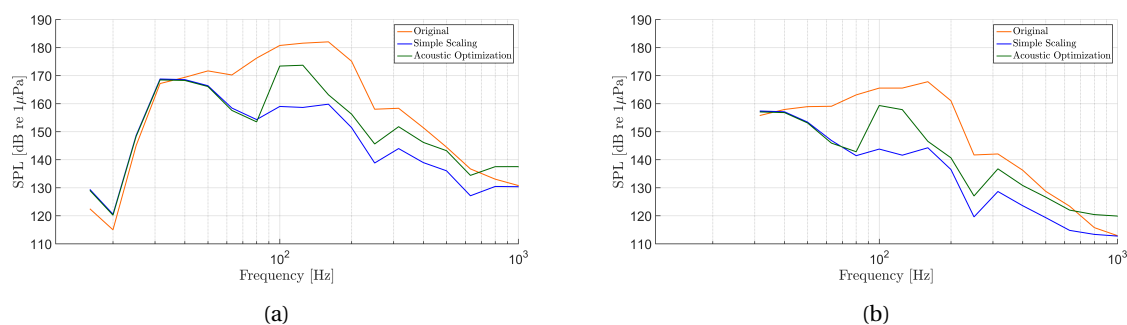


Figure 8.11: Frequency spectrum after excitation with the original impact diagram, simple scaling impact diagram and acoustic optimized impact diagram at (a) $r = 50$ m and (b) $r = 750$ m from the pile and 2 m above the seabed

The peak around 100 till 125 Hz is caused by the added energy in the absolute excitation spectrum. Due to the conversion towards the third octave band, energy is collected within a bandwidth. At 100 Hz the bandwidth is from 90 till 112 Hz and at 125 Hz this is between 113 and 140 Hz. As a consequence both added energy zones are collected within both bandwidths together with the 110-115 Hz region to be avoided. Figure 8.12 shows the amplitude pressure response of the original, simple scaling and acoustic optimized impact diagram. This time not in the third octave band. Here the influence of the added energy is more clearly visible between 90 and 130 Hz. on top of that, the region in which the excitation spectrum should excite the system less is also clearly visible between 110 and 115 Hz.

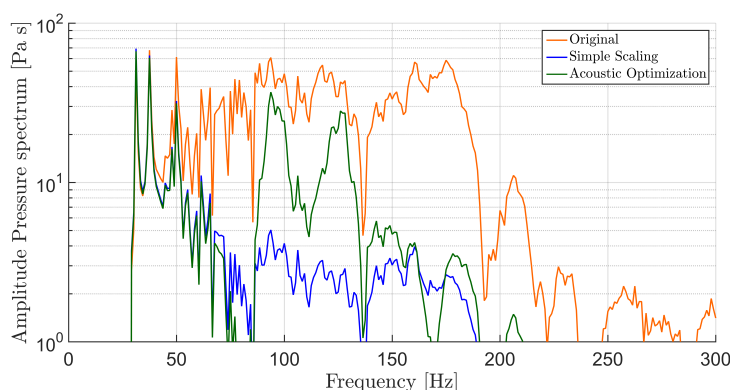


Figure 8.12: Amplitude pressure spectrum after excitation with the original impact diagram, simple scaling impact diagram and the acoustic optimized impact diagram. Response at 2 m above the seabed and 750 m from the pile

8.5.2. Response during pile driving in time domain

Figure 8.13 presents the pressure field propagation from the original impact diagram. This shows a clear propagation of the pressure field along increasing radial distances. High pressure amplitude of around 52 kPa are observed in the near field (50 m), where with a decay of 90% this reduces to about 5 kPa at 750 m. For the acoustic optimized impact diagram, mainly due to the enlargement of the time duration, the pressure amplitude has a completely different shape as illustrated in Figure 8.14. The pressure waves have a longer duration than the original and the amplitude has decreased. In the near field at 50 m, a maximum pressure amplitude of 9.2 kPa is observed. This is a reduction of 82% with the original maximum pressure amplitude in the near field. The decay of the pressure amplitude to the 750 m region is similar with 84% due to the attenuation of the fluid layer.

Finally, the reduction in pressure amplitude is related to the noise levels. A reduction of the pressure amplitude will not automatically reduce the noise levels by its definition, but will affect a reduction of the peak

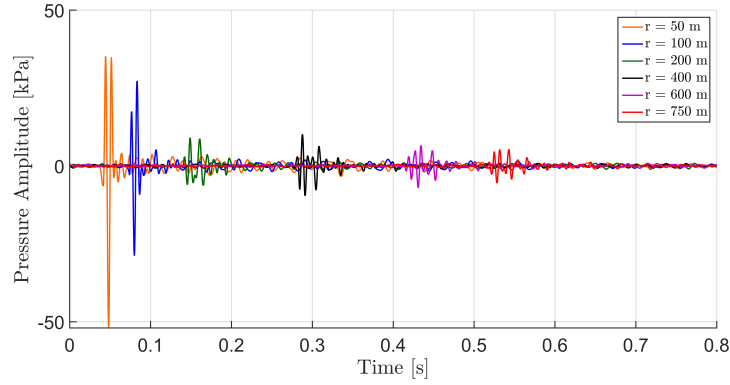


Figure 8.13: Pressure amplitude propagation of original impact diagram at 2 m above seabed

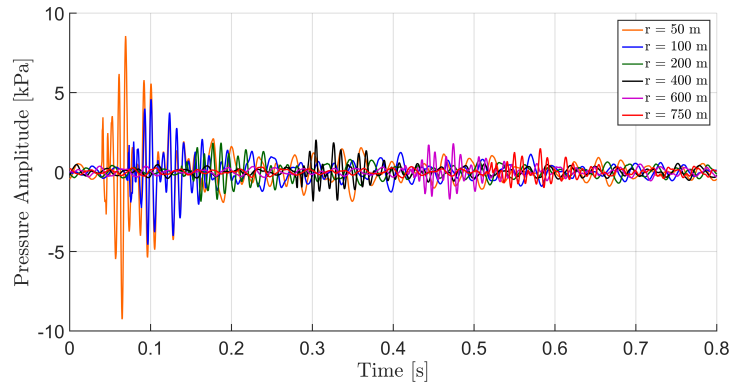


Figure 8.14: Pressure amplitude propagation of acoustic optimized impact diagram at 2 m above seabed

Table 8.2: Noise levels after excitation with adjusted impact diagrams

Approach	Category	Distance m	Model Original dB re $1\mu Pa^2 s$	Model Adjusted dB re $1\mu Pa^2 s$	$\Delta SEL_{05} / \Delta L_{peak}$
Simple Scaling	SEL_{05}	750	175.2	163.9	-11.3
	L_{peak}	750	194.8	174.6	-20.2
Acoustic Optimization	SEL_{05}	750	175.2	166.8	-8.4
	L_{peak}	750	194.8	183.4	-11.4

level. Table 8.3 summarizes the SEL_{05} and L_{peak} at 750 m from the pile for the simple scaling and acoustic optimized impact diagram. With a reduction in pressure amplitude of around 82 %, the peak level decreases drastically. Remarkable to notice is the relation between the slope of the impact diagram and the final noise levels. The slope angle of the original impact diagram to the horizontal is around 500%, resulting in a L_{peak} of 194.8 dB re $1\mu Pa^2 s$. The slope angle of the simple scaling impact diagram is around 278 % with a peak level of 174.8 dB re $1\mu Pa^2 s$. This means a reduction of around 20 dB with a decreased slope angle of 44 %.

8.6. Noise predictions with Elastic Medium Model

Having analyzed the response with the Spring Dashpot model, the focus is now placed on analyzing the response of the Elastic Medium model. The Elastic Medium model is much more sophisticated, but still straightforward to configure. Unlike the Spring Dashpot model, the soil is modeled as a visco-elastic medium to encounter shear stresses and accordingly be able to predict the noise levels during pile driving more accurately.

8.6.1. Response during pile driving in frequency domain

In Figure 8.15 the amplitude pressure spectrum in the fluid layer is shown for the acoustic optimized impact diagram at two vertical distances from the seabed and 100 m from the pile. As can be seen, the response is similar for $f > 80$ Hz. Only the amplitude varies due to the lower soil interaction at further vertical distance from the seabed. Below 80 Hz the differences in pressure amplitude at both vertical distances are larger due to the influence of the soil. To examine further the effect of the acoustic optimized impact diagram on the system compared to the original impact diagram, Figure 8.16 shows the relative differences at $h = 2$ m and $h = 12$ m from the seabed and 100 m from the pile. A significant reduction of amplitude in the higher frequencies can be noticed due to the shift in energy in the impact diagram. This remains when moving up the fluid layer to $h = 12$ m. Both energy bumps around 95 and 125 Hz are clearly visible in comparison to the simple scaling impact diagram. They are positioned in the regions where for the original amplitude response less excitation was noticed, combined with the eigen frequencies of the system for both accounted circumferential modes.

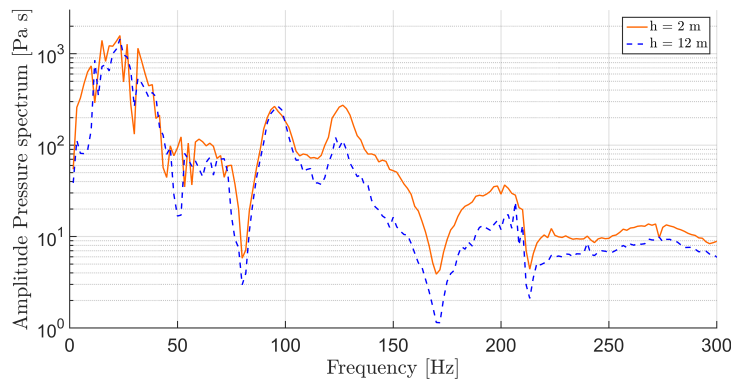


Figure 8.15: Amplitude pressure spectrum after excitation with the acoustic optimized impact diagram at $h = 2$ m and $h = 12$ m from the seabed and 100 m from the pile

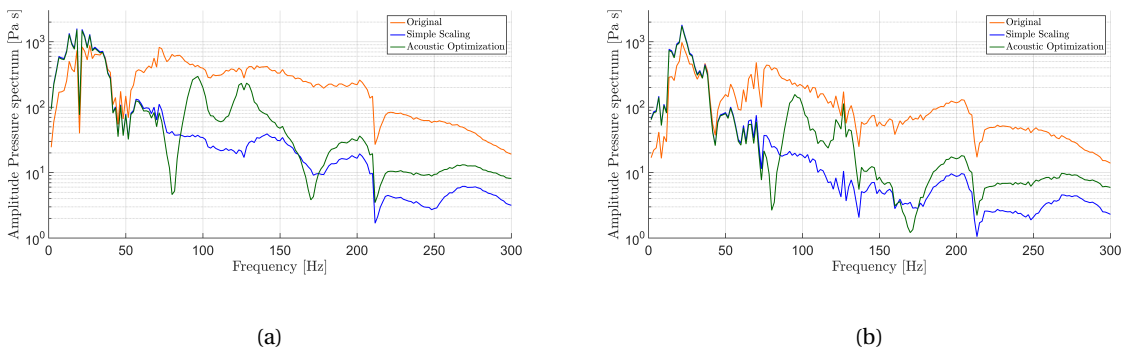


Figure 8.16: Amplitude pressure spectrum after excitation with the original impact diagram, simple scaling impact diagram and the acoustic optimized impact diagram at (a) $h = 2$ m and (b) $h = 12$ m from the seabed and 100 m from the pile

Finally in Figure 8.17, the frequency response spectrum after excitation with the original, simple scaling and acoustic optimized impact diagram is given in the third octave band. This enables to compare mutually the outcome with earlier presented frequency spectrum's. A relative large low frequency response can be noticed. This is due to the high amount of energy applied in the low frequency region. Also, due to the large wavelength of the low frequency waves, the waves are still within one wavelength distance from the pile. As a consequence no attenuation of the wave has yet taken place resulting in a relative high response. Since the high response region is below the cut-off frequency, the wave will not propagate further through the waveguide.

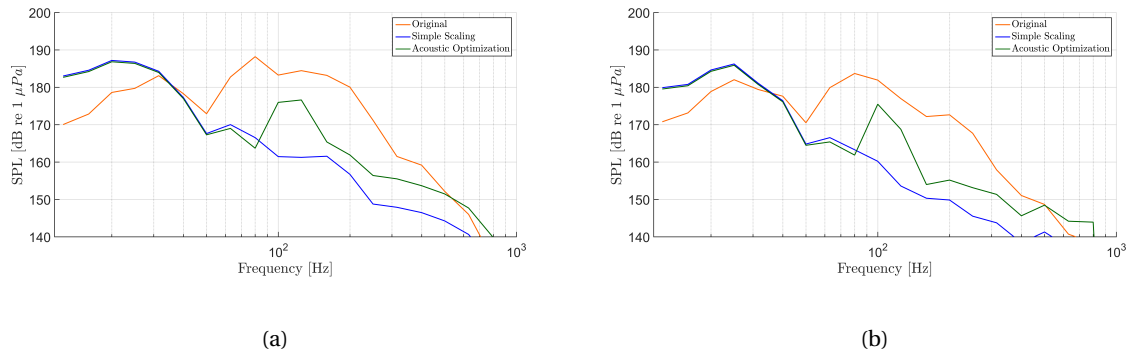


Figure 8.17: Frequency spectrum after excitation with the original, simple scaling and acoustic optimized impact diagram at (a) $h = 2$ m and (b) $h = 12$ m from the seabed and 100 m from the pile

8.6.2. Response during pile driving in time domain

Having analyzed the response in frequency domain, the focus is now placed on the time domain response. In previous subsection it was noticed that shifting the energy towards the lower frequencies, result into more energy accumulating around the low frequencies. Due to the cut-off frequency of 26 Hz, a significant part must propagate into the soil layer. In order to quantify this effect, the pressure wave propagation in time for both the fluid as for the soil layer is examined. Figure 8.18 shows the pressure wave evaluation from the original, simple scaling and acoustic optimized impact diagram at $h = 2$ m and $h = 12$ m from the seabed and 50 m from the pile.

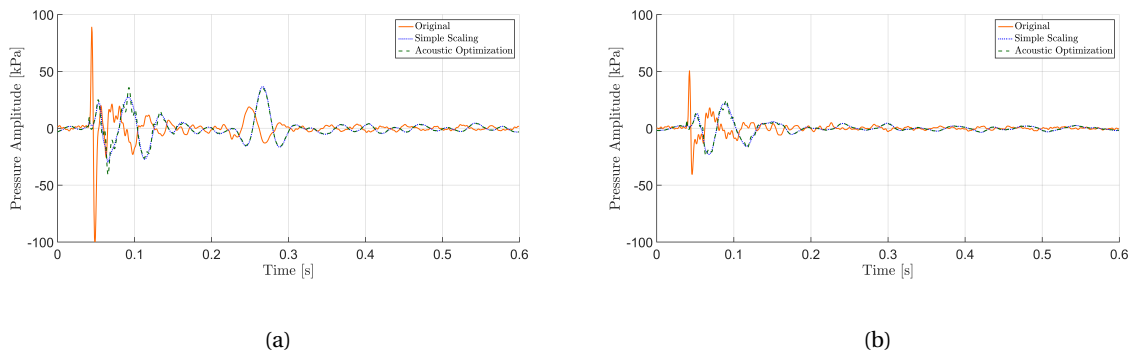


Figure 8.18: Pressure wave propagation after excitation with the original, simple scaling and acoustic optimized impact diagram at (a) $h = 2$ m and (b) $h = 12$ m from the seabed and 50 m from the pile

Enlargement of the time duration of the impact force reduces the peak level of the pressure wave significantly as can be noticed at the first pressure wave at both heights. The time duration of acoustic optimized impact diagram is enlarged with 290% compared to the original impact diagram. As a consequence the peak level drops with 60%. For the simple scaling impact diagram the enlargement is a bit larger with 300%, resulting in a peak level drop of 71%. This is more than with the acoustic optimization method. That the peak level drops with enlarging the impact force, does not necessarily mean that the final sound exposure level also decreases due to its dependency of time. On the other hand, the energy shift corresponds to an increase of soil interaction by compressional, shear and Scholte waves as can be seen at the second pressure wave around 0.25 sec. Enlargement of the time duration with 290% results in an increase of soil wave propagation amplitude of 94%, which is a significant large part. For the simple scaling impact diagram, with the enlargement of 300% compared to the original impact diagram, the increase in pressure waves reflecting from soil interaction is also 94%. Moving up in the fluid layer this effect almost completely disappears.

In order to determine whether the soil interaction is dominated by shear or compressional waves, both directions in the fluid layer are shown in Figure 8.19. Here it becomes clear that the same as only for the original impact diagram happens, the dominant motion in the first pressure wave is in the radial direction. This

means a compressional wave causing the primary noise path. The second pressure wave is a combination of radial and vertical velocities in the fluid layer, meaning that this pulse is influenced by Scholte waves at the soil water interface. Remarkable is the large increase in amplitude of the low frequency waves compared to the response of the original impact diagram. Hence the particle motion in the soil layer is examined to determine what is causing the second pressure wave in the fluid layer. Figure 8.20b shows the particle velocity of the soil layer in radial and vertical direction at 50 m from the pile and at the soil water interface. Here the same as with the original impact diagram occurs. A vertical polarization of the soil response can be noticed, meaning a domination of shear waves.

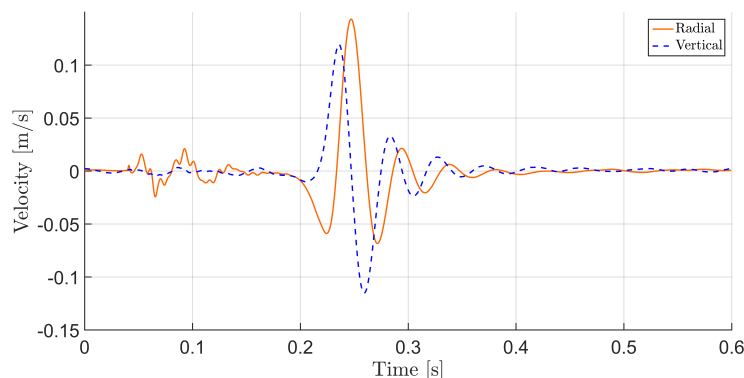


Figure 8.19: Vertical and radial velocity in fluid layer for the acoustic optimized impact diagram at 50 m from pile and 2 m above seabed

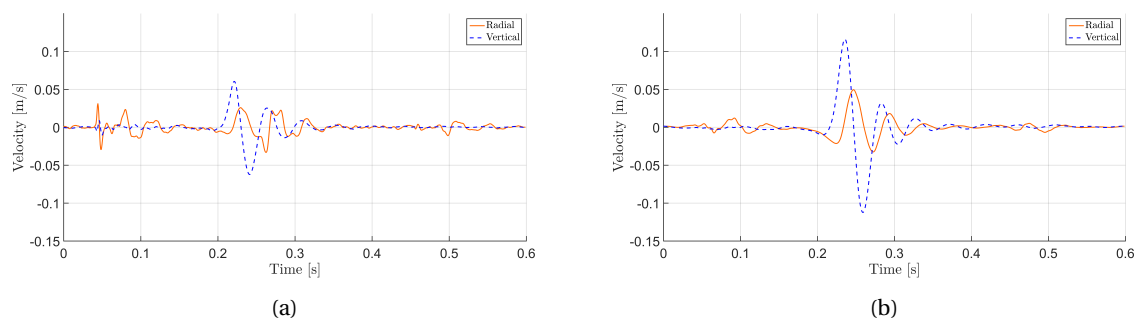


Figure 8.20: Vertical and radial particle velocity in soil layer for (a) Original impact diagram and (b) Acoustic optimized impact diagram at 50 m from pile and at soil water interface. The vertical and radial velocity of the simple scaling impact diagram are similar for the acoustic optimized impact diagram and subsequently not shown here.

Compared to the vertical and radial particle velocity caused by excitation of the original impact diagram, Figure 8.20a, the vertical and radial velocity has increased with 95%. On top of that, it can be noticed that the influence of the compressional wave in the soil for the acoustic optimized impact diagram has nearly completely disappeared. The same occurs in the fluid layer where the peak level drops by the enlargement of the impact force, but the time duration over which the particle velocity wave is distributed increases.

In order to further quantify the reduction of the compressional pressure wave and the enlargement of the shear wave interaction, the instantaneous acoustic power as introduced in section 5.4.2 is examined. This gains insight in the diversion between compressional, shear and Scholte waves in the fluid and soil layer. Figure 8.21a shows the instantaneous power for the fluid layer at four radial distances from the pile. Close to the pile surface the energy carried by the compressional and Scholte waves are indistinguishable. But when moving further from the pile surface, the difference increases and becomes visible. The first energy block is related to the compressional pressure wave due to the fast arrival in time. The second pressure wave indicates the energy carried by the shear and Scholte wave that arrives much later in time than the compressional wave. Both wave types are present due to the earlier defined combination of horizontal and vertical polarized pressure waves. From the figure it can be derived that the amount of energy carried by the shear and Scholte

wave increases over radial increasing distance. The increase in energy carried by the second energy block in the fluid layer between 10 and 40 m is 40%. Where with the original impact diagram a decrease was observed. This means that more energy radiates into the fluid layer from the soil in comparison to the original impact diagram.

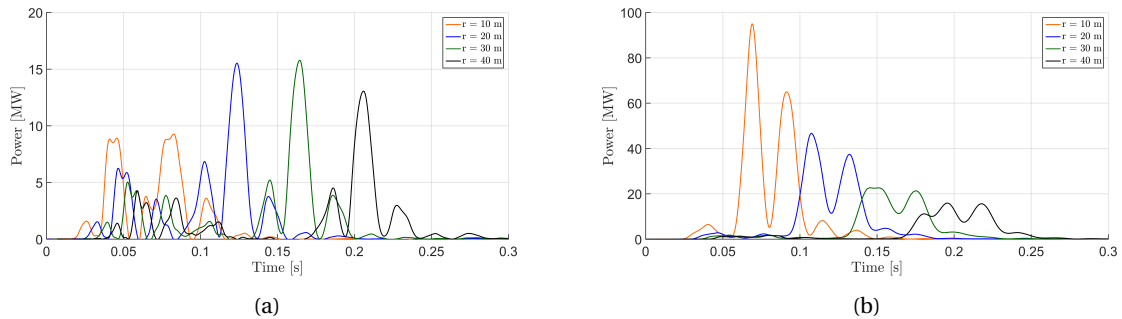


Figure 8.21: Instantaneous acoustic power in the (a) fluid layer and (b) soil layer at 10, 20, 30 and 40 m from the pile

In order to validate this statement, the instantaneous acoustic power in the soil layer is examined. Figure 8.21b shows the instantaneous acoustic power for four different distances from the pile in the soil. Between 10 and 40 m radial distance the energy reduction of the low frequency wave is 75%, compared to the 81% reduction with the original impact diagram. Less decay of energy means more energy stored in the soil. Consequently, it can be concluded that more energy is localized around the soil-water interface in the form of Scholte waves. As these waves are less attenuated, they remain their energy over radial distance. However, their influence at 750 m from the source is still questioned.

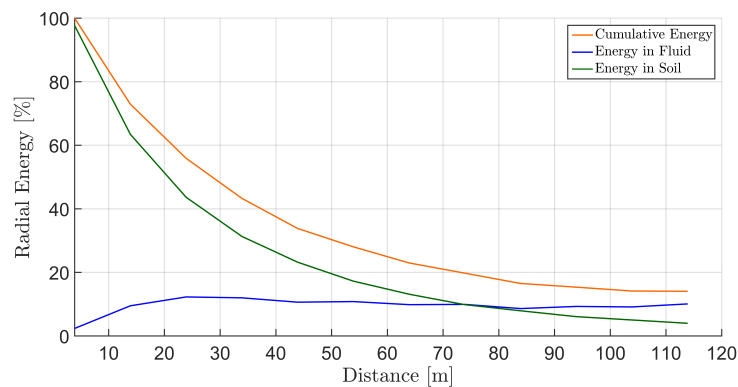


Figure 8.22: Radial energy distribution over fluid and soil layer

Figure 8.22 shows the energy radiation over radial distance into the different material layers. Approximately 9 - 12 % of the input energy radiates into the fluid. At 10 m distance from the pile, 40% of the radiated energy in the fluid is carried by the compressional wave. As a result from the upper boundary of the energy radiated into the fluid, less than 4.8% of the total input energy is attributed to compressional waves. On top of that, around 7.2% of the total input energy radiated into the fluid layer is carried by Scholte waves along the soil water interface. This is an increase of the secondary noise path compared with the original impact diagram with the same soil conditions.

The aim of this research is to investigate ways to reduce noise levels directly at the source of the noise, instead of mitigating the radiated noise. By optimizing the impact force in order to reduce underwater noise during installation of a large sized monopile, it is of importance to evaluate the final noise level. As discussed earlier, the model can not predict with the current soil conditions at 750 m due to the use of the DFT. Consequently, comparing with measured data at 750 m is pointless. The computed data is therefore only compared with

Table 8.3: Noise levels after excitation with the simple scaling and acoustic optimized impact diagrams

Impact Diagram	Category	Distance m	Model Original dB re $1\mu Pa^2 s$	Model Adjusted dB re $1\mu Pa^2 s$	$\Delta SEL_{05}/\Delta L_{peak}$ -
Simple Scaling	SEL_{05}	100	193.7	193	-0.7
	L_{peak}	100	217.4	206.6	-10.8
Acoustic Optimization	SEL_{05}	100	193.7	192.8	-0.9
	L_{peak}	100	217.4	207.7	-9.7

the original impact diagram at 100 m distance from the pile. Table 8.3 summarizes the results and compares these with the model predictions of the original impact diagram. From here it can be noticed that there is a difference between reduction of the SEL_{05} and the L_{peak} for the simple scaling and acoustic optimization method. The simple scaling has a higher reduction of peak level, but a lower reduction of the sound exposure level in comparison with the acoustic optimized impact diagram. In the case of extrapolating the results till 750 m, the reduction is expected to increase since the losses with distance in the soil are expected to be larger, forcing the noise levels downwards.

8.7. Conclusions

In this chapter, the force optimization in order to reduce underwater piling noise is developed and examined. This is done by optimizing the impact force with respect to noise, while keeping the drivability unimpaired. The absolute excitation spectrum of the hammer must be able to minimize the response of so called dominant acoustic frequencies. As a result, the vibration response spectrum is reduced and hence the underwater noise.

For the optimization process, multiple steps are taken. Firstly, the dominant acoustic frequencies of the pile-water-soil system are derived that result in a high response after excitation. Secondly, a method is developed to evade the dominant acoustic frequencies in the amplitude excitation spectrum of the hammer. One simple scaling method and one more acoustic optimized method. Both methods make it possible to evade frequencies in the transfer function of the fluid. By scaling the absolute excitation spectrum of a real impact hammer, the main energy content of the spectrum shifts towards the lower frequencies. As a result, more energy is applied to frequencies below the cut-off frequency. Subsequently the time traces of the absolute excitation spectrum's were obtained by means of Fourier transformation.

Thirdly, the drivability of the new obtained impact diagrams are investigated. Driving the pile into the soil is the priority of the impact diagram. By means of the self constructed drivability model, the pile tip displacement that has to overcome the quake value is analyzed for both impact diagrams. It has been shown that both impact diagrams are able to overcome the quake value and drive the pile into the soil in a reasonable amount of blows. In the final stage of penetration, the original impact diagram needs an average of 98 Blows/25 cm, where the simple scaling and acoustic optimization impact diagrams only need 21 and 25 blows/25 cm respectively.

Finally, the noise predictions were analyzed with the Spring Dashpot model and the Elastic Medium model. The analysis is performed in both frequency and time domain. First the results are compared with the results from the original impact diagram in the Spring Dashpot model. The differences in response in the fluid layer are clearly indicated. The propagation of the pressure waves in the radial direction is discussed. It is shown that due to the enlargement of the time duration of the impact diagram, the peak level of the pressure wave drastically decreases. Thereafter the gradient compared to the final noise level dependency is discussed. Secondly, with the Elastic Medium model the interaction with the soil is better investigated. Again by comparing the results with the original impact diagram, a clear view of the influence of shifting the energy in the amplitude excitation spectrum towards specific frequencies is given.

The results show an increased amount of energy at low frequencies carried by waves traveling along the soil-water interface. Due to the high geometrical and material damping in the soil, the high frequency compressional waves attenuate rather quickly with increasing distance from the pile, resulting in shear and Scholte waves being dominant at larger distances. Less than 4.8% of the total input energy is attributed to compres-

sional waves in the fluid layer. Furthermore, around 7.2% of the total input energy radiated into the fluid layer is carried by Scholte waves along the soil-water interface. The energy carried by the latter is increased compared to the previous analysis with the non-adjusted impact diagram. However, the Scholte wave produces only pressure fluctuations in the water close to the soil-water interface and not further up into the water column. With the current derived analysis method, the noise levels at 100 m from the piling source are reduced. A reduction is achieved of $\Delta L_{peak} = -9.7$ dB and $\Delta SEL_{05} = -0.9$ dB, while drivability is kept largely unimpaired. By enabling the Elastic Medium model to work independently on the amount of frequency steps, the reduction in the far field is expected to increase even further.

Conclusions and Recommendations

9.1. Conclusions

The aim of this research is to investigate ways to reduce noise levels caused by the pile driving activity of a large sized monopile. First of all, insight in the noise propagation till 750 m during the installation is obtained. This is done by modeling acoustics with a basic Spring Dashpot model and a more advanced Elastic Medium model, discussed in the chapters 4 and 5. Secondly, an optimization of the impact force with respect to noise is conducted. This is done by adjusting the absolute excitation spectrum of the hammer in chapter 8. In order to keep drivability of the adjusted impact force unimpaired, a basic non-linear drivability model is developed in chapter 6. In the present chapter, the final conclusions and recommendations are presented.

The main conclusions drawn from this research are:

- Four different models are used during this research. Two models for acoustic predictions, namely the Spring Dashpot model and the Elastic Medium model. Two models for drivability predictions, namely the GRLWEAP drivability program and the TU Delft drivability program. The vertical velocity propagation is the base of the final propagating pressure waves in both acoustic models. For the drivability models, the velocity in the shell determines the displacement of the pile with regard to the soil. By comparing the velocity in the shell for all four models, the similarity of the working principle of the models is justified. The results show a different vertical velocity propagation for the two acoustic models compared to the two drivability models.

Due to the long time duration of the impact force, a large amount of low frequency waves are excited. The acoustic models are solved in the frequency domain and account for frequency dissipation. At low frequency, the wavelength is long and the front of these waves has already been close to the soil layer just after impact. As a result the pile starts deforming together with the soil in the Spring Dashpot model. Furthermore, the soil material damping and spring stiffness are assumed constant throughout the frequency range. Consequently, the stiffness of the complete system and hence the vertical velocity from the initial moment in time is influenced. In the Elastic Medium model the soil is better represented by a three-dimensional description of the soil. The description of the soil is not influenced by the excited frequencies. Therefore, the vertical velocity in the pile is not influenced through the complete system from the initial moment in time. Consequently, the vertical velocity propagation in the Elastic Medium model and both drivability models are similar. Only the Spring Dashpot model has a strong deviation which is therefore further investigated.

To reduce the effect of the increased stiffness of the complete system in the Spring Dashpot model, the effect of the soil elasticity on the vertical velocity is examined. The results show a large influence of the soil elasticity and hence increase the uncertainty of selecting the correct parameters. By reducing the soil elasticity, the vertical velocity propagation in the pile is adjusted to an equal propagation path as the other three models. Consequently, a fair comparison between all four models is guaranteed. Furthermore, a similarity between the vertical spring stiffness of the Spring Dashpot and drivability model is obtained when adjusting the soil elasticity. This enables the prediction of soil conditions in the Spring Dashpot model with more certainty.

- The Spring Dashpot model calculates the modes of vibration in the monopile after excitation with a force. The frequencies of these vibrations are finally associated with the modal propagation. The complete acoustic field is then constructed by summing up contributions of each of the modes.

The response of the Spring Dashpot model is compared with measurements. The obtained results are within an acceptable accuracy of ± 2 dB. Due to the large sized monopile, the ring frequency of the shell shifts towards lower frequencies. In addition, the amount of energy required to drive the monopile into the soil increases, resulting in a longer duration of the impact force and hence lower frequencies to be excited. The analysis performed shows a large amount of energy carried by these low frequency waves. However, no modal propagation through the soil layer is taken into account in the present model. Consequently, their influence through the soil is not significant at 750 m from the pile with the present soil conditions.

- The Elastic Medium model has a three-dimensional description of the soil. This reduces the uncertainty of the selecting the correct soil stiffness and damping factors as in the Spring Dashpot model. Furthermore, the model enables to account for shear waves propagating through the soil and Scholte waves propagating along the soil-water interface.

The analysis shows for the present soil condition a large influence of the soil. From the total inserted energy at the top of the pile, approximately 86-90% radiates into the soil layer in the form of compressional, shear and Scholte waves. The remaining energy radiates directly into the fluid layer. From the latter, around 12% is attributed to the compressional waves propagating directly into the fluid layer, the so called primary noise path. A smaller part of approximated 2% of the total input energy radiates as the secondary noise path in the form of Scholte waves along the soil-water interface. The attenuation of the Scholte wave is less in comparison with other propagating modes due to the relative slow wave speed. However, the Scholte wave produces only pressure fluctuations in the fluid close to the soil-water interface and not further up into the fluid layer. Their influence shows to be limited at longer distances, but the amount of energy lost in them is essential in order to be able to get a fair impression of the energy transferred into acoustic waves in the fluid layer.

- For the Elastic Medium model, a sensitivity analysis of the soil parameters is performed. The influence of the following three parameters on the final response is examined, i) soil elasticity, ii) attenuation factors for the propagating waves in the soil layer and iii) multiple soil layers.

The analysis shows a large diversity of the response to different soil elasticity's and corresponding wave velocities. For relative less stiff soil, the pressure and corresponding noise level in the fluid layer decrease. The influence is large at frequencies below 200 Hz and close to the soil-water interface. As a result, estimating a correct soil elasticity is crucial. Furthermore, the soil attenuation factors show to have negligible influence on the final noise levels in the fluid layer. The factor must be in the right magnitude of the analyzed soil material, but no high accuracy is required. Finally, the influence of two soil layers is analyzed. The analysis shows a minor influence on the noise levels in the fluid layer. Consequently, the influence is not significant when including multiple soil layers in order to predict the noise levels in the fluid layer correctly.

- The application of the Discrete Fourier Transform (DFT) in both acoustic models restricts to a pre-defined frequency range and correlating time duration. Due to the low frequency waves traveling through the soil with a low wave speed, the maximum distance of the propagating waves is limited. The Spring Dashpot model does not account for the waves propagating through the soil. This enables the model to analyze up to a further radial distance than the Elastic Medium model with the current analyzed soil conditions. The results of both models were compared at 100 m distance of the pile. This shows a similar response above 100 Hz. Below 100 Hz, the interaction with the low frequency waves traveling through the soil is indicated. A large amount of energy carried by the low frequency waves is taken into account in the Elastic Medium model and not in the Spring Dashpot model.
- In order to keep the drivability with the optimized impact force unimpaired, a basic non-linear drivability model is developed based on mass, springs and dashpots. The drivability predictions match with the predictions of GRLWEAP. The non-linearity is limited to the description of the sliding of the monopile into the soil with locally reacting non-linear vertical springs. No radial springs are taken into account that account for the increased shaft area of a large sized monopile.

- The aim of this research is to investigate ways to reduce noise levels directly at the source of the noise, instead of mitigating the radiated noise. This is achieved by minimizing the response of dominant acoustic frequencies in the fluid layer. The results show an increased amount of energy at low frequencies carried by waves traveling along the soil-water interface. Due to the high geometrical and material damping in the soil, the high frequency compressional waves attenuate rather quickly with increasing distance from the pile, resulting in shear and Scholte waves being dominant at larger distances. Less than 4.8% of the total input energy is attributed to compressional waves in the fluid layer. Furthermore, around 7.2% of the total input energy radiated into the fluid layer is carried by Scholte waves along the soil water interface. The energy carried by the latter is increased compared to the previous analysis with the non-adjusted impact diagram. However, the Scholte wave produces only pressure fluctuations in the water close to the soil-water interface and not further up into the water column. With the current derived analysis method, the noise levels at 100 m from the piling source are reduced. A reduction is achieved of $\Delta L_{peak} = -9.7$ dB and $\Delta SEL_{05} = -0.9$ dB, while drivability is kept largely unimpaired.

9.2. Recommendations

Underwater noise is a complex subject and much is still unknown. To increase knowledge there is need for more extensive studies. On top of that, both acoustic models are still in development stage and hence need further improvement. Consequently, the following three main topics are interesting for further research. Each with their own specific sub topics.

Acoustic models

- Remove the application of the Discrete Fourier Transformation, and apply Fourier Transformation. This enables the analysis of infinite time duration. Consequently, this makes it possible to better investigate the influence of the low frequency waves and especially the Scholte waves at the soil-water interface in the far field. Finally a verification of the limited influence of the secondary noise path at 750 m from the monopile can be performed.
- Include the application to mitigate noise by current existing noise mitigation methods. As the industry is seeking for methods to reduce the noise, it would be interesting to be able to model the noise mitigation during installation of large sized monopiles. And hence support the selection of correct noise mitigation method.
- Account for sliding during piling. Especially for the Spring Dashpot model due to the similarities with present drivability models. Part of the inserted energy dissipates into the fluid and soil in the current model. In reality, this energy is partly used to be able to drive the pile into the soil. Combining these two principles could result in a much more useful model.
- Validate with measured data at multiple, near field and far field, locations. Pressure levels in the fluid layer together with radial and vertical velocities along soil-water interface must be validated. This enables a reduction of the uncertainty of the fluid and soil attenuation factors and soil elasticity parameters.

Drivability models

- Evaluate the drivability models of TU Delft and GRLWEAP for large sized monopiles. Both models still need to be verified in the case of large piles and relatively low frequencies. With the increased size of the monopiles the shaft resistance becomes more dominant in comparison to small diameter monopiles. A correct representation of the shaft resistance must be obtained by including radial springs in the model. Furthermore, with the enlargement of the applied impact force the dynamics involving drivability change. The downward propagating waves are influenced by the upward reflecting propagating waves. In the current models this is not taken into account and therefore advised as further research.

Ways of reducing underwater noise

- The aim of this research is to investigate ways to reduce noise levels directly at the source of the noise, instead of mitigating the radiated noise. In the current method, scaling of the original amplitude exci-

tation spectrum is applied to shift the excited frequency bandwidth. Further research should be conducted in developing the method of avoiding the dominant acoustic frequencies. The effect of minimizing the response of different dominant acoustic frequencies should be taken into account. Furthermore, the effect of the minimization of more dominant acoustic frequencies to the response in the fluid layer should be examined.

- Examine the effect of current noise mitigation methods on the noise generated by an impact on a large sized monopile. Current noise mitigation methods show to be most effective above 100 Hz. As the frequency spectrum after impact of a large size monopile still results in pressure levels above 100 Hz, the current noise mitigation methods can still reduce the final noise levels.

Boskalis

- Modelling underwater noise is valuable to obtain expected noise levels. Anticipating on these noise predictions can save downtime and finally reduce costs. Due to its description of the soil, the Elastic Medium model is a valuable model to obtain the desired results. By combining this with the drivability model GRLWEAP, the impact diagram can be obtained. This serves as input for the acoustic model. Furthermore, both models are parametric models which require only relative simple input parameters. The Elastic Medium model has a function to describe the soil layer by an equivalent fluid. In the current research the noise propagating through the secondary noise path is shown to be limited. By modelling the soil as a fluid the maximum radial distance is increased. Consequently, noise predictions at 750 m can be performed with the current version of the Elastic Medium model.

Bibliography

- J.D. Achenbach. Wave Propagation in Elastic Solids. *North-Holland Series in Applied Mathematics and Mechanics*, 1973.
- Agilent Technologies. The Fundamentals of Signal Analysis. Technical report, 2000.
- Michael a. Ainslie. *Principles Of Sonar Performance Modeling*. 2010.
- T Alm and L Hamre. Soil model for pile driveability predictions based on CPT interpretations. *Proceedings of the 15th international Conf. on Soil Mechanics and Foundation Engineering, Istanbul*, 2:1297 – 1302, 2001.
- H Bailey, B Senior, D Simmons, J Rusin, G Picken, and P.M. Thompson. Assessing underwater noise levels during pile-driving at an offshore windfarm and its potential effects on marine mammals. *Marine Pollution Bulletin*, 60(6):888–897, 2010.
- Bloomberg. Global trends in clean energy investment. Technical report, 2016.
- Brigham. Noise and the Fourier Transform. 2005.
- Benedikt Bruns, B. Bruns, P. Stein, Philipp Stein, C. Kuhn, Christian Kuhn, Hauke Sychla, H. Sychla, Jörg Gattermann, and J. Gattermann. Hydro sound measurements during the installation of large diameter offshore piles using combinations of independent noise mitigation systems. *Inter-Noise Conference, Melbourne, Australia, 16-19 November 2014*, page 10 pp., 2014.
- M.J. Buckingham. Compressional and shear wave properties of marine sediments: comparisons between theory and data. *The Journal of the Acoustical Society of America*, 117(January):137–152, 2005.
- EIA. International Energy Outlook 2016. Technical report, 2016.
- EWEA. The European Offshore Wind Industry: Key Trends and Statistics 1st Half 2015. *European Wind Energy Association*, 2016.
- M.J. Fajfer. Underwater noise caused by pile driving: Impacts on marine mammals, regulations and offshore wind developments. Technical report, 2014.
- Fistuca. GRLWEAP Model description BLUE Piling. Technical report, 2016.
- Moritz B Fricke and Raimund Rolfes. Towards a complete physically based forecast model for underwater noise related to impact pile driving. *Journal of the Acoustical Society of America*, 137(3):1564–1575, 2015.
- G.G Goble and F Rausche. Wave equation analysis of pile foundations. Technical report, 1986.
- GWEC. Global wind report: Opening up new markets for business. Technical report, 2015.
- Royal Haskoning. Underwater Noise. Social Cost benefit Analysis. Technical Report June, 2015.
- Y.A. Hegazy and P.W. Mayne. Statistical Correlations Between Vs and Cone Penetration Data For Different Soil Types. *Proceedings of the International Symposium on Cone Penetration Testing*, 2(July):173–178, 1995.
- M. H. Hussein, W.A. Woerner, M. Sharp, and C. Hwang. Pile Driveability and Bearing Capacity in High-Rebound Soils. *GeoCongress 2006*, pages 1–4, 2006.
- F.B. Jensen, W.A. Kuperman, M.B. Porter, and H. Schmidt. Computational Ocean Acoustics. Technical report, 2011.
- C. Kuhn, H. Sychla, P. Stein, B. Bruns, J. Gattermann, and J. Degenhardt. Dynamic measurements of pile deflections as a source of underwater sound emissions during impact driving of offshore pile foundations. *Inter-Noise 2014, Melbourne, Australia*, page 10, 2014.

- D. Loukidis, R. Salgado, and G. Abou-Jaoude. Assessment of axially-loaded pile dynamic design methods and review of indot axially-loaded pile design procedure. Technical report, 2008.
- W. Lowrie. *Fundamentals of Geophysics*. 2007.
- A.V. Metrikine and A.C.W.M. Vrouwenvelder. *Dynamics of Structures – CT4140. Part 2 Wave Dynamics*.
- P Middelndorp and G. E. H. Verbeek. Thirty Years of Experience with the Wave Equation Solution Based on the Method of Characteristics. *Geo-Congress*, pages 1–12, 2004.
- S.L. Peterie, R. D. Miller, and J. Ivanov. Seismology and Its Applications in Kansas. Technical report, 2014.
- P.G. Reinhall and P.H. Dahl. An Investigation of Underwater Sound Propagation from Pile Driving. *Washington State Department of Transportation*, 2011.
- S. P. Robinson, P. A. Lepper, and R. A. Hazelwood. Good Practice Guide for Underwater Noise Measurement. *National Measurement Office, Marine Scotland, The Crown Estate*, (NPL Good Practice Guide No. 133), 2014.
- Z. Saleem. Alternatives and modifications of Monopile foundation or its installation technique for noise mitigation. Technical report, 2011.
- E.A.L Smith. Pile driving analysis by the wave equation. *American Society of Civil Engineer*, 127:1145 –1193, 1960.
- P. Sparrevik. Monitoring Offshore Wind Turbine Foundations. *Oceanology International*, 2014.
- A. Tsouvalas and A. V. Metrikine. A semi-analytical model for the prediction of underwater noise from offshore pile driving. *Journal of Sound and Vibration*, 332(13):3232–3257, 2013.
- A. Tsouvalas and A. V. Metrikine. Wave radiation from vibratory and impact pile driving in a layered acousto-elastic medium. *Proceedings of the 9th International Conference on Structural Dynamics, EURO-DYN 2014*, (July):3137–3144, 2014.
- A. Tsouvalas and A.V. Metrikine. Offshore noise generated by pile driving. Technical report, 2015.
- UBA. Empfehlung von Lärmschutzwerten bei der Errichtung von Offshore-Windenergieanlagen (OWEA). Technical report, 2011.
- G.E.J.S.L Voitus van Hamme, J.W. Jansz, H Bomer, and D Arentsen. Hydroblok and improved piledriving analysis. *De Ingenieur*, 18(86):345 –353, 1974.